The Thesis Committee for Palash Dhaval Gajjar
Certifies that this is the approved version of the following Thesis:

Characterization of Li-ion Battery Transition from Normal Operation to Abuse Conditions

Approved by
Supervising committee:

Ofodike Ezekoye, Supervisor

Venkat Subramanian

Characterization of Li-ion Battery Transition from Normal Operation to Abuse Conditions

by

Palash Dhaval **Gajjar**

Thesis

Presented to the Faculty of the Graduate School of

The University of Texas at Austin

in Partial Fulfillment

of the Requirements

for the Degree of

Masters of Science in Engineering

The University of Texas at Austin

May 2020

Acknowledgments

A big thank you to my advisor Dr. Ofodike Ezekoye for welcoming me into the UT Fire Research Group. His encouragement and research guidance throughout my Masters study at the University of Texas at Austin has allowed me to augment my knowledge in both, technical skills and effective communication. His support, in research and other areas, has played a crucial role in my personal development.

Next, I would like to thank my lab-mate, Haotian Yan, for helping me with the experiments. His experimental skills proved to be very helpful in the development and validation of my computational work. Other members of the lab, too, were highly supportive. Thanks to Serhat for helping me with understanding thermal runaway in batteries, Robert for helping with experiment debugging, and Tyler for suggesting different regression models.

Also, I want to thank Dr. Venkat Subramanian for providing insightful inputs and explaining battery models using first principles. The discussions I've had with him have always been very helpful and enlightening.

Lastly, I would like to express my gratitude to the Department of Justice for sponsoring the project. This funding has allowed us access to resources that proved to be instrumental to the construction of experiments and models. Grant number: 2018-MU-BX-0004.

Abstract

Characterization of Li-ion Battery Transition from Normal Operation to Abuse Conditions

Palash **Dhaval** Gajjar, M.S.E.

The University of Texas at Austin, 2020

Supervisor: Ofodike Ezekoye

This thesis aims at the identification and modeling of the underlying phenomena that trigger thermal runaway in lithium-ion batteries. While a great amount of research has been done on simulation of lithium-ion battery's normal operation and thermal runaway separately, very few have attempted to link both the conditions. This study can be regarded as a stepping stone to the development of robust battery management systems that can predict whether the lithium-ion battery will go into thermal runaway or not. In the first two chapters, a brief introduction and analyses of different modeling techniques are presented. The next chapter pushes the physics-based P2D model to thermal abuse conditions and specifies a few modifications that can improve the scope of its validity. Since the study in this area is limited, a simple first-order model using an equivalent circuit is chosen to simulate battery operation at relatively high temperatures. The fourth chapter deals with the parameterization and the validation of the circuit model. At the end, the model output is compared to experimental data. The results show that the thermal response of the battery can be captured by this simple model, however, some steps need to be taken for accurate parameterization. Some model modifications are added to increase the fidelity of the current model. A case with thermal runaway is also presented where the different regions of battery degradation are specified. The insights provided can be utilized to further tune the circuit model.

Table of Contents

List of Tables

List of Figures

1 Background

This chapter presents an extensive overview of lithium-ion battery applications, construction, physics, and abuse mechanisms. Furthermore, it covers the research objective and the motivation behind this thesis.

1.1 Introduction

Given the rate of depletion of fossil fuels, the need for transition from traditional fuel-based energy generation methods to alternative renewable methods is evident. Many efforts have been made to make this shift through the conversion of energy present in sunlight and wind to usable forms. However, the energy obtained from such sources is intermittent and requires efficient energy storage systems for transportation and supply to different areas. Among various energy storage arrangements, lithium-ion battery (LIB) is one of the most researched types of batteries. It has high energy density, high efficiency, high cyclability, and long life, hence, warranting extensive development and use [1, 2].

The thermal behavior of LIBs is an impedance to its long term application as they generally function well only between 0°C and 40°C [3, 4, 5]. Below 0°C, lithium plating occurs at the anode, which leads to loss of capacity of the LIB, whereas, above 40°C, other degradation processes like solid-electrolyte interface (SEI) breakdown cause capacity fade [6, 7]. Thus, chances of a LIB going into thermal runaway increase, which is a major concern from a safety point of view. The usefulness of modeling the LIB function can thus be seen.

Many modeling methodologies have been derived for simulation of LIBs, ranging from high fidelity multi-physics models to purely empirical models [8]. The restricted use of stiff physics models for a real-time application can be attributed

to its complexity and computational cost, whereas, empirical models suffer from the lack of robustness as they are designed to model a single type of cell and are unable to handle conditions outside their definition domain. There are equivalent circuit models (ECM) that sit at the sweet spot in the modeling spectrum. They are constructed using experimental fits and can cover a wide range of operations. The circuit parameters also represent certain aspects of battery electrochemistry, hence, establishing the reason for their use in the circuit.

This thesis concentrates on the thermal aspect of the LIB operation. A physics-based model is first used to model certain operating conditions, however, given the number of parameters required, the model of choice for further analysis is changed to ECM. Since circuit models are simple to implement and understand for any type of LIB, their analysis from an application point of view is justified. Despite its advantages, its application comes at the cost of accuracy. Therefore, the scope of its applicability is clearly defined in section 4.2.1. This also provides the model with more freedom in accuracy.

1.2 Li-ion Battery Design

Batteries, in general, are made up of 5 essential layers: negative current collector, negative electrode, separator, positive electrode, and positive current collector. Design of LIBs [9] is discussed in the following paragraphs.

The most popular choice for the negative electrode in LIBs is graphite. It is thermally and electrically conductive, resistant to heat, and, most importantly, it has high reversible intercalation capability [10]. The positive electrode is generally composed of Lithium oxides like Lithium Cobalt Oxide ($LiCoO_2$), Lithium Ferrous phosphate ($LiFePO_4$), Lithium Manganese Oxide ($LiMn_2O_4$), and their combinations. The electrodes are made to be porous to maximize their contact with the electrolyte, thus promoting spatial uniformity and efficiency of current exchange within the electrodes.

A separator has a two-fold purpose in batteries. In LIBs, it provides easy passage

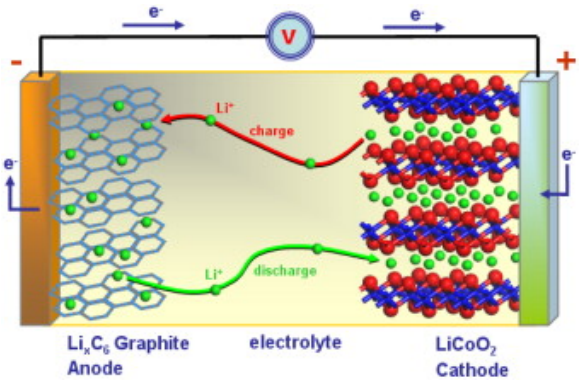

Figure 1.1: Discharge of LCO cell [12]

for lithium ions between the electrodes, and, at the same time, acts as a barrier for electrons, forcing them to flow through the external circuit. The most typical choices for separator material include polyethylene (PE), polypropylene (PP), and their combinations (PE/PP). All the solid components of the LIB are immersed in a conducting aqueous base, which is a mixture of organic solvents, lithium salts, and additives. One of the most used salts in LIBs today is Lithium Hexafluorophosphate ($LiPF_6$) [11]. Finally, the current collectors provide a way for electrons to flow into or out of the electrodes. For most LIBs, the copper plate is placed at the negative end, while the aluminum plate is used at the positive end of the battery.

During discharge, oxidation of lithium metal occurs at the negative electrode (anode for discharge), and reduction of lithium ions occurs at the positive electrode (cathode for discharge). The lithium ions produced at the anode surface diffuse (and migrate) through the electrolyte to the cathode surface, while the electrons generated at the anode surface move to the external circuit through the copper current collector. At the cathode, lithium ions recombine with the electrons coming from the external circuit and get settled into the lithium oxide host matrix. The direction of motion of lithium ions and electrons gets reversed during the charging process.

Most LIBs can be classified into 3 categories based on their shape: cylindrical, pouch, and prismatic [13]. Cylindrical cells are most commonly used due to their high energy density and ease of manufacturing. However, they have a disadvantage of low packing density, which is easily overcome by the pouch and prismatic cells. Pouch cells present a light-weight and space-efficient battery design solution, but

Figure 1.2: Different types of LIBs [14]

they are prone to swelling. Prismatic cells with their sturdy outer casing exhibit higher mechanical stability and are generally used in automotive applications.

1.3 Li-ion Battery Physics

This section covers various physics models that attempt to explain the different aspects of LIB functioning. Current state-of-the-art multi-physics simulation software employ modeling techniques that stem from the physics explained below. Emphasis is placed on electrochemical and thermal processes in LIB.

1.3.1 Electrochemical Behaviour

Stellar work was done by Doyle, Fuller and Newman [16, 17] in establishing the fundamental LIB electrochemistry at a macro-scale. In essence, their work involved the application of conservation equations of mass and charge on different regions of the battery.

Figure 1.3: Swollen pouch cell [15]

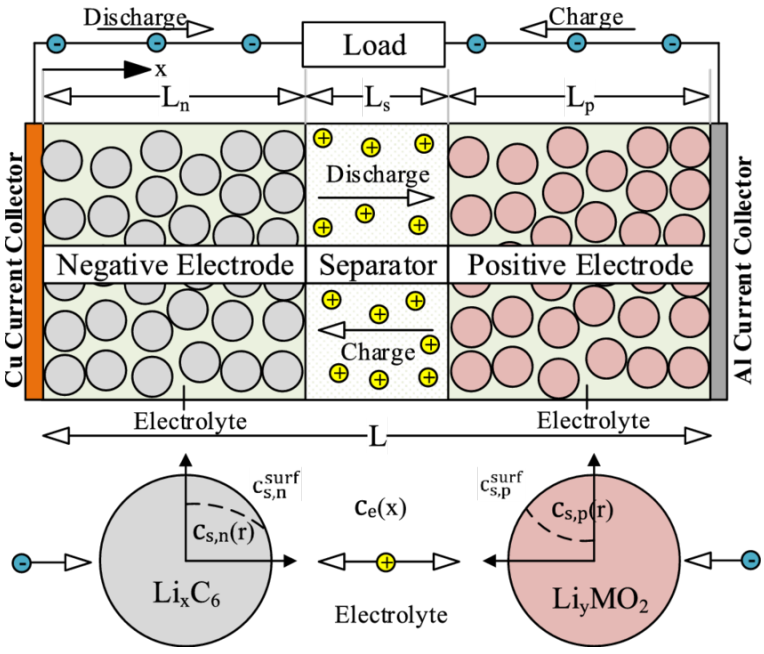

Figure 1.4: Typical P2D model [18]

1.3.1.1 Mass Conservation in Solid Phase, c_s

As discussed before, the redox reactions occur at the electrode-electrolyte interface. At the cathode surface, solid lithium gets consumed, and, to maintain a concentration balance, lithium moves from the core to the surface. This is a simple diffusion phenomenon with a reaction flux boundary condition. However, from a modeling

perspective, it is unreasonable to model an accurate porous structure of an electrode for diffusion. Doyle et al [16] addressed this problem by treating an electrode as a collection of solid lithium spheres, as shown in the figure 1.4. Diffusional mass transfer in each spherical domain is governed by the Fick's law of diffusion,

$$\frac{\partial c_s}{\partial t} = \frac{1}{r^2}\frac{\partial}{\partial r}\left(D_s r^2 \frac{\partial c_s}{\partial r}\right) \tag{1.1}$$

Using the spherical symmetry argument, the boundary condition at the center of the sphere is given by,

$$\left.\frac{\partial c_s}{\partial r}\right|_{r=0} = 0 \tag{1.2}$$

Since the solid concentration at the electrode surface is governed by the rate of lithium reaction, the charge transfer boundary condition for the sphere is given by,

$$\left.-D_s\frac{\partial c_s}{\partial r}\right|_{r=R_s} = j_{Li} \tag{1.3}$$

where c_s is the solid concentration, D_s is the solid diffusivity of the electrode material, R_s is the radius of the model sphere and j_{Li} is the rate of reaction. The significance of j_{Li} will be expounded upon later.

1.3.1.2 Mass Conservation in Liquid Phase, c_e

The application of a control volume-based method on liquid phase mass conservation was a bit tricky due to the interstitial nature of the electrolyte-electrode contact. The challenge of coming up with a macro-scale description of the interaction of the electrode pores (which are of the order of a micron) and the electrolyte, was solved by Newman's [19] porous electrode theory. In this theory, both the electrode and the electrolyte are treated as overlapping continuous media, and the porous nature of the electrode is incorporated into the conservation equations through a single material parameter known as porosity (ε).

The conservation law states that, for a given domain, the change in concentration of

a species over time is equal to the sum of the net concentration inflow and the rate of species generation. In the context of LIBs, the species generation term is related to the charge transfer process taking place at the electrode-electrolyte interface. The conservation equation for liquid phase concentration is given by,

$$\varepsilon \frac{\partial c_e}{\partial t} = \frac{\partial}{\partial x}\left(\varepsilon D_e^{eff} \frac{\partial c_e}{\partial x}\right) + a_s(1 - t_+) j_{Li} - \frac{\mathbf{i_e}}{F}\frac{\partial t_+}{\partial x} \tag{1.4}$$

On the right side of the equation 1.4, the first term represents the diffusion process, the second term acts as a concentration source term in the electrode regions (zero in separator region), and the third term takes into account the spatial variation of cation mobility in the electrolyte, which is generally assumed to be constant.

As lithium ions are not entering or leaving the battery domain at any time, the boundary conditions for liquid phase concentration can be conveniently written as (for 1D case),

$$\left.\frac{\partial c_e}{\partial x}\right|_{x=0} = 0 \quad \text{and} \quad \left.\frac{\partial c_e}{\partial x}\right|_{x=L} = 0 \tag{1.5}$$

where c_e is the lithium ion concentration in liquid phase, D_e^{eff} is the effective diffusivity in electrolyte, a_s is the active surface area per unit volume of the electrode, t_+ is the cation transference number, and $\mathbf{i_e}$ is the total current density in the electrolyte which is related to j_{Li} through Faraday's law ($\frac{\partial \mathbf{i_e}}{\partial x} = a_s F j_{Li}$).

1.3.1.3 Charge Conservation in Solid Phase, ϕ_s

The charge transfer process in solid phase is governed by a combination of the generalized Ohm's law and Faraday's law. Mathematically, we have,

$$\frac{\partial}{\partial x}\left(\sigma^{eff}\frac{\partial \phi_s}{\partial x}\right) = a_s F j_{Li} \tag{1.6}$$

For the case of constant current case, inflow current boundary condition is applied at current collector ends of each electrode. For the case 1D case illustrated in figure 1.4.

For negative electrode,

$$-\sigma_n^{eff}\frac{\partial\phi_s}{\partial x}\bigg|_{x=0} = I_{app} \quad \text{and} \quad -\sigma_n^{eff}\frac{\partial\phi_s}{\partial x}\bigg|_{x=L_n} = 0 \tag{1.7}$$

For positive electrode,

$$-\sigma_p^{eff}\frac{\partial\phi_s}{\partial x}\bigg|_{x=L_n+L_s} = 0 \quad \text{and} \quad -\sigma_p^{eff}\frac{\partial\phi_s}{\partial x}\bigg|_{x=L} = I_{app} \tag{1.8}$$

where ϕ_s is the solid phase potential, σ^{eff} is the effective electrical conductivity of the electrode, and I_{app} is the applied current per unit surface area of the battery.

1.3.1.4 Charge Conservation in Liquid Phase, ϕ_s

The movement of charges in the electrolyte region is primarily governed by two phenomena: diffusion and migration. The mathematical representation of this process involves a transformation of the generalized Ohm's law and the Nernst-Planck equation. The differential equation is given by,

$$\frac{\partial}{\partial x}\left(\kappa^{eff}\frac{\partial\phi_e}{\partial x}\right) - \frac{2R}{F}\frac{\partial}{\partial x}\left(T(1-t_+)\kappa^{eff}\frac{\partial ln(c_e)}{\partial x}\right) = -a_s F j_{Li} \tag{1.9}$$

where ϕ_e is the electrolyte potential, κ^{eff} is the effective electrolyte conductivity, and T is the temperature. The first term on the left hand side represents charge motion due to potential field (migration) and the second term takes care of the diffusion of charges due to a concentration gradient.

There has been some discrepancy in the literature regrading the boundary conditions of electrolyte charge transfer. Majority of researchers [20, 21] have suggested the following boundary conditions for the typical 1D case,

$$\frac{\partial\phi_e}{\partial x}\bigg|_{x=0} = 0 \quad \text{and} \quad \phi_e|_{x=L} = 0 \tag{1.10}$$

The negative electrode boundary condition can be interpreted as a zero electrolyte

charge flux and the positive electrode boundary condition can be seen as a setup of a reference zero potential for the battery. This gives a clear picture of how the potential field is varying with respect to a reference point. The reference zero potential can be set as the boundary condition for either ϕ_e or ϕ_s.

Other boundary condition [22] used for this process is,

$$\left.\frac{\partial \phi_e}{\partial x}\right|_{x=0} = 0 \quad \text{and} \quad \left.\frac{\partial \phi_e}{\partial x}\right|_{x=L} = 0 \tag{1.11}$$

A zero flux boundary condition is applied at both the boundaries to bolster the idea of conservation of charge in the electrolyte phase. However, this condition leads to redundancies.

1.3.1.5 Rate of Reaction, j_{Li}

The Butler-Volmer equation is used to calculate the reaction rate at the electrode-electrolyte interface.

$$j_{Li} = i_0 \left(exp\left(\frac{\alpha_{an} F \eta}{RT}\right) - exp\left(-\frac{\alpha_{ca} F \eta}{RT}\right)\right) \tag{1.12}$$

j_{Li} is a coupling term that captures the thermodynamic and kinetic effects of the redox reactions. i_0 is the exchange current density that models the kinetics of the reactions and is given by,

$$i_0 = k_{an}^{\alpha_{ca}} k_{ca}^{\alpha_{an}} (c_{s,max} - c_{s,surf})^{\alpha_{ca}} (c_e)^{\alpha_{an}} (c_{s,surf})^{\alpha_{an}} \tag{1.13}$$

$\eta (= \phi_s - \phi_e - U(c_{s,surf}))$ is the overpotential, α is the electrode transfer coefficient and it denotes the fraction of potential driving the reaction at a particular electrode. Equation 1.12 consists of two parameters that can be determined only through experiments: U and k. U is the open-circuit voltage of an electrode material at a given lithium ion concentration, and k is the reaction rate constant for the redox reaction taking place at each electrode.

1.3.1.6 Constituent Parameters

To complete the physics-based model presented in the previous sections, a multitude of parameters need to be determined, either through experiments or through existing material data. As seen in previous sections, effective properties are employed to take porosity, concentration and temperature variations into account. Consider σ^{eff},

$$\sigma^{eff} = \sigma(1 - \varepsilon) \tag{1.14}$$

where σ is the ionic conductivity of the given material and ε is its porosity.

The effective diffusivities of electrolyte incorporate the effect of tortuosity of the porous solid matrix through the Bruggeman porosity exponent p.

$$D_e^{eff} = \varepsilon^p D_e(c_e, T) \tag{1.15}$$

$$\kappa^{eff} = \varepsilon^p \kappa(c_e, T) \tag{1.16}$$

D_e and κ are empirical relations that are derived through function-fitting of experimental data.

The active surface area per unit volume of the electrode a_s is calculated using a simple correlation,

$$a_s = \frac{3\varepsilon_s}{R_s} \tag{1.17}$$

Note that ε_s denotes the fraction of active material per unit volume, whereas ε denotes the fraction of electrolyte per unit volume or porosity.

The temperature dependence of solid diffusivities D_s and kinetic constants k is generally modeled using the Arrhenius relationship,

$$\psi = \psi_{ref}\ exp\left(-\frac{E_a}{R}\left(\frac{1}{T} - \frac{1}{T_{ref}}\right)\right) \tag{1.18}$$

A table to summarize the parameters is shown below.

Category	Parameter	Units (SI)	Description
Geometric	a_s	m^{-1}	Active surface area to volume ratio, Defined only for electrodes, $a_s = \frac{3\varepsilon}{R_s}$
	L_n, L_s, L_p	m	Length of each region in LIB
	R_s	m	Radius of the model sphere, Defined only for electrodes
	ε	$-$	Porosity, Defined for all regions
Transport	D_e	$m^2 s^{-1}$	Lithium ion diffusivity in electrolyte, Defined for all regions, Generally, $D_e = f(c_e, T)$
	D_s	$m^2 s^{-1}$	Lithium ion diffusivity in solid phase, Defined only for electrodes
	t_+	$-$	Cation transference number, Defined for all regions, Generally, $t_+ = 0.363$ for Li-ion
	κ	$S\ m^{-1}$	Ionic conductivity in electrolyte, Defined for all regions, Generally, $\kappa = f(c_e, T)$
	σ	$S\ m^{-1}$	Ionic conductivity in solid phase, Defined only for electrodes
Kinetic	k	$m^{2.5} mol^{-0.5} s^{-1}$	Reaction rate constant, Defined only for electrodes
	α	$-$	Electrode transfer coefficient, Defined only for electrodes, $\alpha = 0.5$ for 1^{st} order reaction
Thermodynamic	U	V	Open-circuit voltage, Defined only for electrodes, Determined experimentally
	$c_{s,max}$	$mol\ m^{-3}$	Maximum solid concentration in electrode material
	R	$Jmol^{-1}K^{-1}$	Universal Gas Constant, $R = 8.314$ in SI units
	F	$A\ s\ mol^{-1}$	Faraday's Constant, $F = 96485$ in SI units

Table 1.1: Constituent parameters

1.3.2 Thermal Behaviour

Building up on the 1D case, the heat generation terms [23] pertaining to LIBs are explained in this section. The differential form of the energy conservation equation within the LIB is given by,

$$\rho c_p \frac{\partial T}{\partial t} = \frac{\partial}{\partial x}\left(\lambda \frac{\partial T}{\partial x}\right) + \dot{q}'''_{tot} \tag{1.19}$$

where λ is the thermal conductivity, ρ is the density, and c_p is the specific heat capacity measure at constant pressure condition.

The total heat generation in LIBs can be attributed to many mechanisms, like Joule heating, reversible entropic heat generation, ohmic heat due to concentration and potential gradients within the cell. The volumetric heat generation term $\dot{q}'''_{tot}$ is generally given by,

$$\dot{q}'''_{tot} = \dot{q}'''_{irr} + \dot{q}'''_{rev} + \dot{q}'''_{ohm} \tag{1.20}$$

where $\dot{q}'''_{irr}$ is the irreversible heat generation term, $\dot{q}'''_{rev}$ is the reversible heat generation term and $\dot{q}'''_{ohm}$ is the ohmic heat generation term. Each of those terms can be expressed as follows,

$$\dot{q}'''_{irr} = a_s F j_{Li}(\phi_s - \phi_e - U) \tag{1.21}$$

The irreversible heat generation term arises from the charge transfer reactions taking place at the electrode-electrolyte interface. This term is exothermic regardless of whether the battery is being charged or discharged.

$$\dot{q}'''_{rev} = a_s F j_{Li} T \frac{dU}{dT} \tag{1.22}$$

The reversible heat generation term arises due to the change in entropy that occurs during the intercalation/de-intercalation of lithium ions. It can be endothermic or exothermic depending on the sign of the rate of reaction and $\frac{dU}{dT}$.

$$\dot{q}'''_{ohm} = \sigma_{eff}\left(\frac{\partial \phi_s}{\partial x}\right)^2 + \kappa_{eff}\left(\frac{\partial \phi_e}{\partial x}\right)^2 + \frac{2RT\kappa_{eff}}{F}(1-t_+)\left(\frac{\partial \phi_e}{\partial x}\right)\left(\frac{\partial ln(c_e)}{\partial x}\right) \quad (1.23)$$

The ohmic term is generally smaller than the other source terms. It arises due to the passage of current through the solid and electrolyte regions.

Depending on the LIB surrounding, the boundary conditions may vary. The most commonly used boundary condition being the convective boundary condition. For the 1D case, we have,

$$-\lambda\frac{\partial T}{\partial x}\bigg|_{x=0} = -h(T_{x=0} - T_\infty) \quad \text{and} \quad -\lambda\frac{\partial T}{\partial x}\bigg|_{x=L} = h(T_{x=L} - T_\infty) \quad (1.24)$$

1.3.2.1 Lumped Thermal Assumption

The assumption of a uniform cell temperature for heat transfer analysis has become increasingly popular due to its low computational cost and first-order representation of the physics involved. In this model, heat transfer due to conduction within the cell is assumed to be infinitely large, thus, removing the spatial dependence of temperature and heat sources. The simplified version of equation 1.19 is given by,

$$mc_p\frac{dT}{dt} = \dot{q}_{tot} + \dot{q}_{loss} \quad (1.25)$$

In this simplified version, $\dot{q}_{tot}$ reduces to just a sum of irreversible and reversible heat sources. Note that the ohmic heat generation term occurs due to the spatial variation of concentrations and potentials in the solid and liquid phases, however, for the lumped model, spatial variation is assumed to be zero. Mathematically, the generation term looks like,

$$\dot{q}_{tot} = I(U - V) - IT\frac{dU}{dT} \quad (1.26)$$

In equation (1.26), the first term $I(U - V)$ is the lumped irreversible term. It can be viewed as the I^2R_{int} loss where R_{int} is the internal resistance of the battery. The second term $-IT\frac{dU}{dT}$ is the lumped reversible heat term. This term captures the heat generated due to entropy change and takes into account the variation of the open-circuit voltage with temperature.

The heat loss term $\dot{q}_{loss}$ is the sum of all the heat losses that the battery experiences. For most setups, heat loss occurs due to convection and radiation. For the lumped model, $\dot{q}_{loss}$ is given by,

$$\dot{q}_{loss} = -hA_{cell}(T - T_\infty) - \epsilon\sigma_{SB}A_{cell}(T^4 - T_\infty^4) \tag{1.27}$$

The first term in equation (1.27) represents convection and the second term represents radiation. h is the heat transfer coefficient, ϵ is the emissivity of the battery surface, A_{cell} is the cross-section area of the battery across which the current flows and σ_{SB} is the Stephan-Boltzmann constant.

The validity of this lumped model is analyzed using the Biot number, Bi. It is defined as the ratio of the heat transfer due to conduction within a body to the heat transfer due to convection at the surface of the said body,

$$Bi = \frac{hL_c}{\lambda} \tag{1.28}$$

According to [24], a lumped thermal model can be used if the Bi is less than 0.1. For the pouch cell considered in this study, $L_c = 4.3\ mm$ and the typical value of thermal conductivity within the cells (across-plane) can be taken as $1.667\ Wm^{-1}K^{-1}$ (volume averaged value obtained from Torchio et al [20]). Thus, we get,

$$\frac{hL_c}{\lambda} < 0.1 \Rightarrow \boxed{h < 38.76\ Wm^{-2}K^{-1}} \tag{1.29}$$

Thus, the maximum allowable heat transfer coefficient comes out to be $38.76\ Wm^{-2}K^{-1}$. The lumped thermal model for the considered battery geometry is valid over the

entire range of air natural convection heat transfer coefficient, which typically is 2 to 25 $Wm^{-2}K^{-1}$ [25].

1.3.3 Ageing Mechanism

Capacity fade and degradation of LIBs are majorly caused by the formation of the solid-electrolyte interface (SEI) layer in the first few cycles [26]. Other mechanisms can cause irreversible capacity loss like electrolyte breakdown, the phase change of separator, and many other processes, however, their contribution is negligible when it comes to the initial battery cycling stage at normal temperatures.

The SEI layer typically forms at the anode interface; however, it can occur at the cathode surface as well. This layer gets formed due to the reaction between the organic electrolyte and active lithium at the anode surface. The SEI film affects battery life in two ways. Firstly, the film formation decreases the total amount of lithium ions available for charge transfer, thus, reducing the capacity of the cell. Secondly, the SEI layer acts as an impedance to the diffusion of electrolyte to the anode surface, which leads to an increase in the internal resistance of the LIB. Despite the aforementioned disadvantages, the SEI layer plays an important role in protecting the anode from further degradation. Hence, it's presence is considered to be a "necessary evil" for battery functioning.

The SEI layer is generally a dense, thin film of reduced electrolyte species that stick to the anode surface. They exhibit low electrolyte permeability, which is why an increased resistance is observed in an aged LIB.

A simple diffusion-based model is presented by Ploehn et al [27] that agrees with the experimental evidence of battery ageing. Mathematically, they showed,

$$s = \gamma\sqrt{D_{SEI}t} \tag{1.30}$$

where s is the thickness of the SEI layer, D_{SEI} is the solvent diffusivity in SEI, t is time, and γ is a constant. The main takeaway from this model is that the thickness

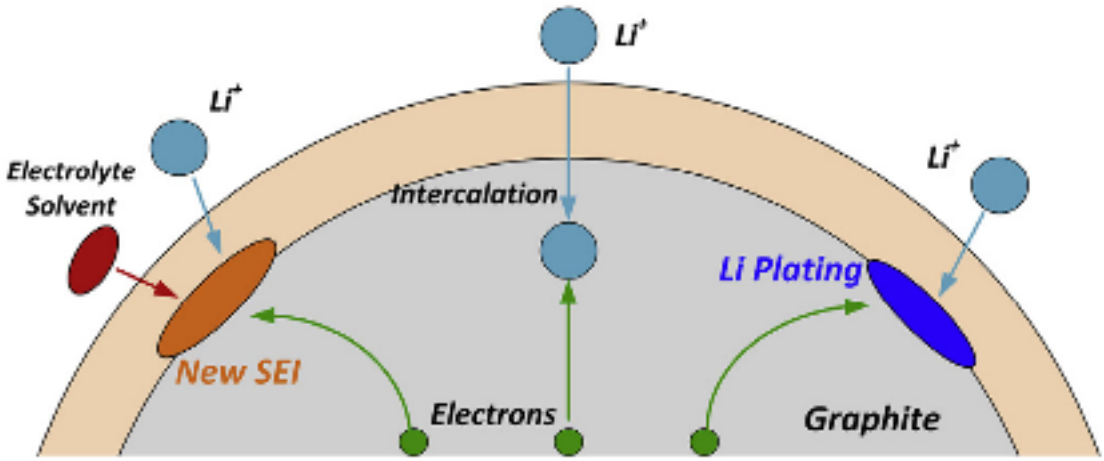

Figure 1.5: Possible reactions at the anode surface during LIB charging [29]

of the SEI layer is directly proportional to the square root of time.

Sticking to the spherical representation of the LIB electrodes, Pinson [28] extended the previously developed physics to porous electrode theory, taking into account the rate of reaction j_{Li}. They also included temperature dependency by introducing an Arrhenius representation of the solvent diffusivity.

Another significant degradation mechanism that occurs in LIB is lithium plating [30]. When excess lithium ions are supplied to the anode, the surplus ions adhere to the anode surface as metallic lithium, which leads to capacity loss. The lithium metal is deposited in the form of dendrites and can lead to an internal short circuit. It is mainly caused by low temperature operation or high charge rates. Using the nomenclature employed in the above sections, lithium plating occurs when the overpotential of the LIB anode becomes negative ($\eta < 0$).

1.4 Cell Abuse

The understanding of cell abuse mechanisms is of utmost importance, especially for LIBs with high energy density which have lower thermal stability [31]. They are broadly classified into 3 groups: thermal abuse, mechanical abuse, and electrical abuse [32].

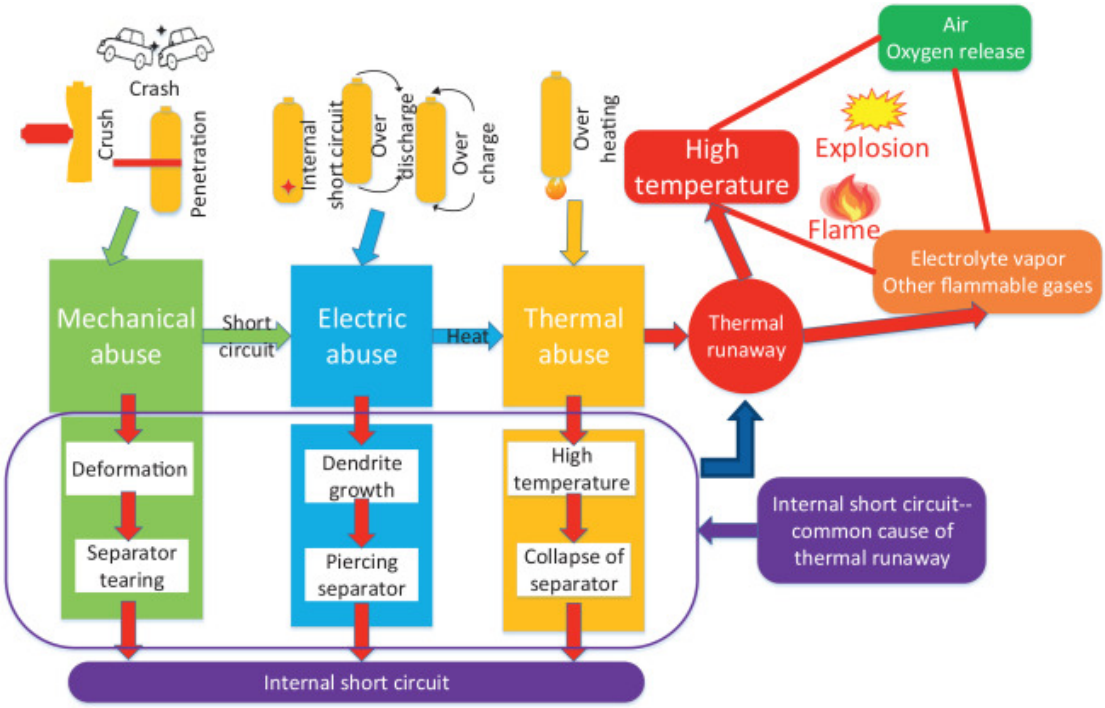

Figure 1.6: LIB failure mechanisms [33]

Figure 1.6 illustrates different pathways to cell failure. It needs to be pointed out that almost all mechanisms lead to an internal short circuit (ISC), which causes the sudden release of electrical energy. ISC has been specified as the main reason behind LIB failures [34]. Mechanical abuse mechanisms entail ISC commencement due to the physical deformation of the LIB, processes like nail penetration or rapid bending [35, 36] lead to mechanical failure.

Electrical abuse mechanisms include overcharge, overdischarge, and external short circuits [37, 38]. The dendrite growth associated with overcharge or low temperature functioning can rupture the separator [39], eventually making contact with the anode to induce ISC. In extreme cases, overdischarging reverses the poles of the battery, which then gives rise to abnormal heat generation in the LIB. Otherwise, charging an overdischarged cell leads to the formation of an unstable SEI layer, which leads to rapid capacity fade [40].

Apart from melting the separator, thermal abuse can also trigger degradation reactions between anode and electrolyte or cathode and electrolyte, which are exothermic in nature [41]. These exothermic reactions stack up, meaning, as temperature increases due to one reaction, another exothermic reaction gets initiated. The end

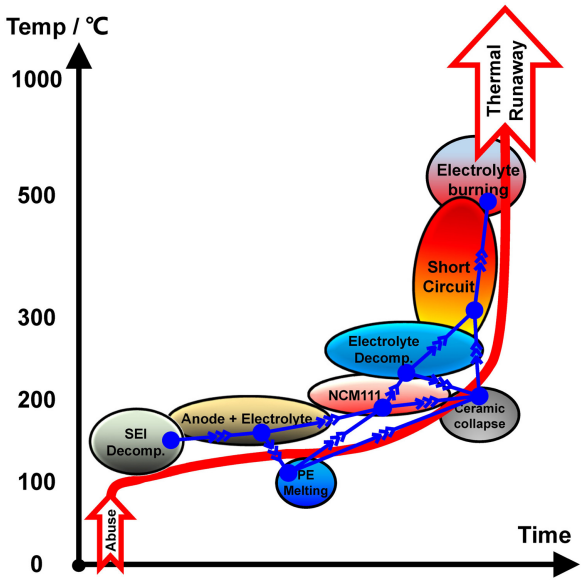

Figure 1.7: Chain reaction progression in thermal runaway [38]

result of these chain reactions is thermal runaway (TR) in which the LIB reaches very high temperatures (around 600-1000°C) and releases vent gases. Manufacturing defects can also set off ISC.

1.4.1 Thermal Runaway Characterization

TR is a product of exothermic chain reactions as shown in figure 1.7. A common trend in the onset temperatures of the reactions has been observed.

The first exothermic process that is generally observed is SEI decomposition, starting at around 80°C [38]. Other reactions can begin simultaneously. For example, the breakdown of the separator (endothermic) and the anode-electrolyte reaction can get triggered at around 120°C . Depending on the cathode material, the cathode-electrolyte reaction can start at a temperature anywhere between 180-280°C. Doughty [42] compared the thermal stability of cathode materials. The order of stability comes out to be $LFP > LMO > NCM111 > NCA > LCO$. Kawamura et al [43] studied the electrolyte ($LiPF_6$) decomposition process and observed exothermic peaks at 230°C and 280°C.

The rate of all the reactions can be represented using a generalized Arrhenius equa-

tion,

$$\frac{dc_i}{dt} = A_i c_i^{n_{i,1}} (1 - c_i)^{n_{i,2}} exp\left(-\frac{E_{a,i}}{RT}\right) \tag{1.31}$$

where c_i represents the normalized concentration of the reactant in the i^{th} reaction. The reactions that are generally considered are: SEI decomposition and regeneration, anode-electrolyte reaction, separator breakdown, cathode-electrolyte reaction, and electrolyte decomposition. A is the pre-exponential factor, E_a is the activation energy, $n_{i,1}$ and $n_{i,2}$ represent the order of the reaction i. R and T stand for universal gas constant and temperature respectively. One set of kinetic parameters is tabulated in Feng [38].

The heat generation term pertaining to reaction i can be related to its reaction rate in the following manner,

$$Q_i = -\Delta H_i m_i \frac{dc_i}{dt} \qquad (T > T_{onset,i}) \tag{1.32}$$

where ΔH represents the enthalpy of reaction i, m_i is the total mass of species i inside the LIB, and $T_{onset,i}$ is the temperature at which reaction i begins. The negative sign depicts the exothermic nature of the decomposition reaction.

1.5 Research Objective

The objective of this thesis is two-fold. The first is to give an overview of different modeling methods employed to simulate LIB behavior. The second is to extend one of the modeling methods to understand the connection between battery operation and thermal runaway. A better understanding of this connection will immensely improve the state of the current battery management systems. One application that will directly get impacted is the fast charging of EV batteries. Recently, in August 2019, a Hyundai Kona Electric vehicle caught fire while being charged. Several such incidents have occurred since 2010 [33, 38], thus, making this study imperative from a safety point of view.

The majority of literature either characterizes normal battery use or studies ther-

mal runaway exclusively. Very few researchers have attempted to predict thermal runaway while simulating the thermo-electrochemical behavior of the battery. This thesis will attempt to extend one model in order to attain a better understanding of LIBs over a wider range of temperatures.

Chapter two deals with various methodologies studied by researchers. Each subsection covers the explanation and implementation of different methods. The most commonly implemented P2D model and the equivalent-circuit model (ECM), used in this thesis, are explored in great detail.

Chapter three shows P2D results for LIBs subjected to different thermal conditions. Abuse conditions like low heat transfer coefficient, high current, and high ambient temperature are simulated using the standard P2D model. Its shortcomings and motivation behind the switch to ECM are addressed.

Chapter four and five cover the procedure used for the characterization and prediction of LIB behavior at high temperatures. Cases with different current profiles, which try to push the battery to its limits, are presented along with the model results. Additionally, a case of failure due to cyclic overcharging is also shown.

2 Modeling Methodologies

Researchers have developed various ways of modeling LIBs which can be roughly classified into physics-based methods, circuit-based models, and data-based machine learning models. Emphasis is placed on the application of the first two modeling methods.

2.1 Multi-Physics Models

This section briefly expounds upon spatial and temporal discretization schemes of the P2D model, a few simplifications, and solution techniques. The mathematical models described in sections 1.3.1 and 1.3.2 form the basis of physics-based simulation of LIBs. The differential equations described are coupled and highly non-linear. Their discretization gives rise to a stiff system of equations that needs to be solved with caution to avoid instabilities in the numerical solution.

Several simplifications have been proposed to reduce the complexity of the system of equations to aid quick computation. Zhang et al [44] eliminated the macro-scale spatial dependence by modeling the electrodes as single spheres (SPM model) of respective compounds. Subramanian [8] utilized the concept of volume-averaging to come up with an analytical parabolic profile (PP model) solution for solid diffusion in the model spheres that are used in the P2D model. Several such simplifications have been summarized in Jokar[18] and Ramadesigan [45]. These modifications significantly speed up the simulations; however, they face the issue of compromised accuracy when LIB behavior is modeled under certain operating conditions like high current or low/high temperatures.

The order of accuracy and computational complexity can thus be expressed as P2D > P2DPP > SPM. P2D results are generally considered to be the benchmark for

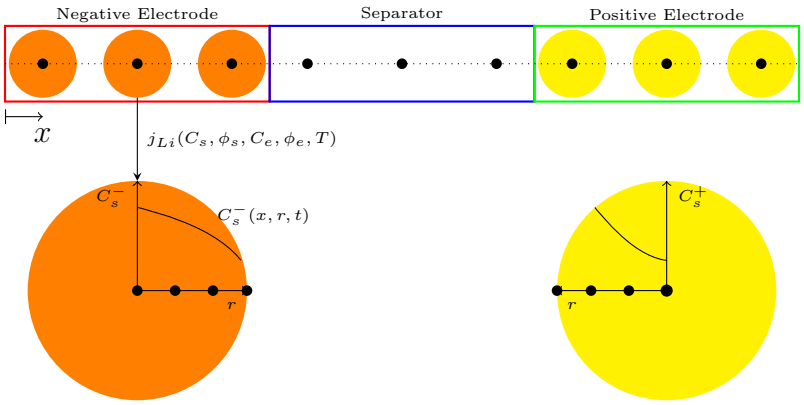

Figure 2.1: P2D discretization

the validation of other reformulated models. However, solving a full-blown P2D model without any simplifications is very taxing in terms of computational time and storage. Reformulated models like the PP model strike a nice balance between accuracy and computational cost. The SPM model, however, has very limited applicability, restricted to low current usage.

2.1.1 Spatial Discretization for P2D model

The computational domain is divided into two regimes: macro-scale and micro-scale. The macro-scale dimension refers to dimensions that are commensurate with the thickness of the electrodes (typically 10-100 μm). Micro-scale refers to lengths that are in proportion to the particle size of the constituent electrode compounds (around 1 μm). The coordinate system illustrated in figure 1.4 is followed for numerical analysis. The x-direction represents the macro-scale regime. As shown in figure 2.1, the spheres are arranged on a 1D x-direction grid. Each sphere models solid phase diffusion at its x coordinate. To solve for solid phase diffusion, a micro-scale grid is defined within each sphere. The r-grid (vertical grid in figure 2.2) represents the mesh for spherical solid diffusion and the vertical grid point that coincides with the x-grid point represents the center of the model sphere.

Various discretization schemes have been established for numerical modeling of differential equations. Three main methodologies are implemented for spatial analysis: Finite Volume Method (FVM), Finite Element Method (FEM) and Finite Difference

Method (FDM). A schematic to show how each scheme slices the computational domain is given in figure 2.2. The FVM scheme involves division of the computational domains into control volumes, the FEM scheme involves partitioning of the domain into elements, and FDM scheme simply maps the domain onto a grid. The mesh required for LIB P2D model is same for FDM and FEM schemes. For a case with large number of grid points, all 3 schemes converge to a common solution.

2.1.1.1 Finite Volume Method Basics

As described before, FVM scheme involves division of domain into small control volumes. The FVM grid in x-direction for the P2D model is shown in figure 2.2. Mathematically, the FVM discretization of a variable u on a 1D x-grid requires the following tools,

$$\left.\frac{\partial u}{\partial x}\right|_i = \frac{u_{i+1/2} - u_{i-1/2}}{\delta x_i} \tag{2.1}$$

The values of $u_{i+1/2}$ and $u_{i-1/2}$ can be obtained either from the upwind difference scheme ($u_{i+1/2} = u_i$ and $u_{i-1/2} = u_{i-1}$) or the central difference scheme ($u_{i+1/2} = (u_i + u_{i+1})/2$ and $u_{i-1/2} = (u_i + u_{i-1})/2$). The second derivative can be expanded as follow

$$\left.\frac{\partial}{\partial x}\left(D\frac{\partial u}{\partial x}\right)\right|_i = \frac{D_{i+1/2}\left.\frac{\partial u}{\partial x}\right|_{i+1/2} - D_{i-1/2}\left.\frac{\partial u}{\partial x}\right|_{i-1/2}}{\delta x_i} \tag{2.2}$$

$$= \frac{D_{i+1/2}\frac{u_{i+1}-u_i}{(\delta x_{i+1}+\delta x_i)/2} - D_{i-1/2}\frac{u_i-u_{i-1}}{(\delta x_{i-1}+\delta x_i)/2}}{\delta x_i} \tag{2.3}$$

If we consider a regular 1D grid with constant diffusivity D, equation 2.2 reduces to,

$$\left.\frac{\partial}{\partial x}\left(D\frac{\partial u}{\partial x}\right)\right|_i = D\frac{u_{i+1} + u_{i-1} - 2u_i}{\delta x^2} \tag{2.4}$$

Consider a sample problem of the advection-diffusion-reaction PDE,

$$ru + \vec{a}.\nabla u - \nabla(\kappa\nabla u) = f \tag{2.5}$$

Here, r is the reaction coefficient, $\vec{a}$ is the velocity, κ is the diffusivity, and f is the source term. Using the discretization scheme explained above, the given PDE in

1D can be written in the form,

$$A_{i+1}u_{i+1} + A_{i-1}u_{i-1} + A_i u_i = F_i \qquad \text{for } i \in [1, N-1] \tag{2.6}$$

where A_i represent the coefficient of u_i. N is the total number of finite volumes used to discretize the domain. The range $i \in [1, N-1]$ is valid when only dirichlet conditions exist in the problem, the range can change depending on the boundary conditions. F_i encapsulates the effect of the source terms and dirichlet boundary conditions. In a matrix form,

$$\mathbf{A}\vec{u} = \vec{F} \tag{2.7}$$

$\mathbf{A}$ is the coefficient matrix, each entry in $\vec{u}$ represents the FVM solution at the respective control volume centre, and $\vec{F}$ is the source term vector. Thus, the PDE system is reduced to a linear algebra problem. A multitude of techniques exist for quick and efficient solution of such matrix systems [46].

2.1.1.2 Finite Element Method Basics

Usage of FEM requires rigorous mathematics, thus, only a brief explanation is given in this work. FEM always begins with the setup of a weak form of the PDE in consideration. Building up on the same advection-diffusion-reaction PDE, assume that the actual solution $u \in \{H^1(\Omega)|u = g \text{ on } \Gamma_g\} \equiv \mathcal{S}$ where $H^1(\Omega)$ is a sobolev space that consists of functions (and their derivatives) that are square integrable over the domain Ω. g represents the dirichlet boundary condition defined on the boundary Γ_g. $\mathcal{S}$ is known as the trial solution space.

Consider a function $w \in \{H^1(\Omega)|w = 0 \text{ on } \Gamma_g\} \equiv \mathcal{V}$. $\mathcal{V}$ is commonly known as the test solution space. To form a weak form, multiply w to equation 2.5 and integrate over the whole domain.

$$\int_\Omega (rwu + w\vec{a}.\nabla u - w\nabla(\kappa\nabla u))d\Omega = \int_\Omega wf d\Omega \tag{2.8}$$

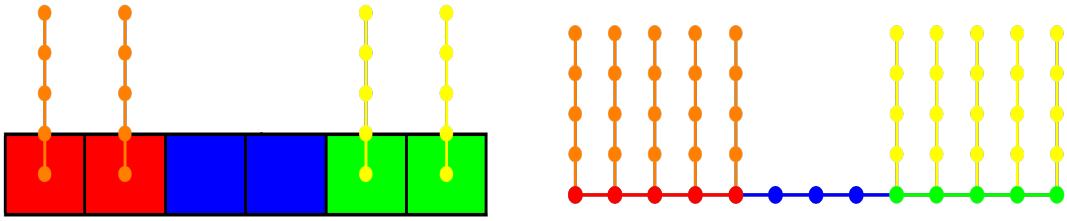

(a) FVM scheme

(b) FEM/FDM scheme

Figure 2.2: Discretization of LIB computational domain

Using integration by parts, we get

$$\int_{\Omega}(rwu + w\vec{a}.\nabla u + \nabla w.(\kappa\nabla u))d\Omega = \int_{\Omega} wfd\Omega + \int_{\Gamma_h} w\nabla u.\vec{n}d\Gamma \tag{2.9}$$

To get a Galerkin FEM solution, u and w are replaced with u^h and w^h where the latter represents approximate solutions that are continuous across each element. The approximate spaces are defined as: $u^h \in$ {Piece-wise polynomials of order k $|u^h = g$ on $\Gamma_g\} \equiv \mathcal{S}^h \subset \mathcal{S}$ and $w \in$ {Piece-wise polynomials of order k $|w^h = 0$ on $\Gamma_g\} \equiv \mathcal{V}^h \subset \mathcal{V}$.

Thus, the general forms of u^h and w^h can be written as (assuming 1D),

$$u^h(x) = \sum_N c_i N_{1,i}(x) \tag{2.10}$$

$$w^h(x) = \sum_N d_i N_{2,i}(x) \tag{2.11}$$

where N is the total number of elements, c_i and d_i are coefficients of the piece-wise functions $N_{1,i}$ and $N_{2,i}$ respectively. These approximations are then substituted into the weak form. The new form is manipulated to obtain a matrix equation,

$$\mathbf{K}\vec{d} = \vec{F} \tag{2.12}$$

where $\mathbf{K}$ is the stiffness matrix, which is a function of N_1 and N_2. $\vec{d}$ is a vector that stores the nodal point solutions and $\vec{F}$ captures the effect of source terms and dirichlet boundary conditions. Hence, FEM also reduces the posed PDE problem to a linear algebra problem.

Solid Diffusion

For spherical diffusion, FDM is commonly used for discretization. For a uniform r-grid made up of n_r points, the grid spacing is given by $\delta_r = R_p/(n_r - 1)$. The distance of the i^{th} grid point from the centre of the sphere is given by $r_i = \delta_r i$ where $i \in [0, n_r - 1]$. $i = 0$ and $i = n_r - 1$ denote the centre point and surface point respectively. The FDM discretization of equation 1.1 is given by,

$$\frac{\partial c_s(x, r_i, t)}{\partial t} = D_s(x) \left[\frac{r_{i+1} c_s(x, r_{i+1}, t) + r_{i-1} c_s(x, r_{i-1}, t) - 2 r_i c_s(x, r_i, t)}{r_i \delta_r^2} \right] \quad (2.13)$$

where $i \in [1, n_r - 2]$. Boundary conditions are discretized in the following manner,

$$c_s(x, r_0, t) - c_s(x, r_1, t) = 0 \quad (2.14)$$

$$c_s(x, r_{n_r-1}, t) - c_s(x, r_{n_r-2}, t) = -\frac{j_{Li} \delta_r}{D_s(x)} \quad (2.15)$$

The boundary conditions can be combined with the domain discretization equation to give (x and t have been omitted from the notation to improve legibility),

$$\frac{\partial c_s(r_i)}{\partial t} = \begin{cases} 2D_s \frac{c_s(r_1) - c_s(r_0)}{\delta_r^2} & \text{for } i = 0, \\ D_s \left[\frac{r_{i+1} c_s(r_{i+1}) + r_{i-1} c_s(r_{i-1}) - 2 r_i c_s(r_i)}{r_i \delta_r^2} \right] & \text{for } i \in [1, n_r - 2], \\ 2D_s \frac{c_s(r_{n_r-2}) - c_s(r_{n_r-1})}{\delta_r^2} - \frac{2n_r}{R_p} j_{Li} & \text{for } i = n_r - 1 \end{cases} \quad (2.16)$$

In order to combine the equations 2.13, 2.14 and 2.15, one has to use the concept of ghost points at the boundaries. This method entails addition of 2 nodes, one at $i = -1$ and other at $i = n_r$. The domain discretization is then written for all nodes $i \in [0, n_r - 1]$. The boundary conditions are modified using the central difference scheme, after which they are utilized to eliminate $c_s(r_{-1})$ and $c_s(r_{n_r})$ from the domain discretization equation.

Electrolyte Diffusion

The process of electrolyte diffusion only takes place along the x-direction for this P2D model. Any of the three schemes (FVM, FEM or FDM) can be used for the discretization of equation 1.4.

Starting with FVM, assume there are n_x control volumes in total, out of which n_n belong to the negative electrode region, n_s belong to the separator region and n_p form the positive electrode region. Note that $n_x = n_n + n_s + n_p$.

The FVM scheme described in subsection 2.1.1.1 can be readily applied to equation 1.4,

$$\varepsilon_i \frac{\partial c_{e,i}}{\partial t} = \begin{cases} 2\frac{D^{eff}_{e,i+1/2}(c_{e,i+1}-c_{e,i})}{\delta x_i(\delta x_i+\delta x_{i+1})} + a_{s,i}(1-t_+)j_{Li,i} & \text{for } i=0, \\ \frac{1}{\delta x_i}\left[D^{eff}_{e,i+1/2}\left.\frac{\partial c_e}{\partial x}\right|_{i+1/2} - D^{eff}_{e,i-1/2}\left.\frac{\partial c_e}{\partial x}\right|_{i-1/2}\right] + a_{s,i}(1-t_+)j_{Li,i} & \\ & \text{for } i \in [1, n_x-2], \\ 2\frac{D^{eff}_{e,i-1/2}(c_{e,i-1}-c_{e,i})}{\delta x_i(\delta x_i+\delta x_{i-1})} + a_{s,i}(1-t_+)j_{Li,i} & \text{for } i=n_x-1 \end{cases} \tag{2.17}$$

To proceed with FEM, a weak form of equation 1.4 is constructed. It is given by,

$$\int_L \varepsilon \frac{\partial c^h_e}{\partial t} w^h dx = -\int_L \left(\varepsilon D^{eff}_e \frac{\partial c^h_e}{\partial x}\frac{\partial w^h}{\partial x}\right) dx + \int_L a_s(1-t_+) j^h_{Li} w^h dx \tag{2.18}$$

Zero flux boundary condition is already taken care of in the weak form.

Solid and Electrolyte Potential

The potential equations for the solid and electrolyte phases do not contain explicit time dependence, thus, they are termed as algebraic constraints. These constraints have to be satisfied at each step for the solution to proceed to next time step. Their discretization is straight-forward using both, FVM and FEM.

The FVM discretization of the solid potential equation is given by,

$$0 = \begin{cases} \frac{2\frac{\sigma^{eff}_{i+1/2}(\phi_{s,i+1}-\phi_{s,i})}{\delta x_i+\delta x_{i+1}} + a_{s,i}Fj_{Li,i}\delta x_i + \alpha_1}{} & \text{for } i = \beta_1, \\ \sigma^{eff}_{i+1/2}\left.\frac{\partial\phi_s}{\partial x}\right|_{i+1/2} - \sigma^{eff}_{i-1/2}\left.\frac{\partial\phi_s}{\partial x}\right|_{i-1/2} + a_{s,i}Fj_{Li,i}\delta x_i & \\ \qquad\qquad \text{for } i \in [\beta_1+1, \beta_2-1], & \\ \frac{2\frac{\sigma^{eff}_{i-1/2}(\phi_{s,i-1}-\phi_{s,i})}{\delta x_i+\delta x_{i-1}} + a_{s,i}Fj_{Li,i}\delta x_i + \alpha_2}{} & \text{for } i = \beta_2 \end{cases} \tag{2.19}$$

For the negative electrode, $\beta_1 = 0$, $\beta_2 = n_n - 1$, $\alpha_1 = I_{app}$, and $\alpha_2 = 0$. For the positive electrode, $\beta_1 = n_n + n_s$, $\beta_2 = n_x - 1$, $\alpha_1 = 0$, and $\alpha_2 = I_{app}$.

Using FEM, the solid potential equation can be discretized as,

$$\begin{aligned} 0 = -\int_{L_{\beta_1}}^{L_{\beta_2}} \left(\sigma^{eff}\frac{\partial\phi_s^h}{\partial x}\frac{\partial w^h}{\partial x}\right)dx + \int_{L_{\beta_1}}^{L_{\beta_2}} a_s F j_{Li}^h w^h dx \\ + \left[\sigma^{eff}\frac{\partial\phi_s^h}{\partial x}w^h\right]_{x=L_{\beta_1}}^{x=L_{\beta_2}} \end{aligned} \tag{2.20}$$

Similarly, the electrolyte potential equation can be discretized as,

$$0 = \begin{cases} \frac{2\frac{\kappa^{eff}_{i+1/2}(\phi_{e,i+1}-\phi_{e,i})}{\delta x_i+\delta x_{i+1}} + 2\frac{\kappa^{eff}_{d,i+1/2}(lnc_{e,i+1}-lnc_{e,i})}{\delta x_i+\delta x_{i+1}} + a_{s,i}Fj_{Li,i}\delta x_i}{} & \text{for } i = 0, \\ \frac{1}{\delta x_i}\left[\kappa^{eff}_{i+1/2}\left.\frac{\partial\phi_e}{\partial x}\right|_{i+1/2} - \kappa^{eff}_{i-1/2}\left.\frac{\partial\phi_e}{\partial x}\right|_{i-1/2}\right] + a_{s,i}Fj_{Li,i}\delta x_i & \\ +\frac{1}{\delta x_i}\left[\kappa^{eff}_{d,i+1/2}\left.\frac{\partial lnc_e}{\partial x}\right|_{i+1/2} - \kappa^{eff}_{d,i-1/2}\left.\frac{\partial lnc_e}{\partial x}\right|_{i-1/2}\right] & \text{for } i \in [1, n_x-2], \\ \frac{2\frac{\kappa^{eff}_{i-1/2}(\phi_{e,i-1}-\phi_{e,i})}{\delta x_i+\delta x_{i-1}} + 2\frac{\kappa^{eff}_{d,i-1/2}(lnc_{e,i-1}-lnc_{e,i})}{\delta x_i+\delta x_{i-1}} + a_{s,i}Fj_{Li,i}\delta x_i}{} & \text{for } i = n_x - 1 \end{cases} \tag{2.21}$$

where $\kappa_d = \frac{2RT\kappa}{F}(1-t_+)$. The equation form may look complex, yet, it is easier to implement in code since the basic procedure of discretization stays the same.

The weak form of the 1D electrolyte potential equation is given by,

$$\begin{aligned} 0 = -\int_L \left(\kappa_e^{eff}\frac{\partial\phi_e^h}{\partial x}\frac{\partial w^h}{\partial x}\right)dx - \int_L \left(\kappa_{d,e}^{eff}\frac{\partial lnc_e^h}{\partial x}\frac{\partial w^h}{\partial x}\right) \\ + \int_L a_s F j_{Li}^h w^h dx + \left[\kappa_e^{eff}\frac{\partial\phi_e^h}{\partial x}w^h\right]_{x=0}^{x=L} \end{aligned} \tag{2.22}$$

2.1.1.3 Time Integration

Once the equations are spatially discretized and written in matrix notation, the P2D equations reduce to,

$$\mathbf{B}\frac{\partial \vec{u}(t)}{\partial t} = \mathbf{A}(\vec{u}(t)).\vec{u}(t) + \vec{F}(\vec{u}(t)) + \vec{D}i_{app}(t) \tag{2.23}$$

For FVM, these vectors and matrices denote,

$$\vec{u} = [\ \vec{c_s}^T\ \vec{c_e}^T\ \vec{\phi_s}^T\ \vec{\phi_e}^T\ ]_{1\times 2n_x+(n_r+1)(n_p+n_n)} \tag{2.24}$$

$$\vec{F} = [\ \vec{F}_{c_s}^T\ \vec{F}_{c_e}^T\ \vec{F}_{\phi_s}^T\ \vec{F}_{\phi_e}^T]_{1\times 2n_x+(n_r+1)(n_p+n_n)} \tag{2.25}$$

$$\vec{D} = [\vec{0}_{1\times(n_x+n_r(n_p+n_n))}^T\ 1\ \vec{0}_{1\times(n_p+n_n-1)}^T\ -1\ \vec{0}_{1\times nx}^T] \tag{2.26}$$

$$\mathbf{A} = diag(\mathbf{A}_{c_s}\ \mathbf{A}_{c_e}\ \mathbf{A}_{\phi_s}\ \mathbf{A}_{\phi_e}) \tag{2.27}$$

$$\mathbf{B} = diag(\mathbf{I}_{nr(n_n+n_p)}\ \mathbf{I}_{nx}\ \mathbf{0}_{n_n+n_p}\ \mathbf{0}_{nx}) \tag{2.28}$$

The solution vector is composed of the variables of the P2D system, $\vec{F}$ consists of all the source terms (non-linear) and $\vec{D}$ takes care of the current boundary condition at the electrode ends. $\mathbf{A}$ is formed of the coefficient matrices and $\mathbf{B}$ has entries one for the variables that have explicit time dependence and zero for the rest. For galerkin FEM with linear elements, $\mathbf{B}$ turns out to be a tridiagonal matrix.

These equations can be discretized in time using time differencing schemes like implicit Euler method (first-order accuracy) or Crank-Nicholson scheme [47] (second-order accuracy). Since these equations are highly non-linear, solution at each timestep needs to be solved iteratively. The most popular choice for dealing with non-linear equations is the newton-raphson method. A simple flow-chart describing the solution algorithm, used in this work, for the P2D system is shown in figure 2.3. This method involves a gauss-seidel approach within the newton-raphson loop, meaning that the guessed solution is updated constantly before solving for the next variable. This kind of sequential solution increases the convergence rate of the newton-raphson method; however, it requires more function calls.

Method-of-lines is recommended for solving this system since adaptive time-stepping

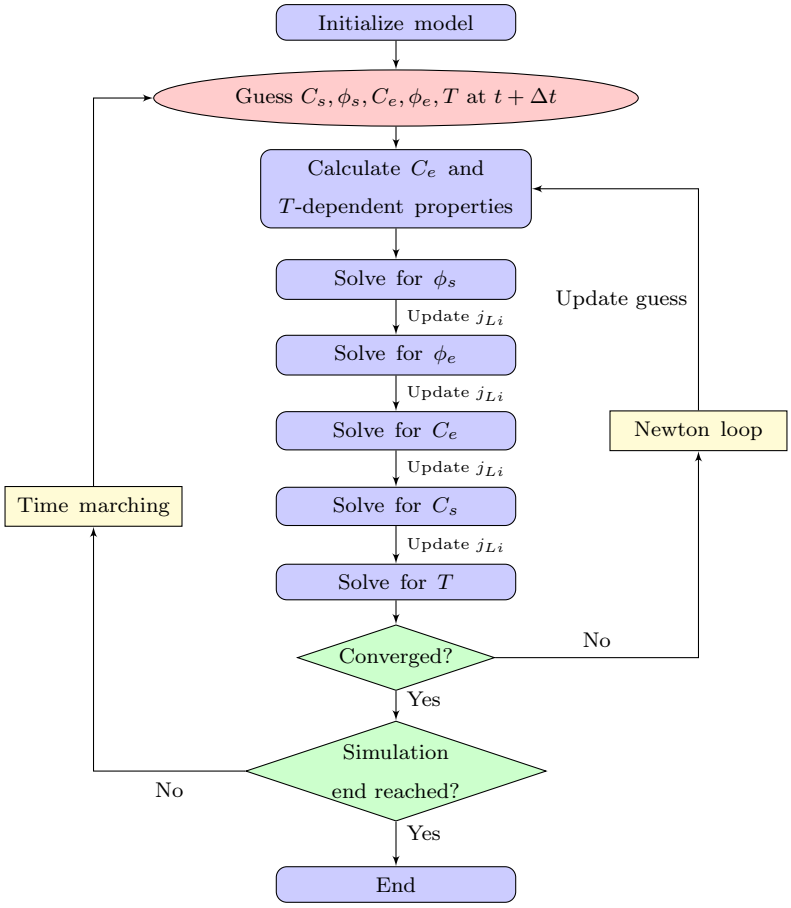

Figure 2.3: P2D Gauss-Seidel solution algorithm

provided by pre-existing ODE solvers reduces simulation time drastically. More information on dealing with such stiff system of equations can be found in the book *Iterative Methods for Linear and Nonlinear Equations* [48].

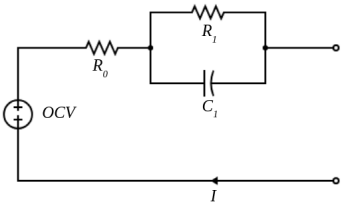

(a) 1^{st} order RC model

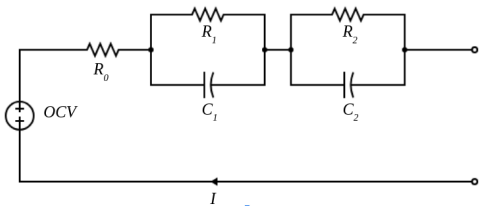

(b) 2^{nd} order RC model

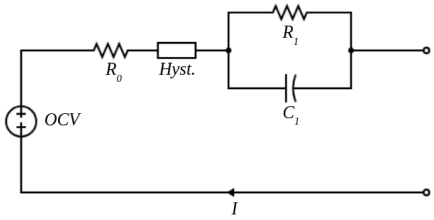

(c) 1^{st} order RC model with hysteresis

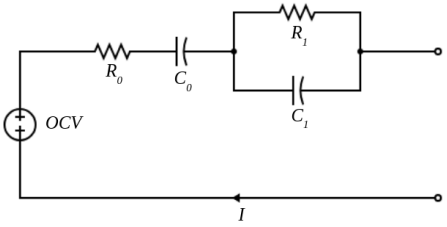

(d) PNGV model

Figure 2.4: Various circuit models

2.2 Circuit Models

The models described in the previous subsections capture the physics behind battery functioning, however, they're computationally expensive and memory-heavy. From a BMS perspective, it is impractical to deploy PDE-based electrochemical models for real-time battery management. Thus, it is imperative to have a quick model with little memory usage that is accurate to a certain degree. Equivalent circuit models (ECM) seem to be an excellent fit for this application [49]. They can simulate a battery faster than real-time and require fewer parameters for operation.

Several circuit models have been analyzed, like the internal resistance model, Thevenin circuit, n^{th} order RC circuit, and PNGV model, for EV applications [50, 51]. Its applicability in energy storage systems was first observed by Randles [52]. Some studies have included the hysteresis effect by adding certain elements to the RC circuits [53]. Each element in ECMs represents a constituent process of the thermo-electrochemical dynamics of the battery. Using the nomenclature shown in figure 2.4, R_0 models the total internal resistance of the battery which captures the combined resistive properties of the electrodes, electrolyte, and current collectors. Notations R_0 and R_{int} are used interchangeably in this work. It can be modified

Model	**Output Voltage** V_{out}	**Notes**
1-RC model	$U - IR_0 - IR_1(1 - e^{-\frac{t}{\tau_1}})$	Time constant, $\tau = RC$
n-RC model	$U - IR_0 - \Sigma_{i=1}^{n} IR_i(1 - e^{-\frac{t}{\tau_i}})$	Multiple RC branches provide higher accuracy
PNGV model	$U - IR_0 - It/C_0 - IR_1(1 - e^{-\frac{t}{\tau_1}}$	C_0 tracks the gradual change in voltage with buildup of current
1-RCH model	$U + sgn(I)M(1 - e^{-\lvert k_p I \rvert}) - IR_0 - IR_1(1 - e^{-\frac{t}{\tau_1}})$	M is the maximum hysterisis voltage and k_p is the decay constant

Table 2.1: Output voltage expressions of different ECMs (Constant current assumed)

to track degradation as well. The RC groups represent various transient processes that occur during battery operation. Processes like charge transfer across electrode-electrolyte interface, li-ion diffusion, li-ion migration make up the transient regime of battery response to input current/voltage. Increasing the number of RC components increases the accuracy of the model at the expense of additional computational complexity. An EMC with too many parameters also runs the risk of overfitting which can lead to unexpected errors. The SOC circuit shown in figure 2.5 models the SOC increase/decrease, depending on the current direction. C_c represents the capacity of the cell. This helps with accurate OCV (U) estimation for the output voltage calculation.

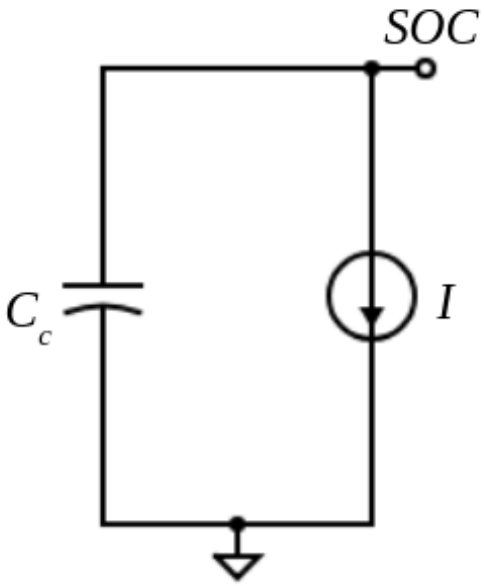

Figure 2.5: SOC circuit

2.2.1 Dual Polarization Model (2-RC Circuit)

As shown by He [54], the Dual Polarization (DP) model is a robust model and strikes the right balance between accuracy, computational efforts, and memory storage. The name Dual Polarization comes from the two polarization processes characterized by the 2 RC branches. One RC branch represents electrochemical polarization, which captures the time response of the charge-transfer process. The second RC branch represents concentration polarization, which encapsulates the effect of diffusion of lithium ions across the LIB.

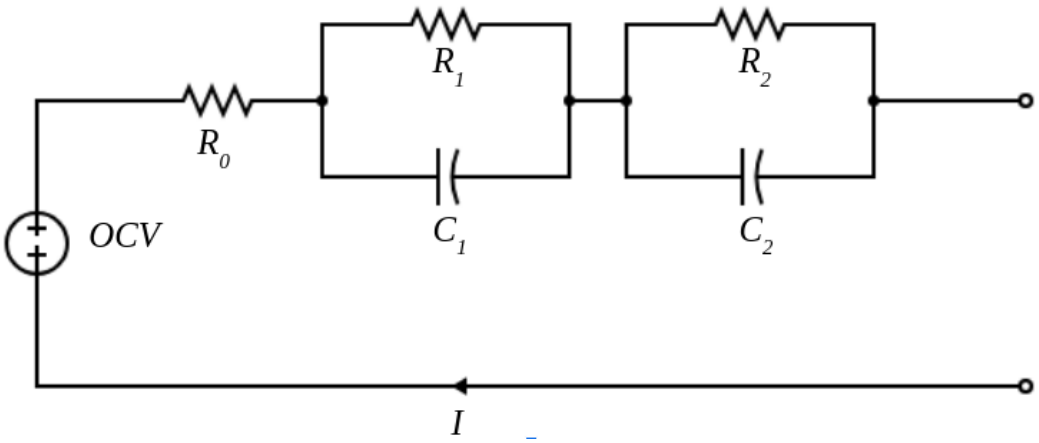

Figure 2.6: DP Model

Figure 2.6 gives an expanded view of the DP model. It consists of 4 parts: open-circuit voltage (OCV) circuitry which is a function of SOC and temperature, internal resistance R_0, and two RC branches. I is the current flowing through the LIB model. Mathematically, the circuit can be defined using the following equations.

$$V_{out} = U - IR_0 - V_1 - V_2 \tag{2.29}$$

$$\frac{dV_1}{dt} = -\frac{V_1}{R_1C_1} + \frac{I}{C_1} \tag{2.30}$$

$$\frac{dV_2}{dt} = -\frac{V_2}{R_2C_2} + \frac{I}{C_2} \tag{2.31}$$

For constant current I, the given set of equations can be solved analytically to yield,

$$V_{out} = U - IR_0 - IR_1(1 - e^{-\frac{t}{\tau_1}}) - IR_2(1 - e^{-\frac{t}{\tau_2}}) \tag{2.32}$$

where τ_1 and τ_2 represent the time constants ($\tau = RC$) of respective RC components. The solution is obtained based on the assumption that the potentials across the two RC branches are 0 initially. Since the aim of this thesis is to model various LIB operating scenarios using a simple, quick, and accurate model with a low memory occupancy, the DP model is chosen.

In total, there are 4 ODEs and one algebraic equation for SOC, voltage, and tem-

perature evaluation. Together, they can be written as,

$$\frac{d(SOC)}{dt} = -\frac{I}{C_c}$$

$$\frac{dV_1}{dt} = -\frac{V_1}{R_1 C_1} + \frac{I}{C_1}$$

$$\frac{dV_2}{dt} = -\frac{V_2}{R_2 C_2} + \frac{I}{C_2}$$

$$\begin{aligned} mc_p \frac{dT}{dt} &= I(U - V) - IT\frac{dU}{dT} \\ &\quad - hA_{cell}(T - T_\infty) - \epsilon\sigma_{SB}A_{cell}(T^4 - T_\infty^4) \end{aligned}$$

$$V_{out} = U - IR_0 - V_1 - V_2$$

It should be noted that all the main circuit parameters, namely, R_0, R_1, R_2, C_1 and C_2 are dependent on SOC and temperature. The aforementioned equations are discretized in time to solve for varying current profiles. The python package `scipy.integrate.odeint` is used for the analysis of the ECM in this thesis.

3 P2D Model - Validation and Results

As established in the previous section, the physics-based models are superior when it comes to accuracy. Thus, based on the methodologies discussed in the previous chapter, FVM and FEM codes are constructed and validated against existing literature. A few results related to LIB temperature response and some modeling roadblocks are discussed.

3.1 Model Comparisons

Three cases are considered for the validation of the in-house code. The code is written in python, which is a high-level language. It is used to ensure ease of code readability and management. The combination of FVM and backward Euler time discretization of the LIB governing equations (electrochemical-thermal) reduces to a matrix equation $\mathbf{A}\vec{u} = \vec{b}$, where the coefficient matrix ($\mathbf{A}$) turns out to be tridiagonal. Thus, to take advantage of the tridiagonal form of $\mathbf{A}$, `scipy.linalg.band` python package is used for quickly solving the matrix equation.

3.1.1 Case 1

For the validation of the FVM code, the results from Mazumder and Lu [22] are considered. Their study aimed to perform a real-time simulation using the full-scale P2D model. Leveraging techniques like source term linearization and efficient tridiagonal matrix solution, they were able to simulate a 15-minute current profile in less than 12 seconds. They chose Fortran90 to simulate the FVM-based LIB operation.

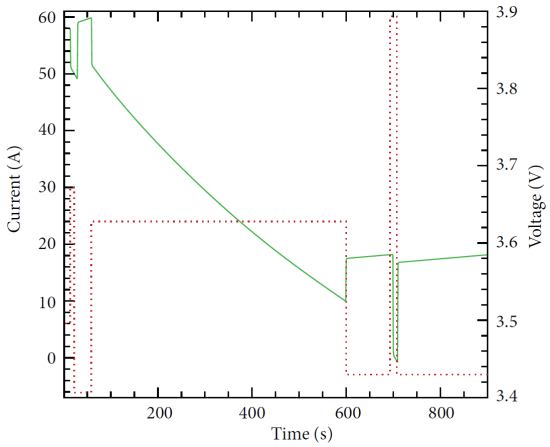

(a) Voltage - Mazumder and Lu

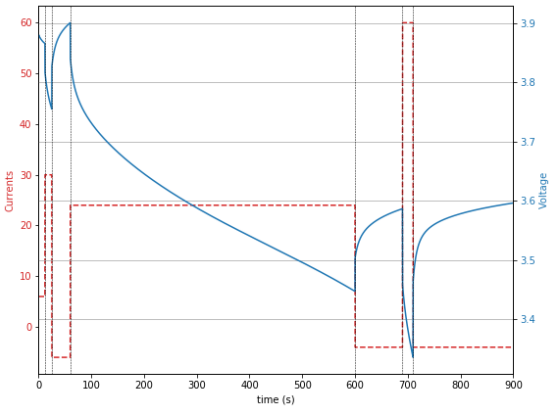

(b) Voltage - In-house code

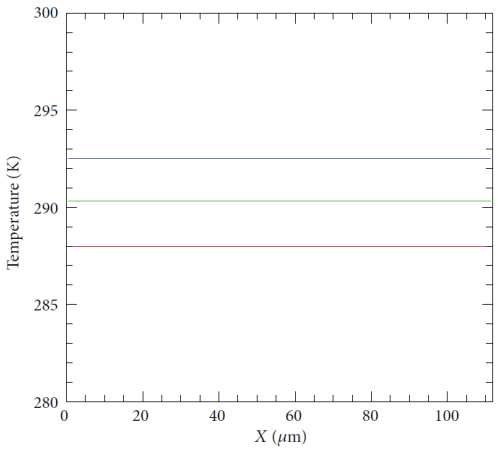

(c) Temperature - Mazumder and Lu

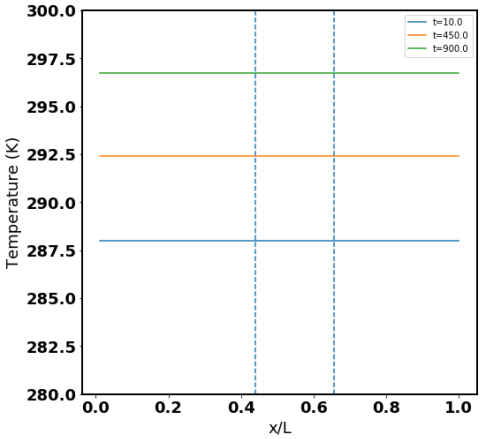

(d) Temperature - In-house code

Figure 3.1: Case 1

Analysis

Just qualitatively, the differences between both the simulations are clear from figure 3.1. The voltage simulated by both the codes depict contrasting time constants, despite of the same parameter inputs. Whenever the direction of the current changes, a smoother transition is observed in the in-house code output. A smooth response means that the charge diffusion process, that takes places at short time scales, is slow. The temperature profile also shows dissimilarities. The difference in computation time can be seen in figure 3.3.

These differences can be attributed to a multitude of reasons. Firstly, the current profile used for the in-house simulation was obtained through qualitative mapping

of the current profile used in the paper. Secondly, the thermal boundary conditions were not clearly specified. Thirdly, Mazumder and Lu used a time step of 1 second, whereas the in-house code ran with a smaller time step of 0.1 second. This also explains the huge difference in computation time of both the codes. Another reason for this stark difference in computation time is the choice of coding language. Fortran is miles ahead of python (`scipy` in this case) in terms of scientific computing speed.

Code	**Computation time (s)**
Mazumder and Lu	12
In-house	502.21

Table 3.1: Model speed comparison

To conclude, the in-house code doesn't completely mimic the paper results; however, the fact that it converges to a result that is close to the published work, is the first step towards validation.

3.1.2 Case 2

To further validate the in-house code, the results from Smith et al [55] are used. They develop a low order dynamic battery model to accurately predict non-linear P2D battery model results. The nonlinearities associated with the P2D model are approximated on a distributed basis.

Analysis

For this case, a FEM formulation of the full-scale P2D model is also developed in FEniCS [56]. The results from the paper, FVM and FEM are compared in figures 3.2, 3.3, and 3.4.

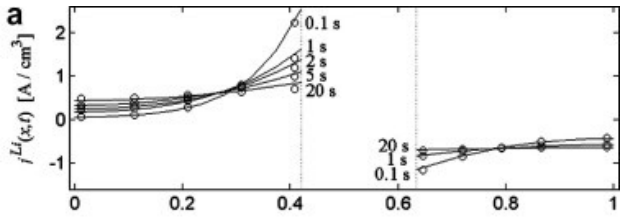

(a) Smith et al

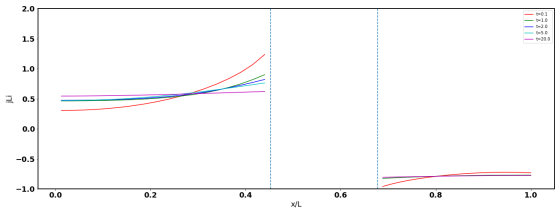

(b) In-house - FVM

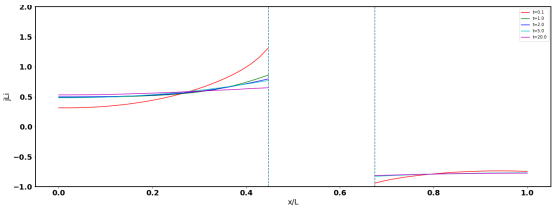

(c) In-house - FEM

Figure 3.2: Case 2 - Rate of reaction

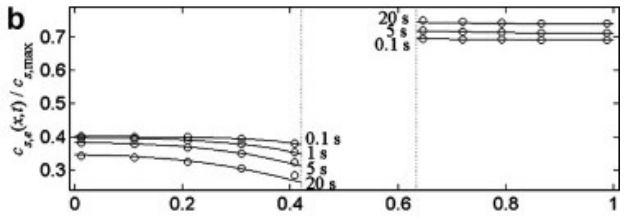

(a) Smith et al

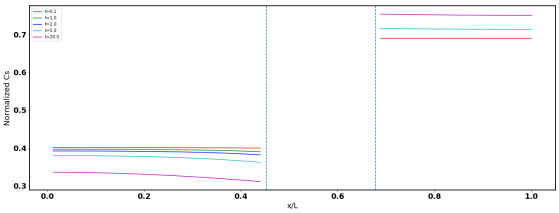

(b) In-house - FVM

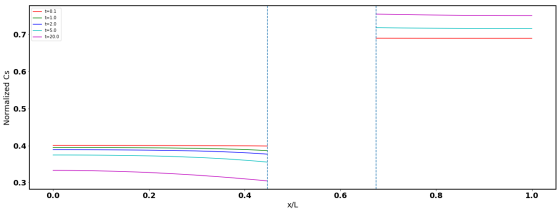

(c) In-house - FEM

Figure 3.3: Case 2 - Normalized solid concentration

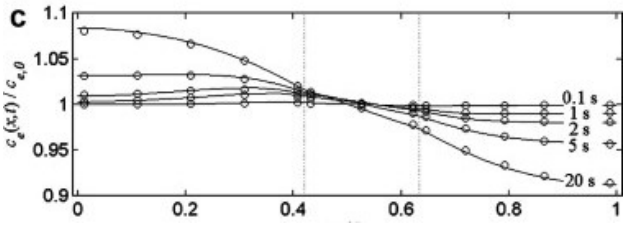

(a) Smith et al

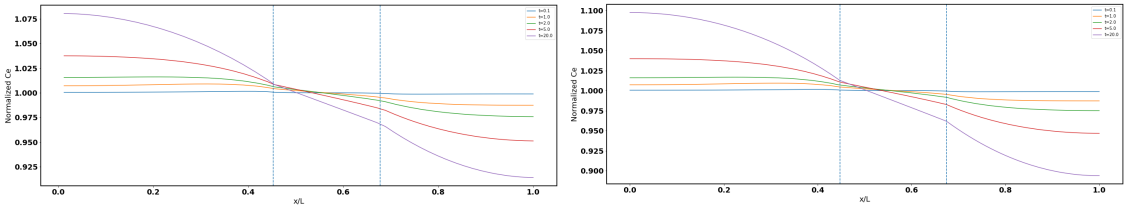

(b) In-house - FVM

(c) In-house - FEM

Figure 3.4: Case 2 - Normalized electrolyte concentration

The figures show the rate of reaction, electrolyte concentration, and solid concentration profiles obtained from Smith et al, FVM and FEM. The rate of reaction is hardest to match, given its sensitivity to the overpotential η (exponential dependence). It can be seen that both, FVM and FEM, closely follow the trend observed in Smith et al. The j_{Li} profile near the anode-separator at 0.1-second shows maximum deviation. A visible difference between FVM and FEM predictions is noticed only in the electrolyte concentration profiles, with FVM prediction being closer to the paper result. Overall, both the in-house codes do a good job of matching the profile presented in Smith et al.

The difference in computation time between FVM and FEM schemes is shown in table 3.2. The coupling of the solid concentration in spherical coordinates to the variables varying in x-direction is not efficiently implemented in FEniCS. Based on the breakdown of the computation time, FEniCS spends 34% of the time in extracting the surface concentration from the model spheres and mapping them onto the x-grid. Thus, an efficient implementation or some model reformulation is required to make FEniCS a viable option for P2D simulations.

Model	**Computation time (s)**
FVM	153.37
FEM	306.57

Table 3.2: FVM-FEM comparison

3.1.3 Case 3

The results from Torchio et al [20] are used for the final validation of the in-house FVM model. They developed a robust MATLAB code (LIONSIMBA) with an adaptive time solver to implement the P2D model. To gauge the standing of their FVM implementation, they compared their model's computation time with that of the other established codes like DUALFOIL and COMSOL. Their test runs showed that their code is consistently faster than COMSOL and almost equal in speed to DUALFOIL. They also compared the performance of the P2D model with reformulated models, as shown in figure 3.3. The parabolic approximation starts to diverge from the P2D results when the discharge rate is greater than 5C.

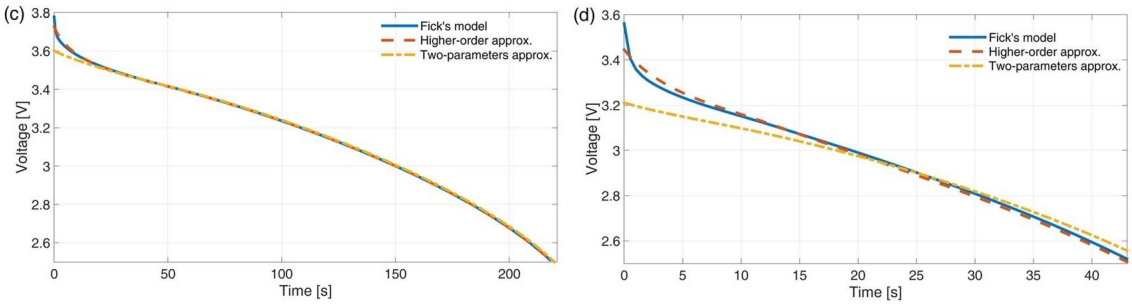

(a) 5C discharge

(b) 10C discharge

Figure 3.5: Comparison of P2D, two-parameter (PP) and high-order model

Analysis

For the given set of parameters, Torchio et al simulated 1C discharge of a LIB using their electrochemical-thermal P2D code for different heat transfer coefficient values. The obtained temperature profiles are compared with the in-house FVM code, as shown in figure 3.6.

The in-house code matches the paper results quite well. The code is now deemed valid and, in the next section, it is used to study the effect of heat transfer coefficient and ambient temperature conditions of a LIB.

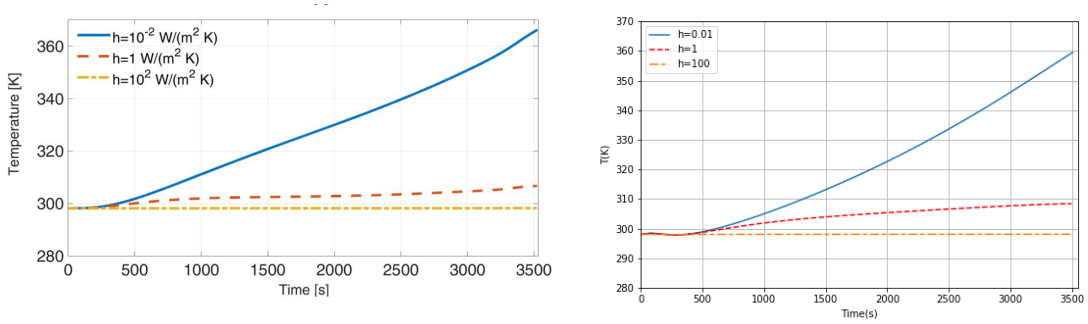

(a) Torchio et al result

(b) In-house FVM result

Figure 3.6: Comparison of temperature profiles

3.2 Results

In this section, the thermal response of LIB is analysed for different discharge rates, heat transfer coefficients, and ambient temperatures.

3.2.1 Effect of Heat Transfer Coefficient

The role of battery management systems is to maintain safe and efficient operating conditions around the battery. The most common mode of heat transfer used by the cooling systems is convection, which is characterized by the heat transfer coefficient h. For this study, the values of h employed are 0, 0.1 and 1 $Wm^{-2}K^{-1}$. The LIB simulated in this work is same as the one used by Torchio et al [20]. The ambient temperature is set to 298 K.

The effect of heat transfer coefficient can be seen in figures 3.7 and 3.8. The voltage curve gets pushed to the right as h decreases. For 1C discharge, the impact of h is modest on the voltage response. The same cannot be said for 5C discharge. The 5C discharge curves for smaller h values are incorrect to begin with. The reason is explained below.

A very interesting inference can be drawn from this behaviour. The LIBs with higher heat transfer coefficient reach the cut-off voltage more quickly. This re-

sponse can be explained by the change in the kinetic and diffusive properties of the LIB components. As the temperature increases, the reaction rates and diffusivities increase, leading to a decrease in the internal resistance (R_{int}) of the LIB. Thus, the voltage drop (IR_{int}) observed at high temperatures is lower than what is seen at higher temperatures. This also means that the irreversible heat generation term (I^2R_{int}) decreases with increase in temperature. However, high temperatures also lead to accelerated capacity fade. Thus, an optimum temperature exists for efficient utilization of the battery.

The 5C-discharge temperature profiles for $h = 0$ and $h = 0.1$ show that the LIB temperature crosses 200°C. This is an inaccurate, though realistic, prediction as the kinetics associated with thermal runaway are not included in the P2D model. The temperature-dependent properties like electrolyte diffusivity and conductivity are formed by fitting a function to a given data set. Since the data set is limited to temperatures less than 60-80°C, the model prediction above this temperature is obtained through extrapolation of these said properties. This may lead to inaccurate predictions at high temperatures. The fact that P2D predicts a voltage response at these temperature is a testament to the above mentioned source of error.

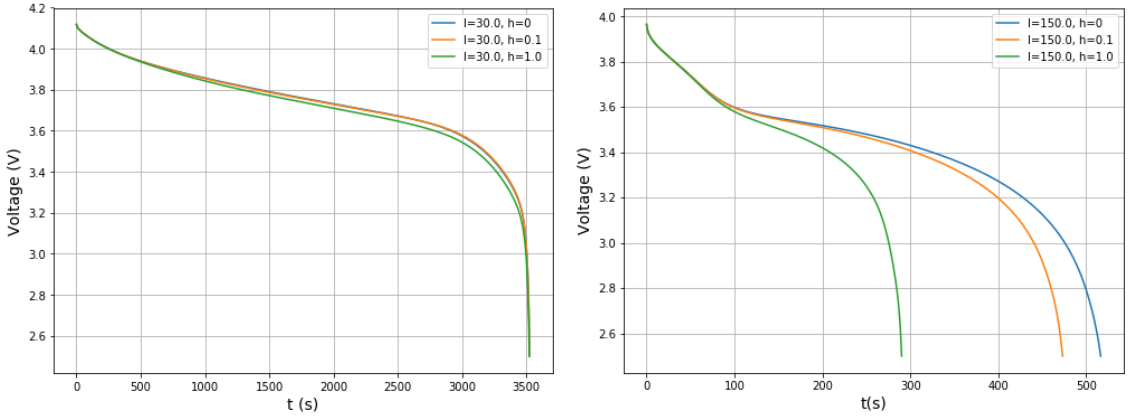

(a) 1C discharge (b) 5C discharge

Figure 3.7: Comparison of voltage response to varying heat transfer coefficients

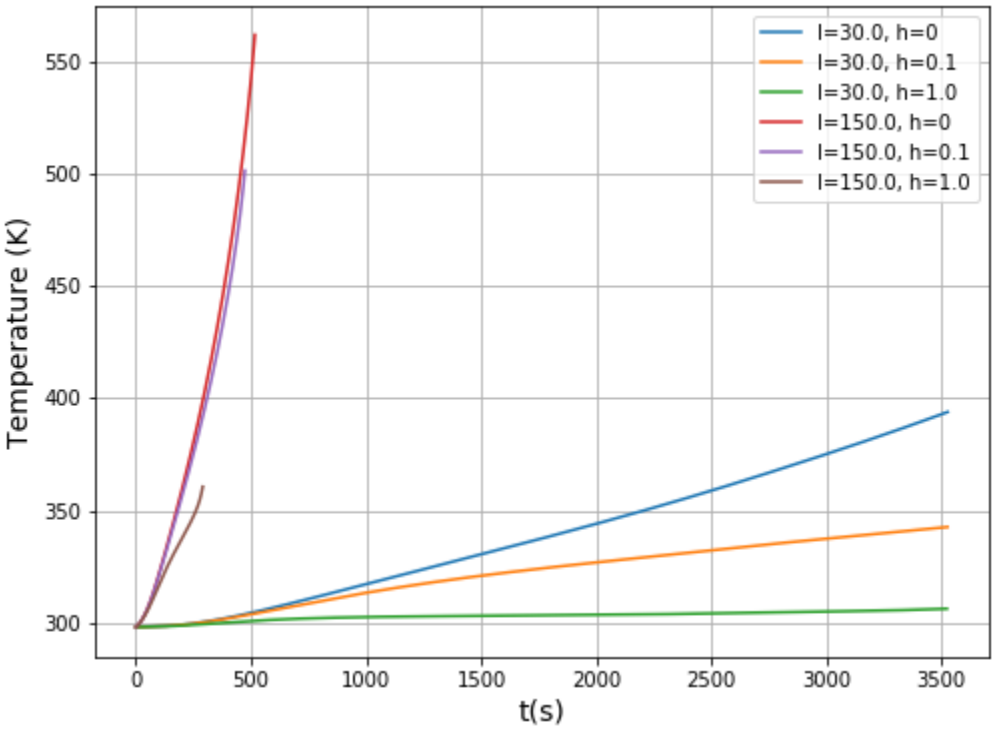

Figure 3.8: Impact of heat transfer coefficient

3.2.2 Effect of Ambient Temperature

The ambient conditions have a substantial impact on the LIB performance. An electric vehicle running in a desert will function differently than when its used to traverse a snowy field. Unless the surrounding temperature of the LIB is maintained using external power, abnormal ambient conditions can significantly affect the LIB life and efficiency.

Figures 3.10 and 3.10 show the battery response to 1C discharge current in different ambient conditions. The heat transfer coefficient is fixed at 0.1 $Wm^{-2}K^{-1}$. Three ambient conditions are considered in this case: 25°C, 60°C, and 120°C.

For times less than 1750 seconds, the voltage drop decreases as the ambient temperature increases. This observation is in alignment with what was explained in the previous case. However, after 1750 seconds, the voltage drop trend flips.

As the SOC of the battery decreases with increasing time, the internal resistance of

the battery achieves a minima when the LIB temperature is between 50-80°C. Based on the temperature plots and assuming a minima in internal resistance exists in the range mentioned before, the LIB placed in 120°C should exhibit lowest voltage drop for times less than 1500 seconds. After which, the temperature of the LIB that is placed in 60°C reaches the said range, thus, a lower voltage drop is observed.

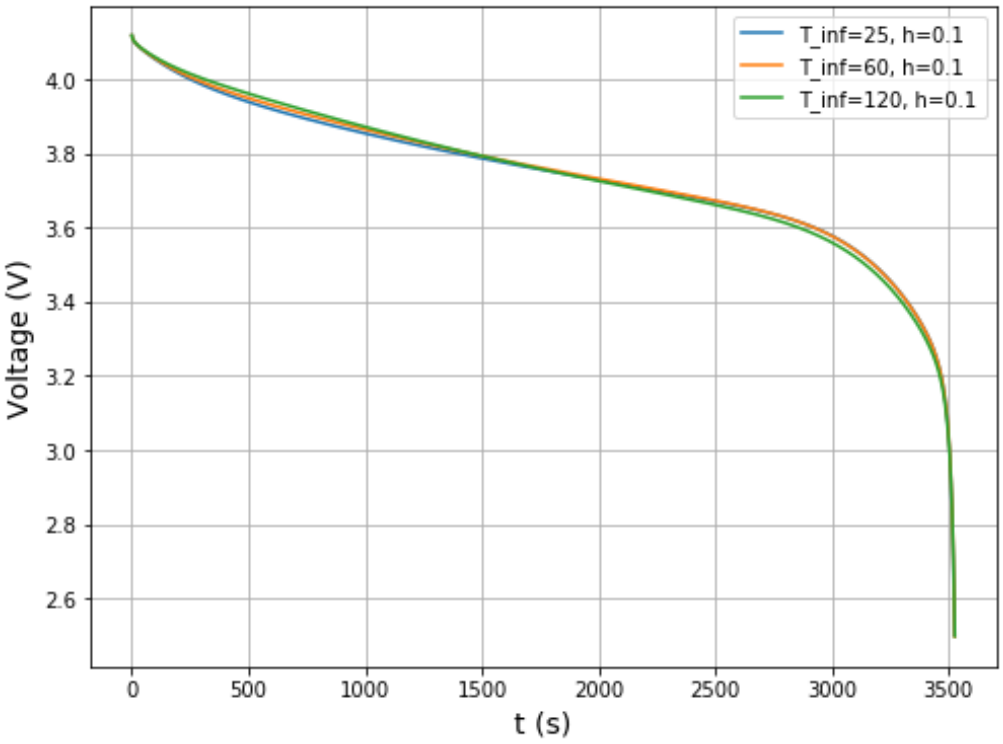

Figure 3.9: LIB voltage response to 1C discharge in different ambient conditions

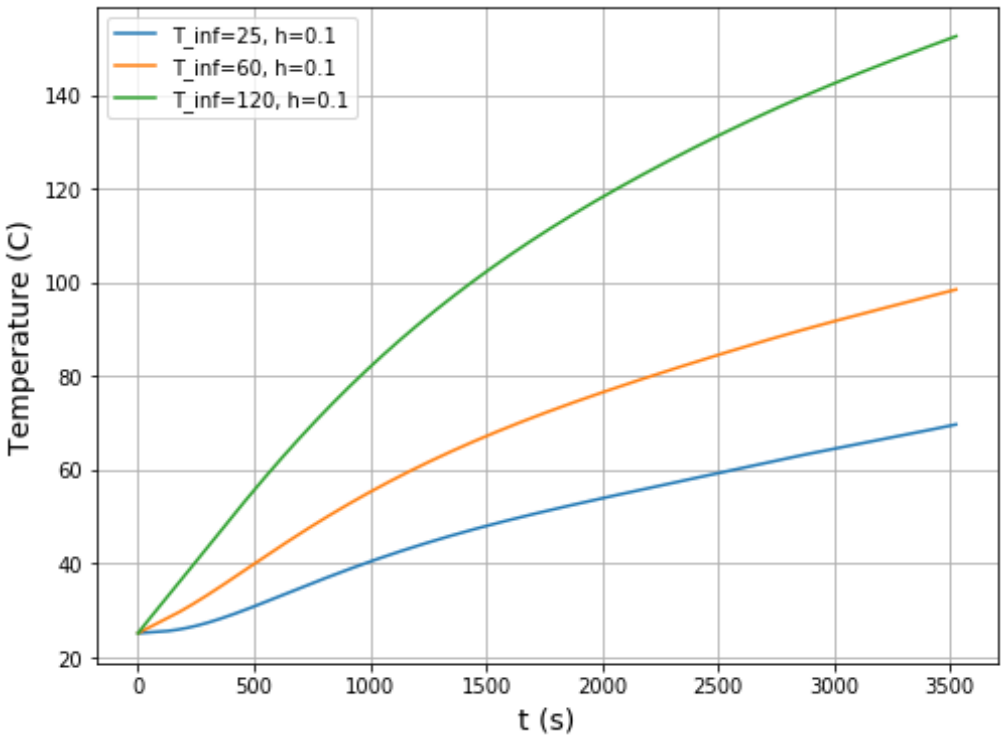

Figure 3.10: LIB temperature response to 1C discharge in different ambient conditions

In conclusion, the thermal management system of the LIB has to be robust enough deal with abrasive working conditions. It should also be able to detect faults that may occur in the cooling system functionality. Improper thermal management can be a damaging ramification to the LIB life and performance.

3.3 Miscellaneous Discussion

In this section, a few tips to increase the efficiency of the code and some issues encountered in practical P2D modeling are presented.

3.3.1 Speeding Up The Code

The amount of time python takes to simulate the LIB operation is way greater than that of the state-of-the-art codes. In an attempt to understand the impact of the choice of coding language on computation time, C++ is employed for comparison.

With the validated model formulation, the python code is replaced with a C++ counterpart. The `armadillo` library [57] is used for efficiently handling the scientific computation involved in the solution of the FVM discretized P2D model.

For the isothermal P2D model, a massive speedup is achieved. For a 1C discharge of a LIB characterized by the parameters given in Torchio et al [20], the performance comparison of python and C++ is shown in table 3.3.

Language	**Computation time (s)**
C++	320.16
Python	3376.52

Table 3.3: Coding language speed comparison

As mentioned before, the computation speed can be drastically increased by optimizing time integration methodology through the use of adaptive time solvers like IDA, SUNDIALS, and DASSL. Figure 3.11 differentiates the regions in a 5C discharge curve based on the number of newton loops required for convergence. The orange zones depict the regions of high nonlinearity. The solver spends more time in these zones, trying to converge to a solution for the given time step. In the yellow zone, the number of newton loops reduces to less than half of that of the orange zones, implying that a bigger time step can be used without overburdening the solver.

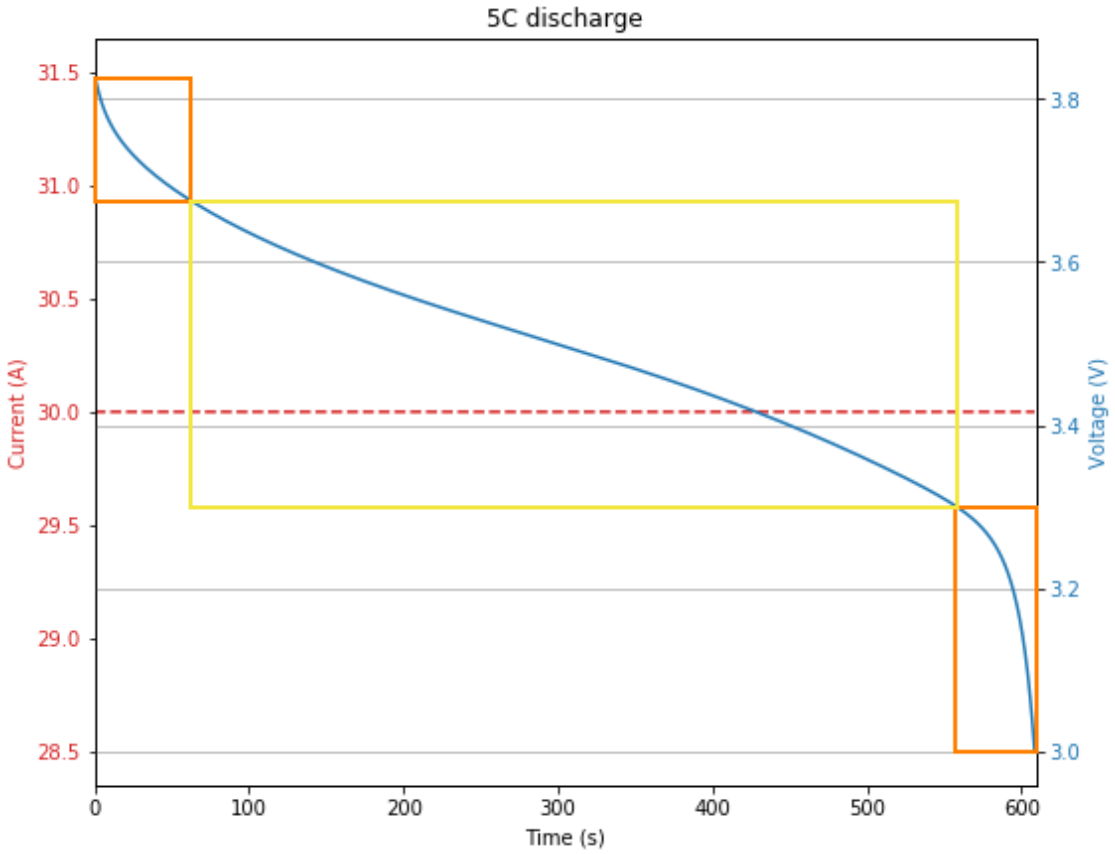

Figure 3.11: Distribution of computation time

3.3.2 Issues

For the abuse conditions examined in this study, the physics-based models suffer from the lack of understanding of the underlying mechanisms and relevant parameters. For example, consider the growth of the SEI layer, which consumes usable lithium and forms a barrier on the anode surface, impeding electrolyte diffusion. If physics associated with such phenomena is not included in the model, the model results become increasingly erroneous as the battery gets cycled. Thus, timely recalibration will be required. Section 1.4 shows the number of processes that characterize the thermal abuse of LIBs. The derivation and the implementation of the physics behind these processes are still not well established.

Since this work attempts to establish a simple pathway for the characterization of LIB abuse, modeling effort is redirected to the ECM representation of the LIB. As compared to the physics-based models, they are easier to build, run, modify,

debug, and maintain. A compromise is made in terms of accuracy when it comes to ECMs. However, from an engineering point of view, if the desired accuracy can be achieved with ECMs, their application makes the most sense. Unlike physics-based models, they require fewer parameters and can be modified based on the operating conditions of the LIB. Also, owing to their simplicity, the online estimation of ECM parameters is widely studied and applied.

4 Equivalent Circuit Model - Parameterization and Validation

Operation of batteries has been extensively and accurately modeled at temperatures ranging from -20°C to 60°C. Thermal abuse models have been developed to understand thermal runaway characteristics. However, little work has been done in bridging the gap between normal operation and abuse conditions. This chapter presents a way of setting up, parameterizing and validating a model that can work for normal operation and high temperature regime.

4.1 Experiment Setup

To set up an Equivalent Circuit Model (ECM) that could simulate battery operation, a series of experiments are conducted to parameterize the model. The Hybrid Pulse Power Characterization (HPPC) test [58] is used for forming the foundation upon which the model will rely on. The HPPC test profile characterizes the battery response to high C-rate discharge and charge pulses. This test works well as it allows one to do both, parameterization and validation of the ECM.

4.1.1 HPPC Test

The HPPC test is composed of two main parts: prepping and cycling. The prepping procedure is done to make sure that the battery cycling begins at 100% SOC. It is a standard constant current-constant voltage (CC-CV) protocol that, first, begins with a discharge at C/2 rate to the discharge cut-off voltage (set by the battery manufacturer), followed by a C/2 charge current till the voltage reaches charge cut-off voltage, and a final constant-voltage charge till the current drops to a threshold

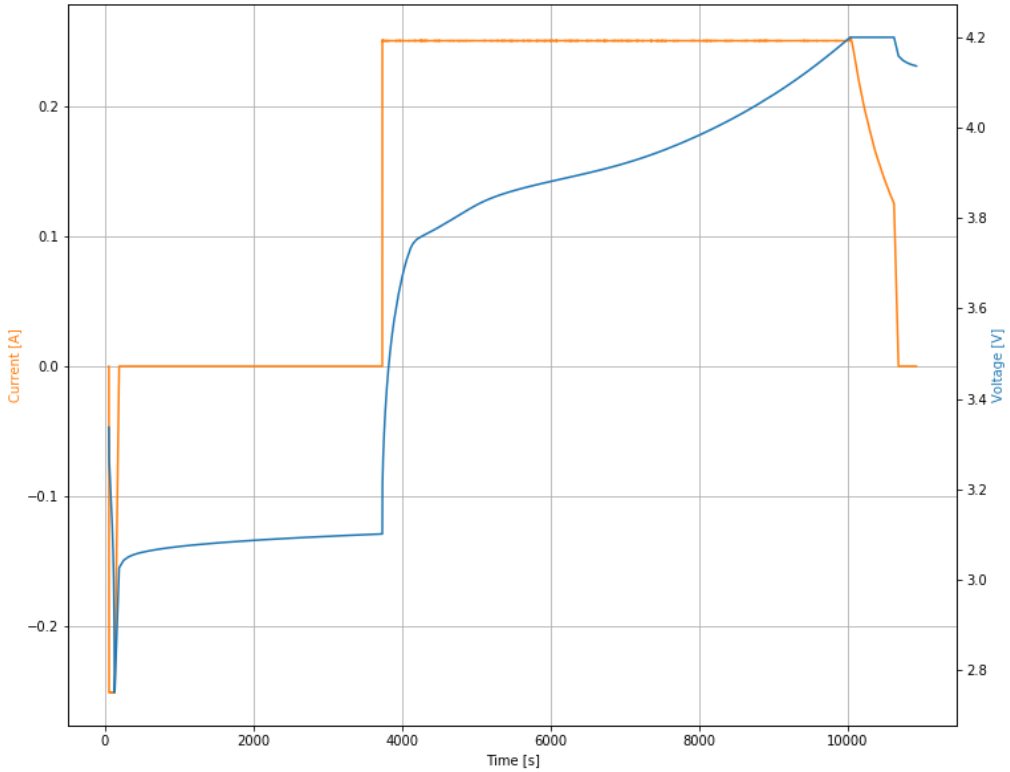

Figure 4.1: HPPC prep profile

value. The battery is allowed to rest for at least 1 hour before beginning the cycling process. This allows the battery to reach an equilibrium at 100% SOC.

The cycling process is made up of successive iterations of a pulse profile. Each pulse profile starts with a 5C discharge pulse that lasts for 10 seconds, followed by a 3-minute rest period, and then a 5C charge pulse of 10-second duration. The current is stopped for 6 minutes after which the SOC of the battery is decreased by 10% by discharging it for 6 minutes at 1C rate. Finally, a 1-hour rest period is set for the battery to reach a steady-state. The full test profile can be seen in figure 4.3.

4.1.2 Battery Specifications

In the tests conducted for the present work, fresh 0.5 Ah Li-ion cells are used. The positive electrode material for these cells is lithium cobalt oxide (LCO) and the negative electrode material is graphite. The cell specifications provided by the manufacturer are given in table 4.1.

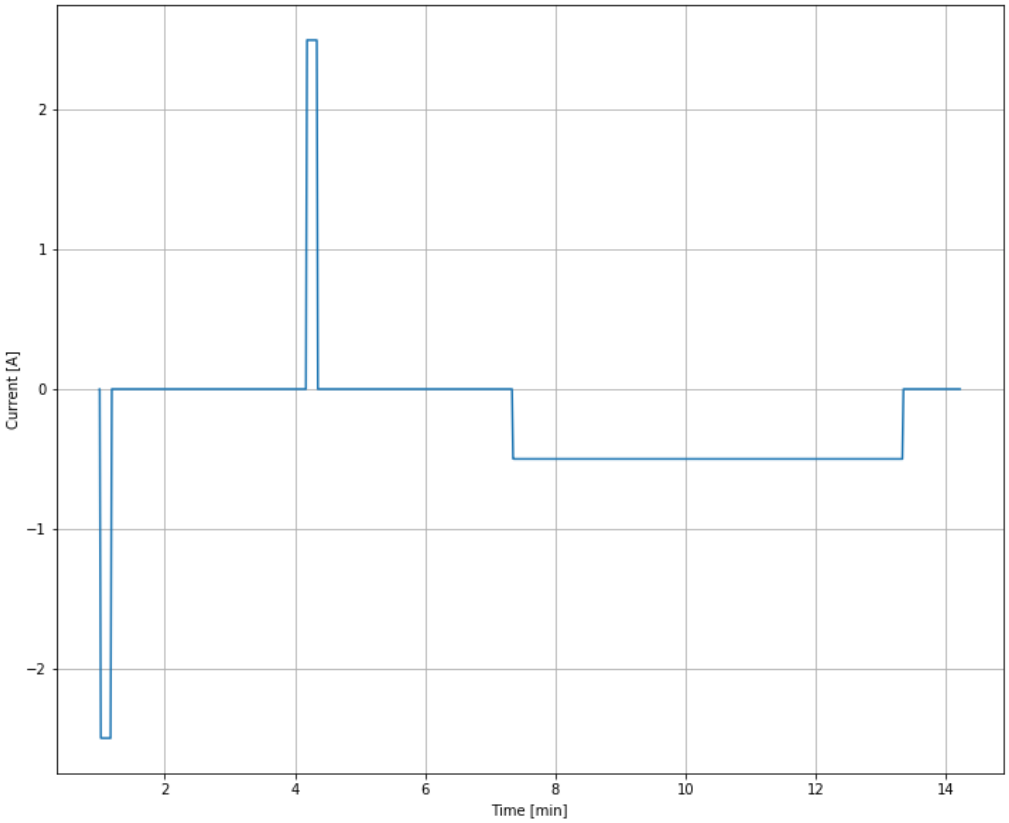

Figure 4.2: HPPC pulse profile

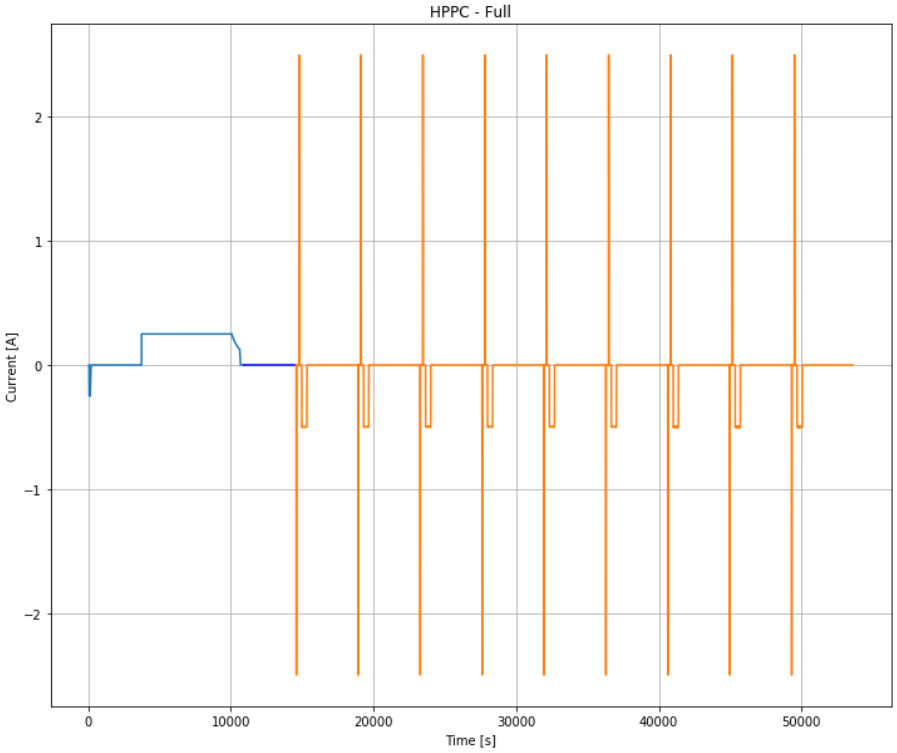

Figure 4.3: Full test profile

Item	Specification
Type	Polymer lithium-ion battery
Model	PL-403144
Cell dimensions	4.3 x 34.5 x 40 mm^3
Nominal Capacity	0.5 Ah
Nominal Voltage	3.7 V
Charge cut-off voltage	4.2 V
Discharge cut-off voltage	2.75 V
Weight	10 g

Table 4.1: Battery specifications

Figure 4.4: Arbin Regulator

4.1.3 Testing Apparatus

The testing system consists of 6 main components: an Arbin LBT21084 to control current/voltage across the cell, MITS Pro software to configure the Arbin instrument and record the current/voltage response of the cell, clamping fixture to hold the cell at a set temperature, GL 840 Graphtec for temperature data acquisition, Omega temperature controller (with a least count of 0.1 °C) and cartridge heaters. All the tests are carried out at standard atmospheric pressure and humidity. The voltage and the surface temperature of LIB are sampled every 1 second for all the tests.

Figure 4.5: Arbin and MITS Pro

Figure 4.6: Omega temperature controller and Graphtec

Figure 4.7: Fixture parts

4.1.4 Fixture Design

To incorporate the temperature dependence of ECM parameters, the HPPC test was conducted isothermally at 22°C, 40°C, 50°C, 60°C, 80°C, 100°C, and 120 °C. An aluminum fixture is designed to obtain near-perfect isothermal conditions at all temperatures considered. The battery is brought to the desired temperature using two cartridge heaters that sit in two slots that are included in the fixture design. When the battery releases heat and overshoots the stipulated temperature, aluminum works particularly well by absorbing the excess heat, quickly conducting it away from the battery, and losing it through convection. To ensure sufficient contact between the battery and the fixture, thermal paste is applied in the tolerance zones.

Note that the prepping part of the HPPC test is carried out at room temperature. The battery is then heated to the required temperature, after which the cycling part commences.

The fixture is composed of two parts. The top part has dimensions 20 x 40 x 60 mm^3, and the bottom part has dimensions 25 x 40 x 60 mm^3. Since a pouch cell, of size 4.3 x 34.5 x 40 mm^3, needs to sit in the isothermal fixture, a box-shaped cavity is added to the bottom part. The cavity is milled to leave a 2 mm tolerance around the battery. Both the parts have cylindrical holes of radius 6 mm, included

for heater placement. Thermal paste is used to maintain contact between LIB and fixture.

4.2 Data Analysis

The HPPC test gives considerable insight into the behaviour of the battery. This section outlines the assumptions, data-fit method, and parameter analysis of the DP model.

4.2.1 Assumptions

Owing to the simplicity of the DP model, a few assumptions and constraints associated with the modeling are specified in this section. The impact of each assumption is examined in subsequent sections.

The HPPC voltage output is used to extract the OCV (represented by U) of the LIB. This process is performed under the assumption that the cell capacity remains constant throughout the test. For temperatures above 60°C, the capacity fade of the LIB should not be neglected for OCV estimation. One significant process that starts near 57°C [38] is SEI decomposition. Thermally, its effect becomes detectable at around 80°C. Additionally, for the lithium-ion polymer cell considered, the PVDF binder can settle on the anode surface or inorganic species can form at the SEI layers at such high temperatures. To understand the influence of all these phenomena on the cell capacity, capacity tests have been carried out before and after the HPPC tests for temperatures greater than 80°C. This helps with the quantification of error in OCV estimation.

Typically, the 5 circuit components that characterize the DP model are assumed to be independent of the SOC of the LIB. Researchers [59] used this assumption in their study of ECMs, while some [60, 61] asserted the relevance of SOC dependence of the circuit parameters . The results, unsurprisingly, show that the SOC dependence of the parameters is indeed present. This study will juxtapose the results obtained

using both these methodologies of modeling.

Since the HPPC test involves steps of 10% discharge, the OCV function extracted from the HPPC test is a discharge OCV function. But, for the sake of simplicity, the OCV obtained from the HPPC test is used for the prediction of cycling tests.

Lastly, as the HPPC test was run only for 6 temperatures, the reversible heat generation term ($\dot{q}_{rev}$, which is proportional to $\frac{dU}{dT}$) may have incurred significant interpolation error. Thus, the prediction test cases are run with and without reversible heat to assess its contribution and range of error.

4.2.2 Parameter Extraction

Two entities need to be identified to parameterize the DP model: OCV and circuit elements. The approach to quantify these parameters is covered below.

4.2.2.1 OCV Fit

This step involves the assignment of equilibrium voltage values, obtained from the HPPC profile, to the SOC values. Figure 4.8 illustrates the occurrence of these equilibrium values in the HPPC output. The first point indicates the 100% SOC mark. As the battery is discharged for 6 minutes after each pulse cycle, the SOC measured at subsequent marks indicates voltage values at SOC levels 10% (approximately) lower than the previous mark.

4.2.2.2 Circuit Element Fit

Several global optimization techniques efficiently fit a model to given data. Particular to ECM parameter determination, methods like Genetic Algorithm(GA), Firefly Algorithm, Particle Swarm Optimization, have been extensively used throughout the literature. In this work, GA is employed for the identification of the parameters of the DP model. Application of GA has several advantages like the ease of

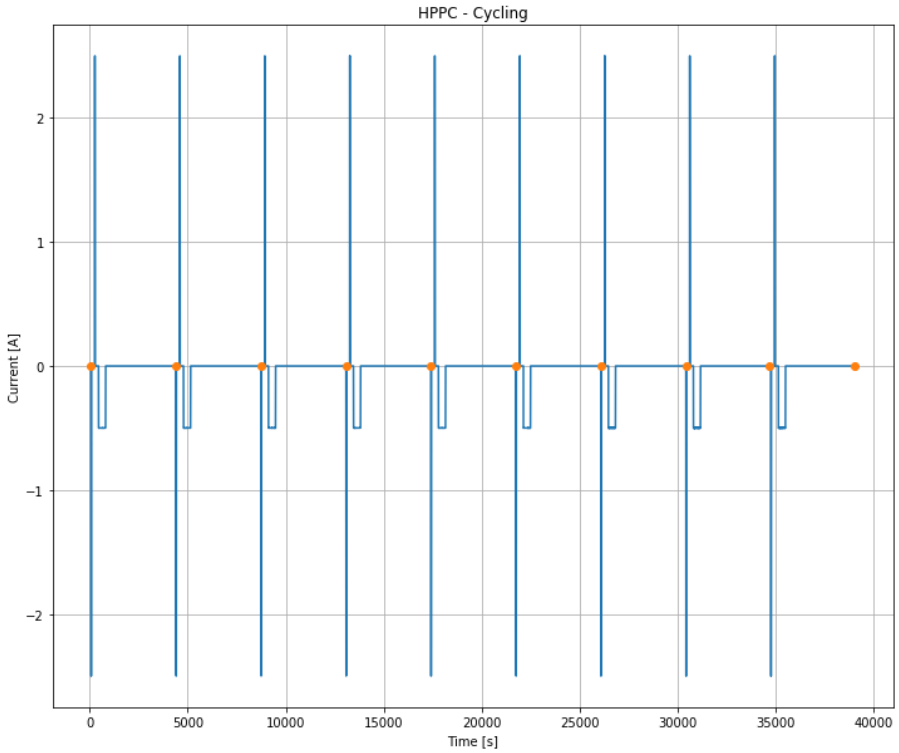

Figure 4.8: Points used for OCV formulation

implementation, flexibility with initial values, use of fitness score instead of derivatives or auxiliary information, and use of an evolutionary approach that precludes convergence problems.

GA mimics the process of natural selection where the fittest individuals breed to give rise to a fitter next generation. GA is made up of 4 phases: fitness score, selection, crossover, and mutation. At each step, the fitness of each individual in the population is evaluated. Fittest individuals are selected for the crossover (reproduction) step. During crossover, offspring is formed by an exchange of random genes between the parents. There is also a small chance of gene mutation in the offspring genome after the crossover process. This ensures diversity in the next generation and prevents premature solutions.

4.3 Model Setup and Validation

Once the methodology has been established, the HPPC test is conducted. The circuit parameters and OCV are characterized, the model's response to high C-rate

Temperature (°C)	Before HPPC (Ah)	After HPPC (Ah)	% change
22	0.466	0.467	0.18
40	0.468	0.467	0.19
50	0.471	0.469	0.35
60	0.472	0.470	0.38
80	0.468	0.465	0.49
100	0.468	0.44	5.87
120	0.475	0.416	12.42

Table 4.2: Capacity of LIB before and after HPPC test

pulses (in HPPC) is studied, and some deviations from the experimental data are addressed.

4.3.1 OCV Results

The capacity values used for the evaluation of OCV-SOC relationship are the ones that are obtained before the test. Table 4.2 shows the capacity values of fresh cells before and after they have been cycled through the HPPC test. For temperatures less than 100°C, the capacity change is relatively negligible. Thus, the OCV obtained for these temperatures can be readily applied. For temperatures higher than 100°C, the cells experience significant degradation. An ageing model is required to compensate and correctly predict cell functioning.

As outlined in section 4.2.2.1, the data is extracted from the HPPC tests conducted at temperatures 22°C, 40°C, 50°C, 80°C, 100°C, and 120°C. Since, the HPPC test for 120°C ended prematurely, only its experimental data and least-square fits are shown. For the remaining temperatures, the data is fit over interpolating splines and different polynomials. Two degrees of interpolation splines are used: linear and cubic, and 6 orders of polynomials are analyzed. The polynomial used for the fits are of the following form,

$$U = \sum_{i=0}^{n} A_i SOC^i \tag{4.1}$$

In the spline fit, the linear fit seems to follow the general trend that is observed in

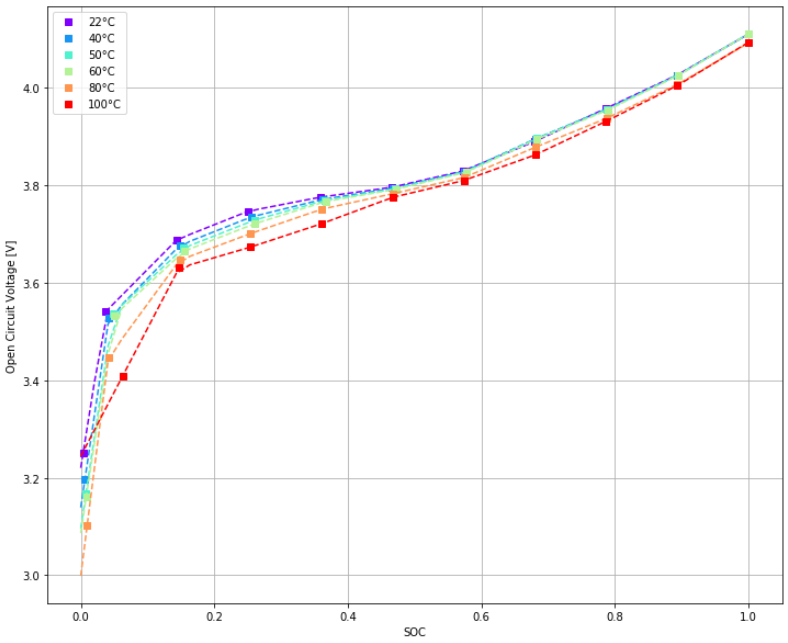

Figure 4.9: Linear spline fit

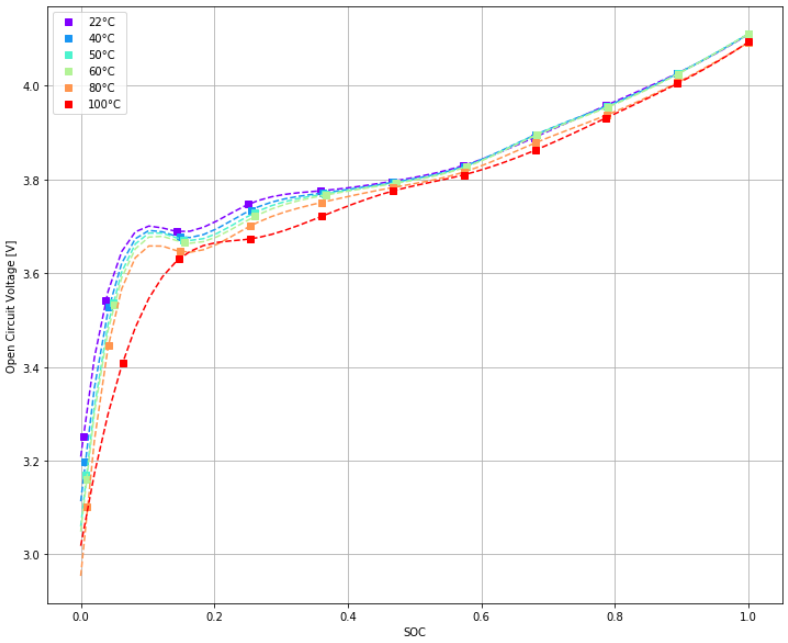

Figure 4.10: Cubic spline fit

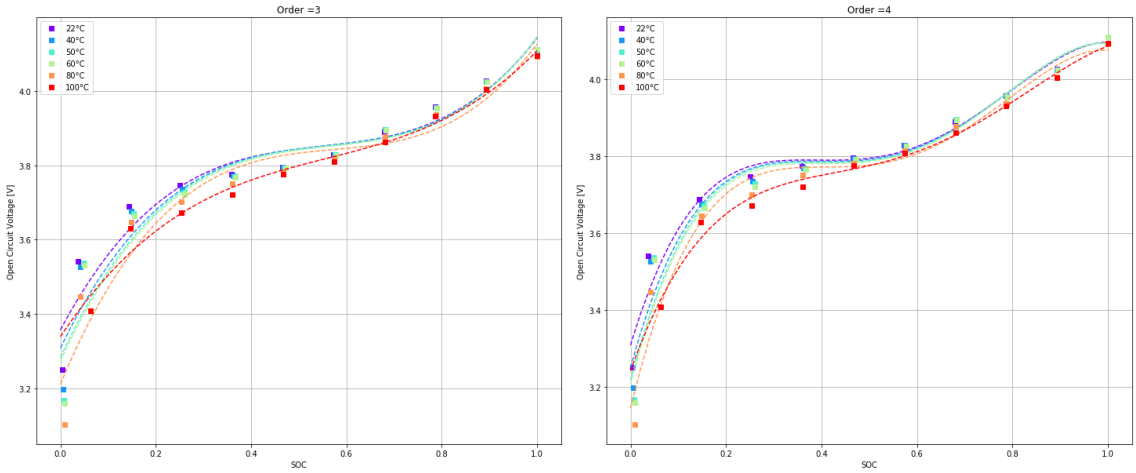

(a) Polynomial of order 3

(b) Polynomial of order 4

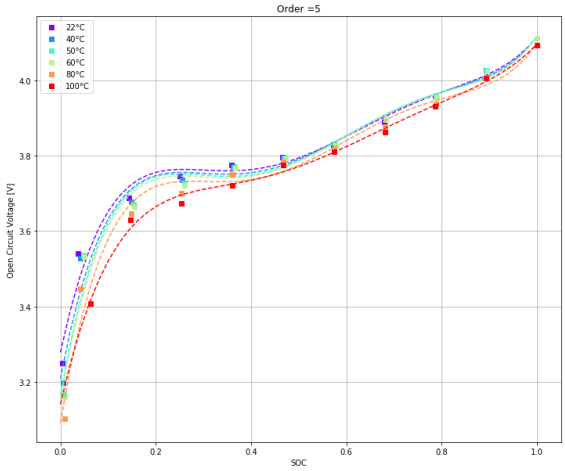

(c) Polynomial of order 5

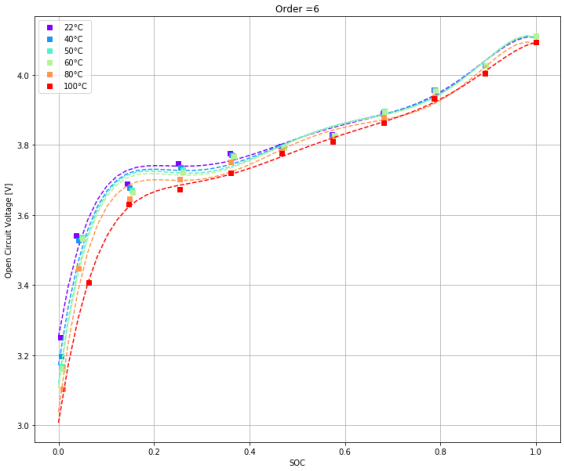

(d) Polynomial of order 6

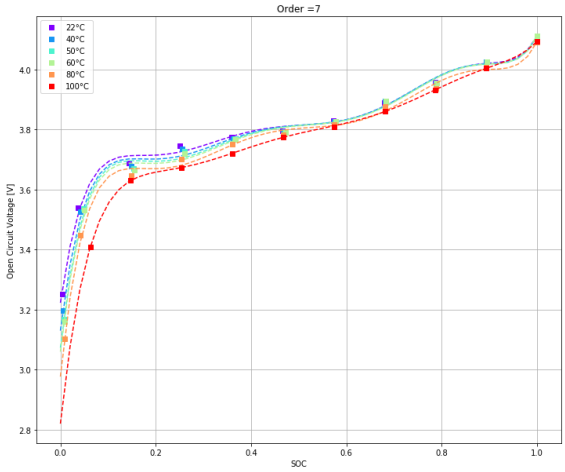

(e) Polynomial of order 7

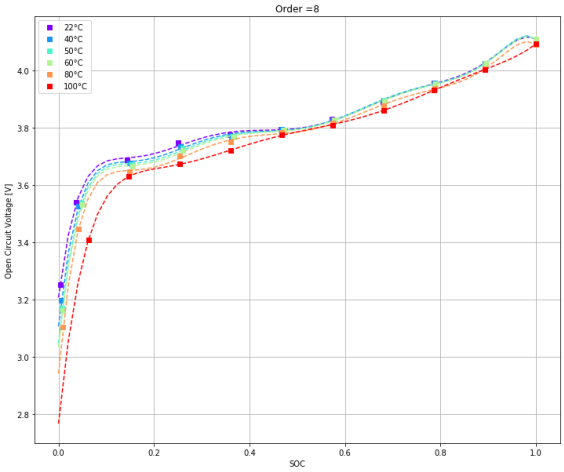

(f) Polynomial of order 8

Figure 4.11: Polynomial fits

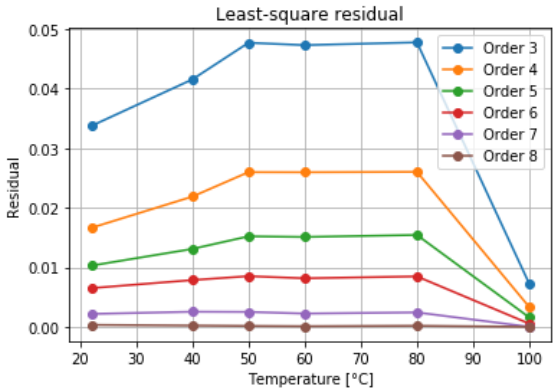

(a) Residual

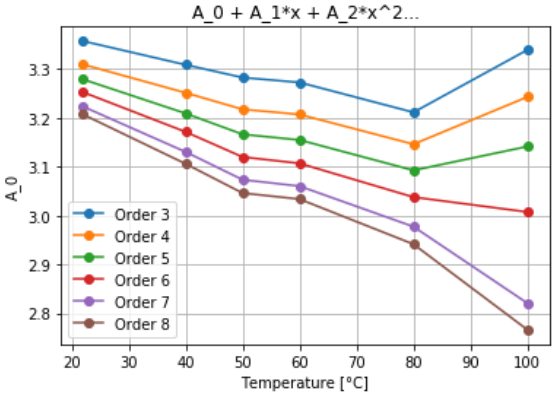

(b) Coefficient A_0

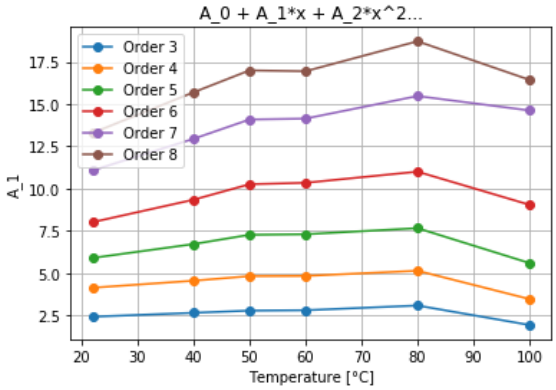

(c) Coefficient A_1

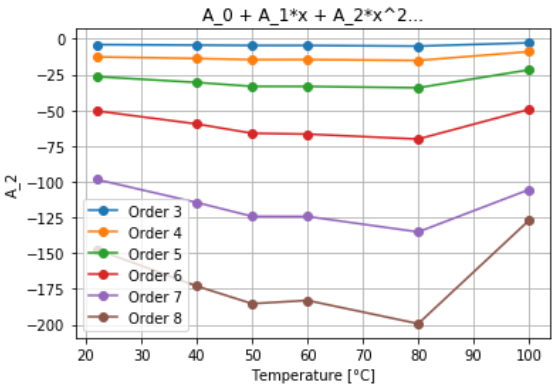

(d) Coefficient A_2

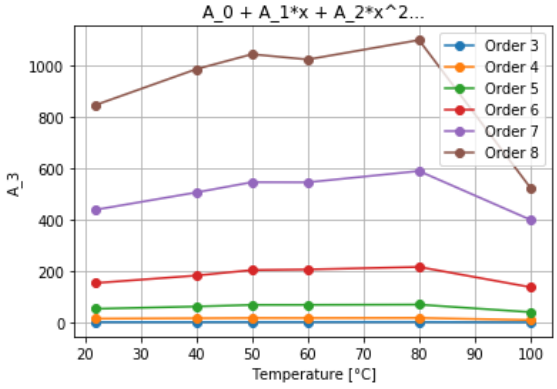

(e) Coefficient A_3

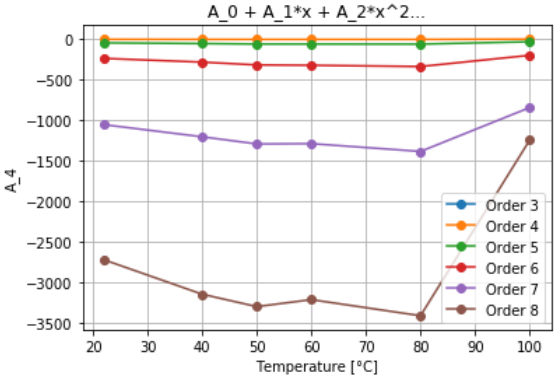

(f) Coefficient A_4

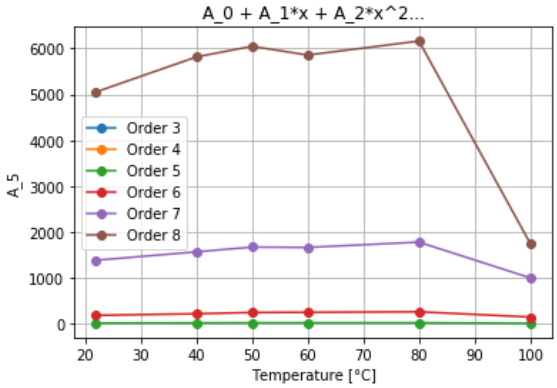

(a) Coefficient A_5

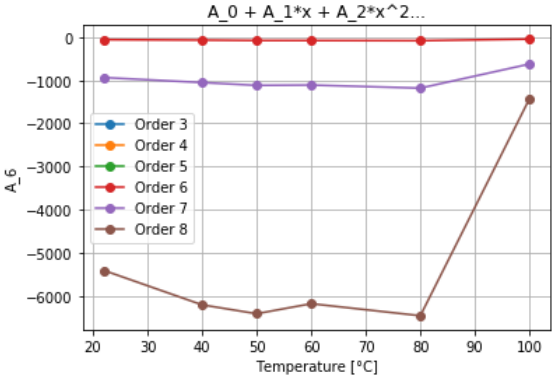

(b) Coefficient A_6

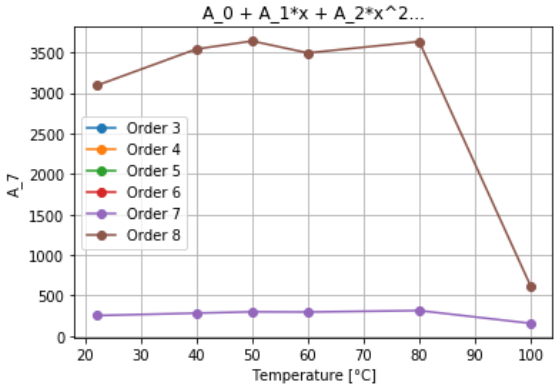

(c) Coefficient A_7

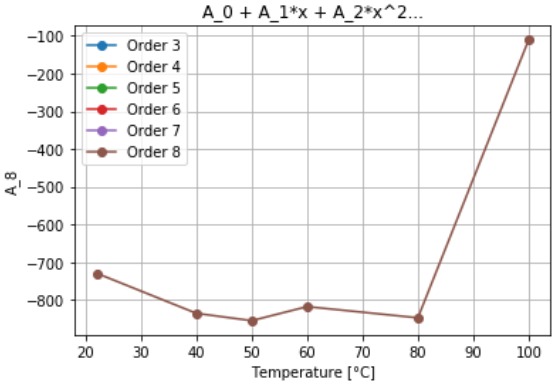

(d) Coefficient A_8

Figure 4.13: Polynomial Coefficients

OCV behavior. The cubic fit looks particularly erroneous near the 10% SOC region. The fit for 100°C is also not matching the OCV trend at 0% SOC. Thus, the need for a different OCV fit is evident. From a BMS point of view, the importance of a model that can track the battery operation with a minimum number of parameters is obvious. This aspect supports the use of polynomials for OCV characterization. Figure 4.11 shows the OCV profile fits with polynomials of varying degrees. As expected, polynomials with higher degrees provide a more accurate fit to the data. However, there can be issues with overfitting. The polynomial of order 8 gives the least residual when compared to the other profiles, thus, it is a good candidate for the formation of the model.

Figure 4.13 consists plots of residuals and polynomial coefficients. Interestingly, a clear monotonic behavior (either increasing or decreasing) is exhibited by each coefficient till 80°C. The reason behind 100°C not following the trend maybe the lack of a data point near 0% SOC. As mentioned before, different reactions like SEI decomposition and regeneration commence at temperatures around 80°C that lead to capacity change which, consequently, may affect the OCV profile.

To choose between high-order polynomial and linear interpolation, the model is run using both fit methods to simulate the HPPC test. The method with the least RMS error is then selected for further analysis.

4.3.2 ECM Parameters Results

After obtaining OCV characteristics of the cells, the ECM parameter values are required to complete the parameterization process. As mentioned in section 4.2.1, parameters will be evaluated for three cases. Starting with the simplest one, a constraint of fixed time constants and SOC independence is considered for parameter evaluation. Adding another dimension, a case with fixed time constants and SOC dependence is studied. Lastly, a case with flexible time constants and SOC dependence is analyzed.

As a reminder, the 5 ECM components of the DP model are R_0, R_1, R_2, C_1 and C_2.

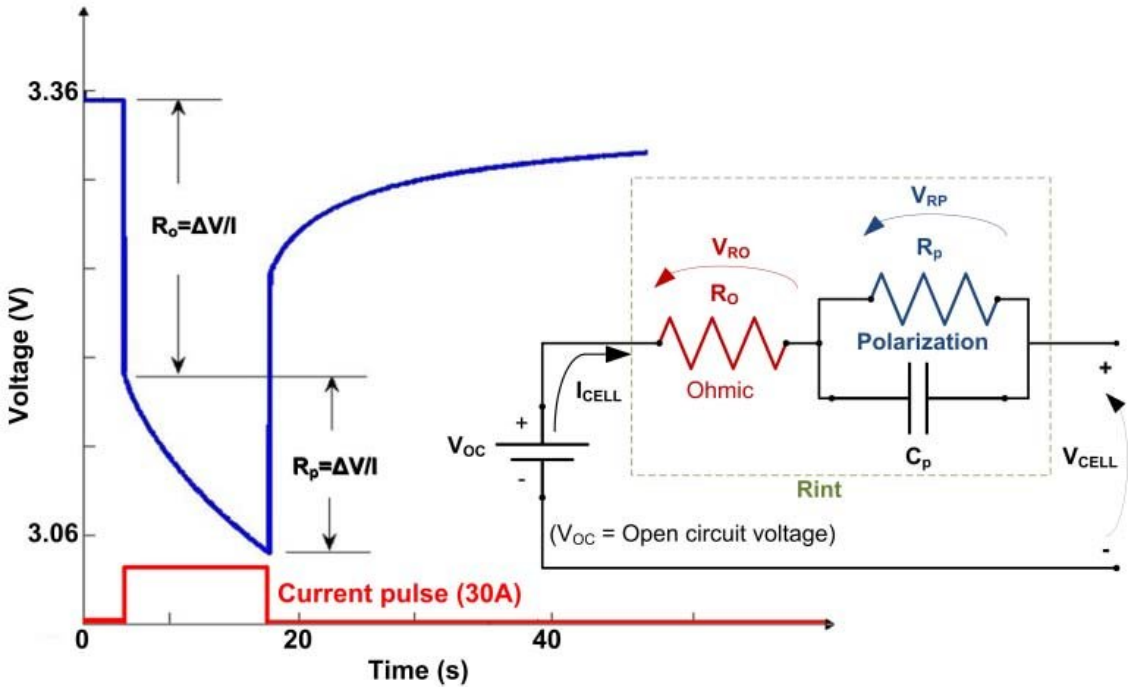

Figure 4.14: Analytical method of internal resistance determination [62]

The genetic algorithm is used to fit these parameters to the HPPC cycling test. Figure 4.2 shows the profile of a single HPPC pulse. The advantage of using the HPPC profile for ECM characterization can be inferred from this figure. The high C-rate pulses help with the assessment of the accuracy of the model. These pulses provide information about internal resistance and time-varying processes that take place inside the LIB. A way to analytically determine the internal resistance is shown in figure 4.14.

The parameters are said to be fit for the model when the least square difference between V_{model} and V_{actual} is minimum. Mathematically, the minimization function is given by,

$$RMS\ Error = \sqrt{\frac{1}{N}\sum_{i=0}^{N}(V_{model} - V_{actual})^2} \tag{4.2}$$

4.3.2.1 Analysis of Experimental Data

The internal resistance of the battery can be directly extracted from the plots in figure 4.15. A common trend can be observed in the R_0 values for a given temper-

ature, it increases when the SOC of the battery is low (less than 20%). Another interesting observation can be discerned from the R_0 and temperature relationship. As temperature increases, the average internal resistance of the cell seems to decrease to a minimum, after which it rises again. The initial decrease in internal resistance can be attributed to the increase in the diffusive and kinetic properties of the cell components. The latter increase can be ascribed to the degradation of the cell itself.

The existence of minima in the internal resistance of a LIB has high application value. For example, fast charging of batteries can be conducted at the point of lowest resistance. This, however, requires increasing the temperature of the LIB which can accelerate the degradation process of the LIB. Even with the reduced charge time at higher temperatures, maintaining the battery at 50-60°C is detrimental to its life. Yet, it is still possible to evaluate an optimal value of temperature at which one can fast charge the LIB without inducing significant capacity fade.

4.3.2.2 Fixed Time Constants and SOC Independence (FTSI)

This method is the most straight-forward way of parameterizing the ECMs. The time constants have fixed values: 20 seconds and 150 seconds. These are calculated by averaging the time constant values obtained from the VTSD case shown in section 4.3.2.4.

Figure 4.15 juxtaposes the experimental data and GA model fit. The model behaves as expected, it roughly averages the internal resistance value for the entire SOC range. The accuracy of time constant values can be inferred by observing the regions where the current is suddenly changing. The battery response is closely imitated by the model's response for all SOC regions except the near-discharge state. If the battery is to be used in a way that it would never go below 20% SOC, then the current model can be used for monitoring the battery operation for temperatures as high as 80°C. However, an ageing component needs to be added to the DP model to extend its prediction capabilities over a longer duration of time.

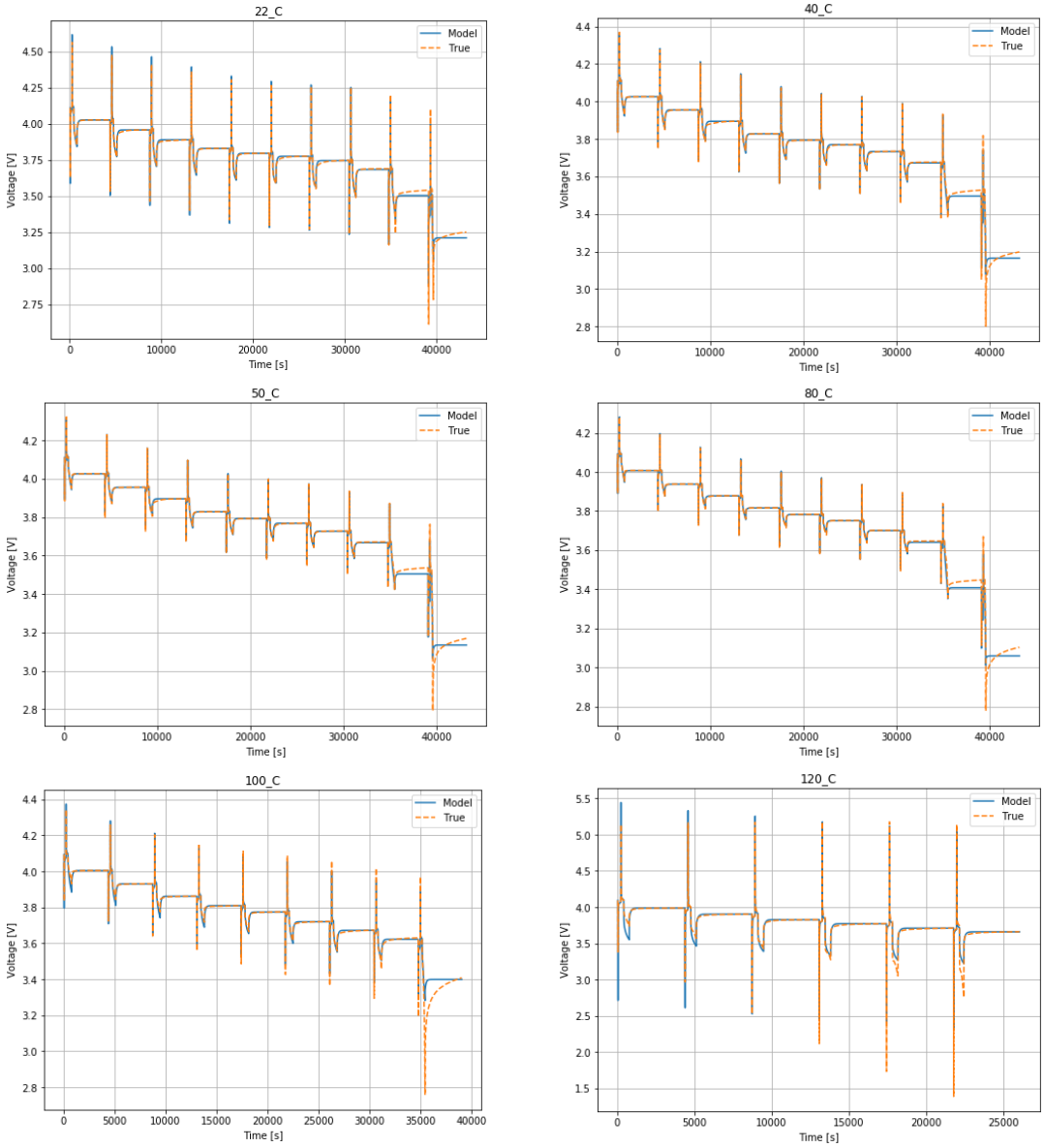

Figure 4.15: Fits with fixed time constants and SOC independence

Temperature (°C)	**RMS Error (V)**
22	0.0148
40	0.0138
50	0.0151
60	0.0154
80	0.0171
100	0.031
120	0.048

Table 4.3: Fixed time constants and SOC independence - RMS error

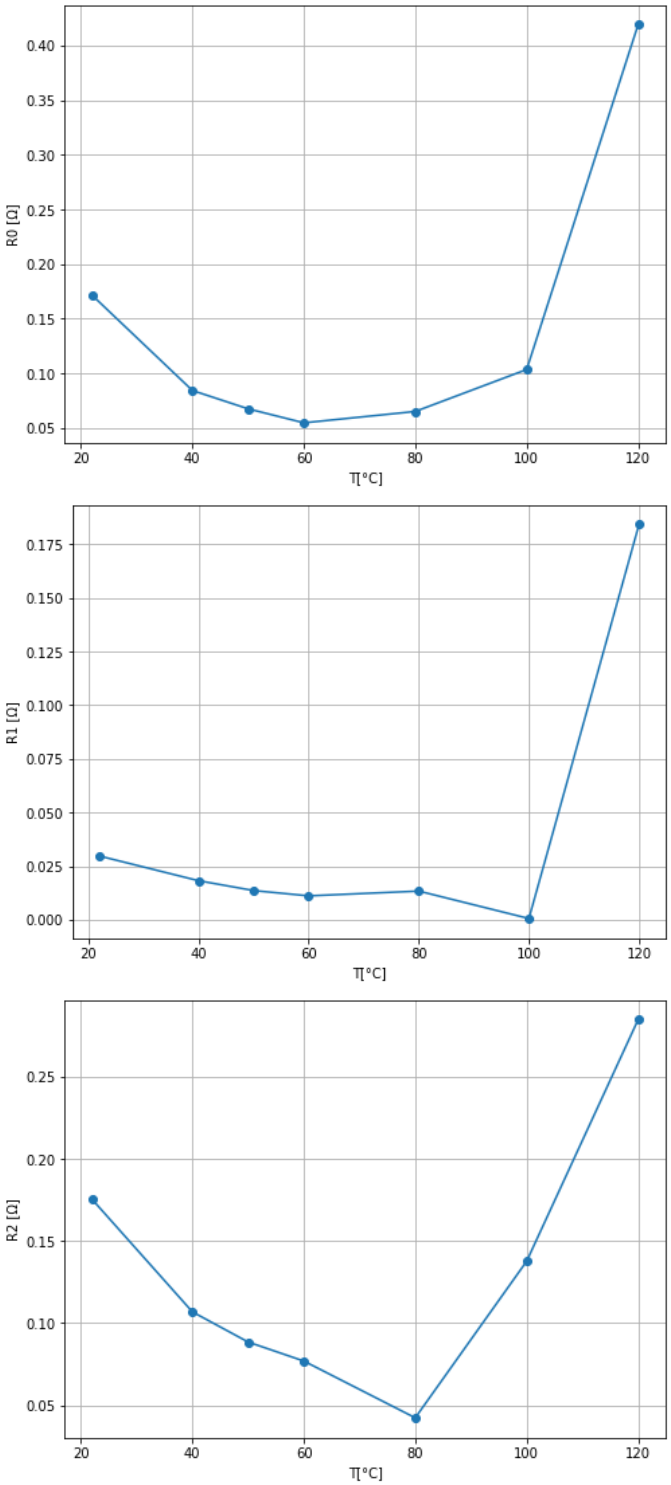

Figure 4.16: Fixed time constants and SOC independence - ECM parameters

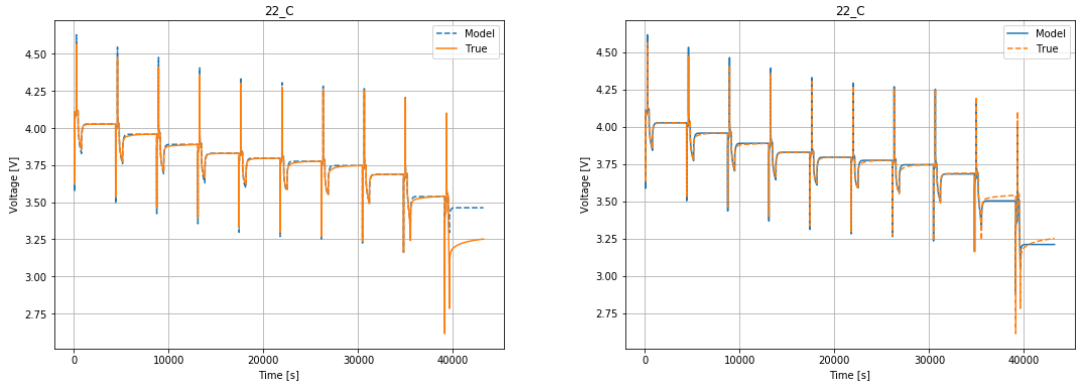

Figure 4.17: Importance of accurate capacity measurement

To highlight the importance of calculating the correct capacity before conducting the OCV and the ECM parameters fit, figure 4.17 shows ECM fit results for 2 cases. The first case uses the capacity given by the manufacturer and the second case uses the value obtained from the capacity test. Both the fits are carried out on 22°C data. Higher accuracy is achieved for data points near the 0% SOC region in the second plot.

4.3.2.3 Fixed Time Constants and SOC Dependence (FTSD)

When SOC dependence is introduced to the model, it is expected to get more accurate. The results corroborate this position. Figure 4.18 shows the data fit results. The SOC region is divided into sections of breadth equal to 10% SOC (approximately). The parameters plotted in figure 4.19 are extracted by fitting each color-coded region shown in figure 4.18.

The advantage of using this approach of fitting is readily evident from the voltage-time plots. Starting with internal resistance, one can observe a common trend over the temperature range of 22-80°C. The internal resistance of the battery increases, almost monotonically, as the SOC decreases. From an application perspective, this trend suggests that the LIBs should be majorly used in the high-medium SOC region to minimize potential drop and power loss (I^2R_{int}). As observed in the previous case, with an increase in temperature, the internal resistance of the LIB decreases to a minimum before rising again. With SOC dependence added to the model, the internal resistance seems to stay constant throughout the SOC range for

temperatures between 40°C and 80°C. At temperatures 22°C and 100°C, the SOC dependence cannot be ignored. Internal resistance variation of ∼25% and ∼44% can be observed for 22°C and 100°C plots respectively.

A common behavior can be discerned from R_1 and R_2 plots . For all temperatures less than 100°C, R_1 decreases as SOC decreases to 75% , suddenly reaches a maximum at around 65% SOC, decreases to a minimum, and increases again. A greater disparity in trends is observed near 0 SOC. R_2 trend looks like the mirror-image of that of R_1.

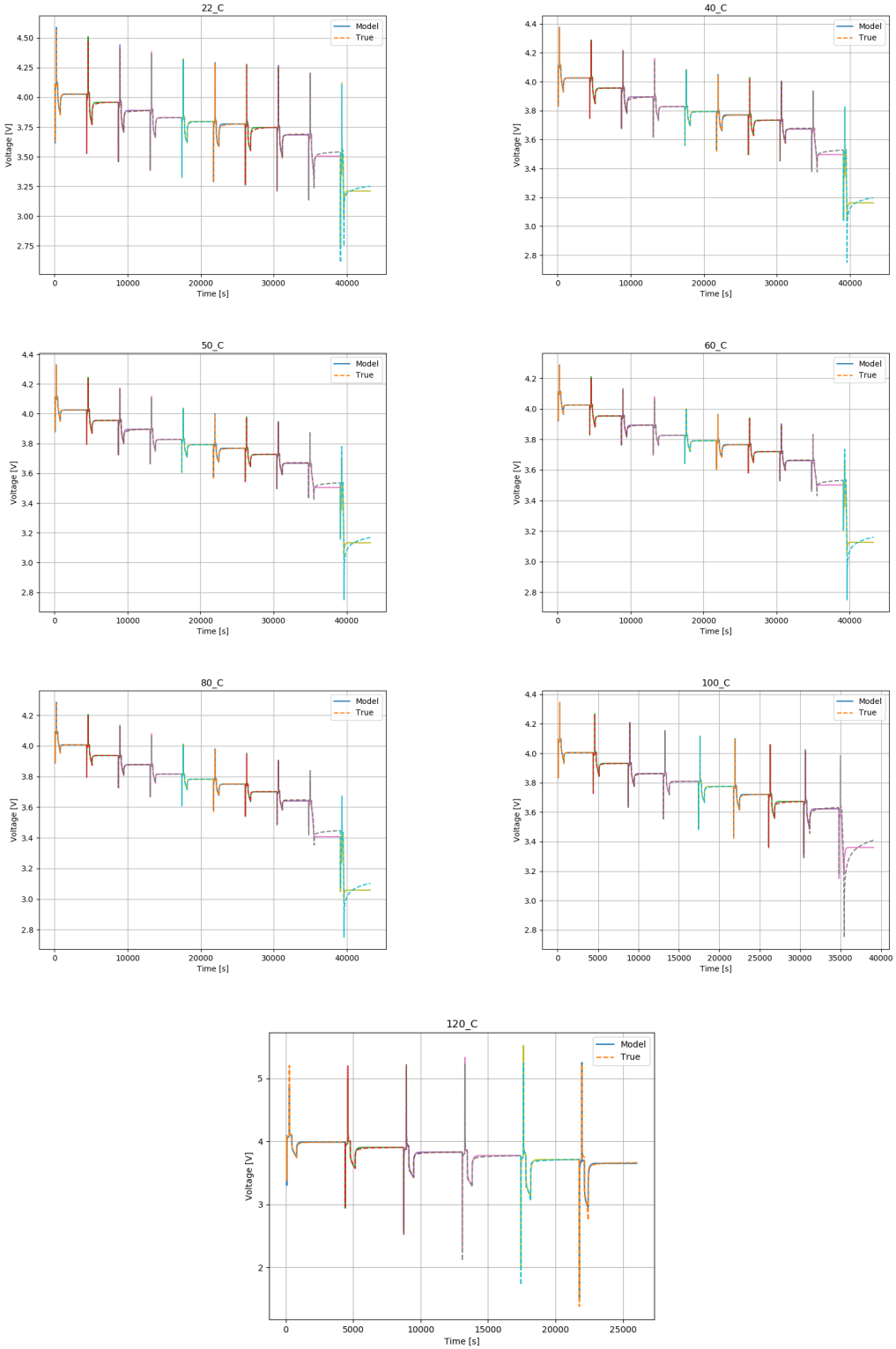

Figure 4.18: Fits with fixed time constants and SOC dependence

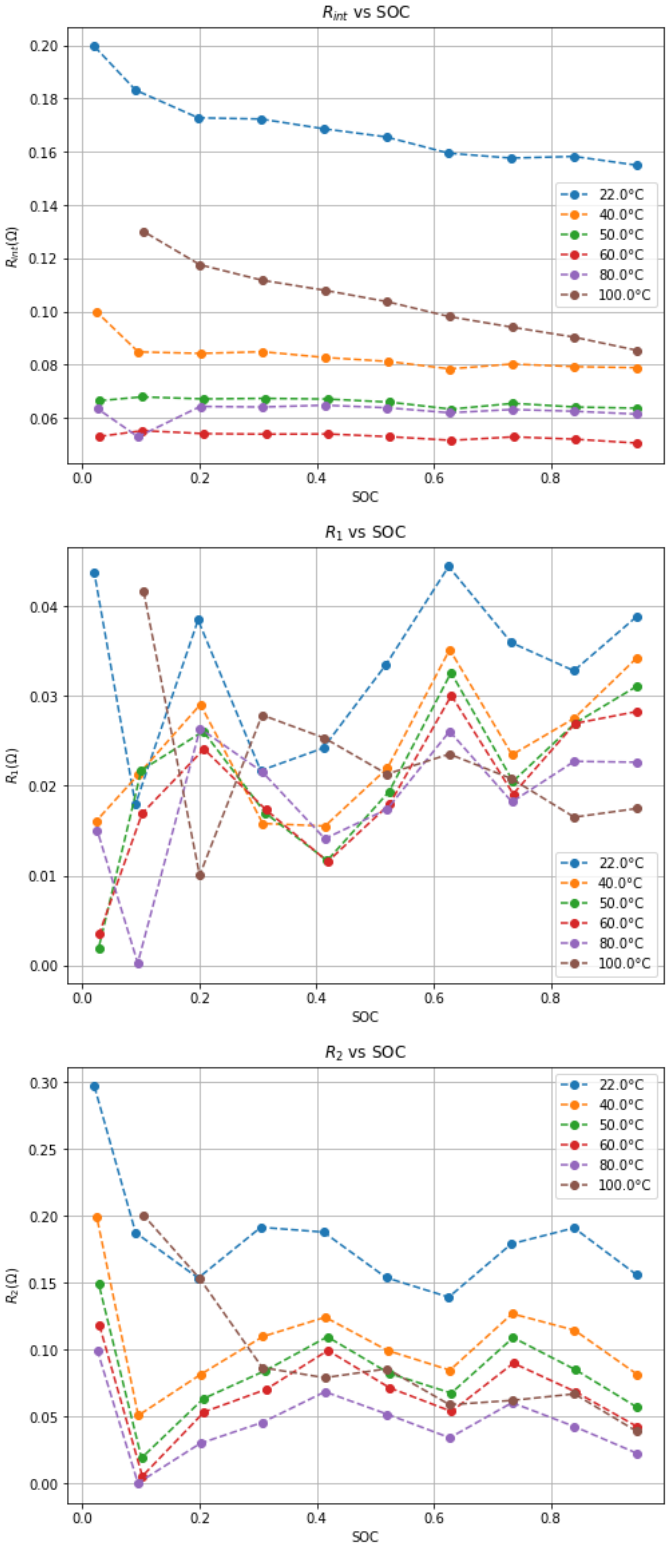

Figure 4.19: Fixed time constants and SOC dependence - ECM parameters

4.3.2.4 Variable Time Constants and SOC Dependence (VTSD)

This model has the most comprehensive definition. With SOC and temperature dependence incorporated into ECM parameters, it is expected to achieve the highest level of accuracy out of all the cases.

In figure 4.20, data fits at different temperatures are plotted. The main difference between this case and the previous case can be observed at time 10000 seconds when the SOC of the battery is around 70%. At low temperatures, the difference is visually perceptible. The voltage response is more closely fitted due to the removal of the constraint on time constants. For 22°C, at around 40% SOC, another noticeable improvement is seen.

Figure 4.21 shows the variation of different ECM parameters with SOC at six temperatures. The trend in the internal resistance is close to what is shown in the FTSD case. One discrepancy can be spotted in the 100°C plot. where the internal resistance of the LIB at low SOC saturates at 0.119 Ω, however, the FTSD plot shows an increasing behavior.

The behavior of R_1 shown by VTSD is starkly different from what is observed in FTSD. The order of magnitude of R_1 values has increased in the VTSD model. Starting from 100% SOC, the FTSD model suggests that the value of R_1 decreases till 80% SOC is reached; however, the opposite is observed in VTSD. The maxima stays at 70% SOC for most cases in both the model results. In VTSD, the maxima shifts from 90% SOC to 70% SOC as the temperature goes from 22°C to 50°C. The position of the second maxima occurs at 40% SOC for all FTSD cases and most VTSD cases. Relative to the first maxima values, the second maxima values don't change much in the FTSD model; however, the VTSD model shows a decrease. At low SOC, the variation in R_1 with temperature becomes more divergent. Interestingly, the τ_1 values follow the same direction as R_1. One can see why choosing a fixed time constant value could lead to potential prediction errors. Barring a few outliers, the short time constant of the LIB decreases with increasing temperature. This can be interpreted as the increase in the rate of the charge transfer process,

which is characterized by τ_1.

Except for the jump observed at low SOC, the magnitude and variation of R_2 remain consistent with the change in the model. In contrast to R_1 behavior, R_2 first decreases as the SOC decreases to 70%, where it reaches a minimum, after which it rises till 40% SOC, and decreases again. τ_2 and τ_1 follow a very similar trend. This shows that the rate of diffusion increases with temperature till 80°C, after which it increases. This change can be ascribed to the degradation of the battery, which leads to increased response time to change in current.

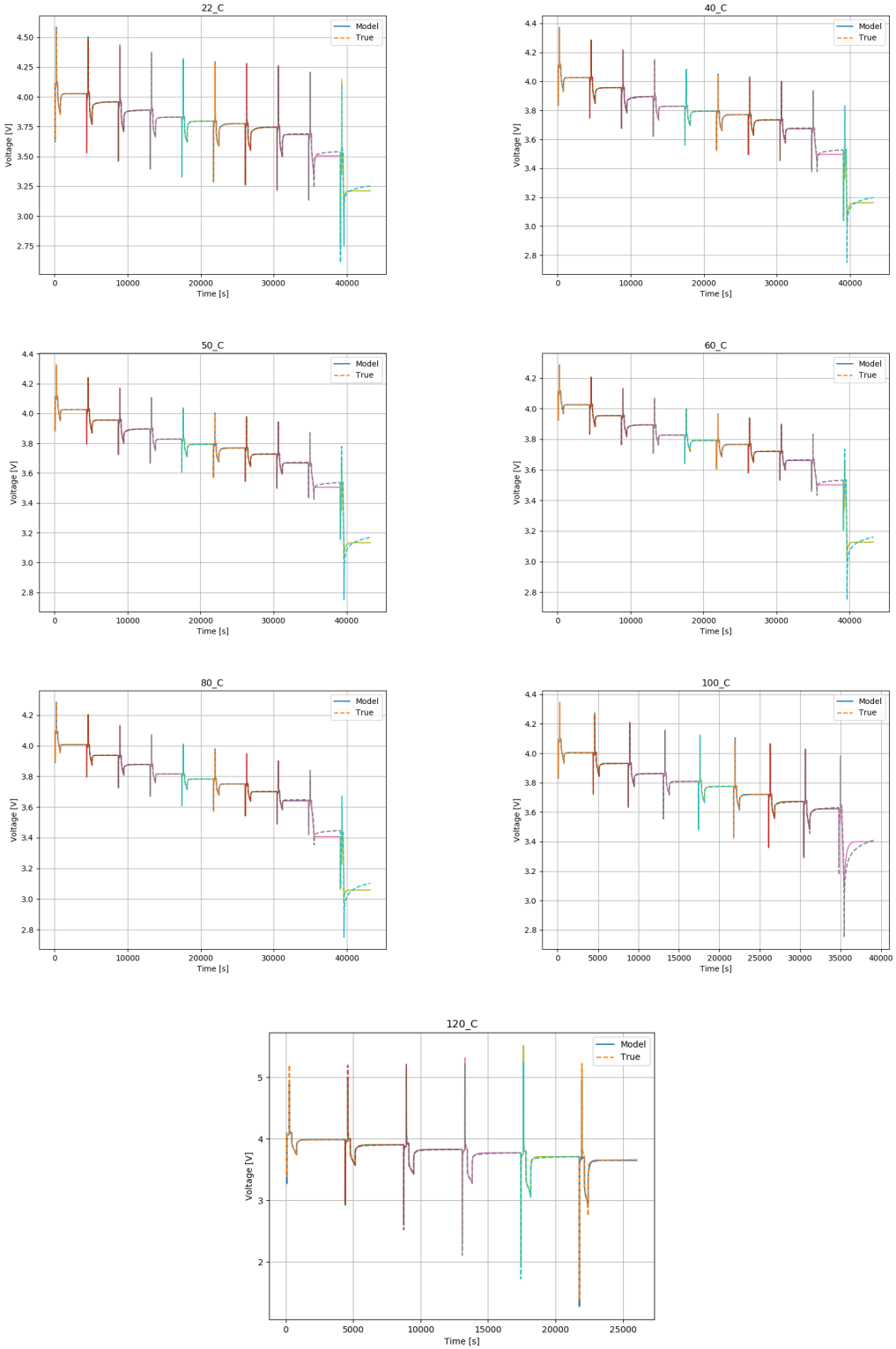

Figure 4.20: Fits with flexible time constants and SOC dependence

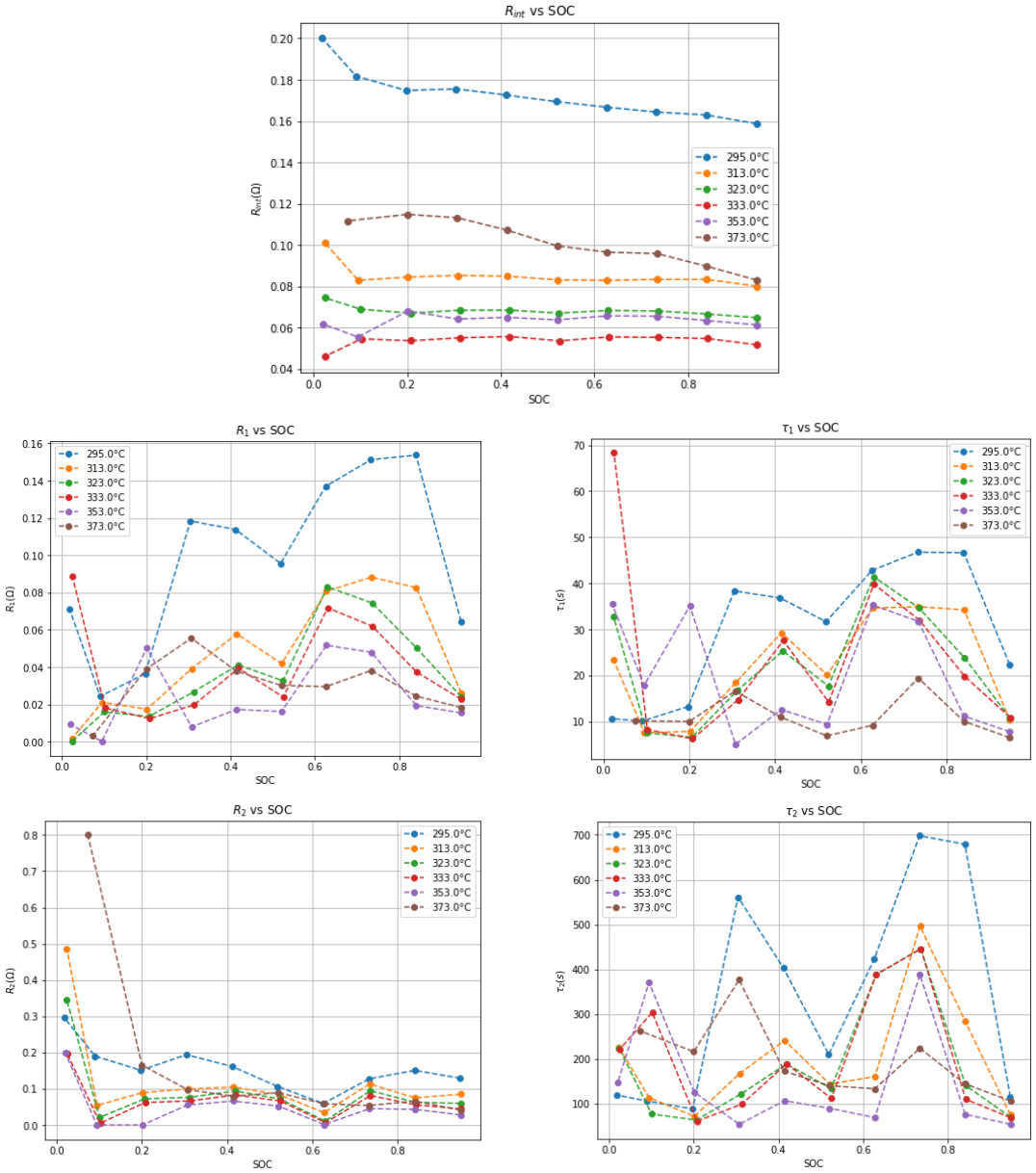

Figure 4.21: Flexible time constants and SOC dependence - ECM parameters

In conclusion, all three cases have their pros and cons. If a system is expected to utilize batteries at normal operating temperatures and limited SOC range, then case 1 is sufficient to model and predict its performance. Above those temperatures, the model defined by the results of cases 2 and 3 should be deployed for BMS. Case 3 captures the change in time response of the LIB with SOC and temperature, however, its impact is small and is observed only at 40% and 70% SOC region. Irrespective of the thermal conditions, one can see that an appropriate ageing model has to added to the DP model to ensure long-term applicability and accuracy.

5 Equivalent Circuit Model - Prediction

The aim of this thesis is to push the limits of a simple DP model and analyze its range of operation. The DP model requires the least number of parameters and, consequently, is easy to setup. Thus, the following sections compare model performance with experimental data to see the effect of the depth of parameterization, that is, the effect of SOC and temperature dependence of said parameters.

5.1 Experiment Setup

To attain high cell temperatures without any external heat source, the cell is cycled at a high C-rate in near adiabatic conditions. The same apparatus, described in section 4.1.3, is used for battery cycling and data acquisition.

The setup to maintain near adiabatic conditions is simpler than that of isothermal conditions. The fixture, designed to maintain a constant temperature, is replaced with ceramic insulation of thermal conductivity (λ_{ins}) approximately equal to 0.047 $Wm^{-1}K^{-1}$, volumetric heat capacity equal to 145.9 $kJm^{-3}K^{-1}$, and the thickness of the insulation (l_{ins}) is 1.91 cm [63]. The heat transfer coefficient used in this work is calculated in section 5.3.2.

For all the cases studied, the battery sits at room temperature initially. Different current profiles are then applied to achieve high battery temperatures.

Model	Voltage RMSE (V)
Linear fit	0.0114
Polynomial fit	0.0162

Table 5.1: Test 1 - C/2 discharge rate - RMS errors

5.2 Results

A number of tests are conducted to observe the voltage and temperature response of LIB to varying current profiles.

5.2.1 Test 1 - OCV Check

The first step of ECM validation is chosen to be a simple discharge test. This validation test is used to give an insight into the functioning of the ECM circuit under nominal conditions. A fresh LIB is taken for the test, wherein, the battery is discharged at C/2 rate.

The OCV functions used for this analysis are the 2D map of linear interpolation OCV and 2D map of polynomial profiles. These 2D maps capture the effect of both, SOC and temperature. Figure 5.1 shows the mapping functions used for all the analyses that follow.

Observations

The battery is discharged for 6000 seconds at C/2 rate till it reaches 20% SOC. The linear and polynomial fits to the experimental data are shown in figures 5.2 and 5.3 respectively. The associated RMS errors for these fits are tabulated in table 5.1.

The polynomial fit is oscillatory as opposed to the linear fit, which is more streamlined. For the linear fit, the OCV dip is not as steep as expected in the low SOC. This leads to incorrect estimation of the voltage, as seen in figure 5.1. Overall, the linear fit follows the actual trend more closely than the polynomial profile fit, however, the opposite is true in the low SOC region.

Analysis

As the battery stays above 20% SOC throughout the test, the sharp dip in voltage in the 0 SOC region is not observed. The polynomial profile is matching the exact profile periodically. The error is maximum when the profile battery SOC is in between two SOC values at which the open circuit voltage is known.

A possible source of error can be perceived from 2D mapping. As observed in a multitude of studies [60, 59], the low SOC region is the most difficult to deal with, the reason being the uncertainty in the capacity of the battery. Even a small error in the capacity specification can lead to large errors in low SOC voltage estimations. The characterization of the point of a sharp dip in voltage in the low SOC region requires more experimental data points. An alternate way of OCV measurement, like very slow discharge (C/10 or C/15 rate), can prove to be more useful. This low discharge rate negates the effect of battery internal resistance and kinetics (quasi-static process), and the output voltage is simply equal to OCV.

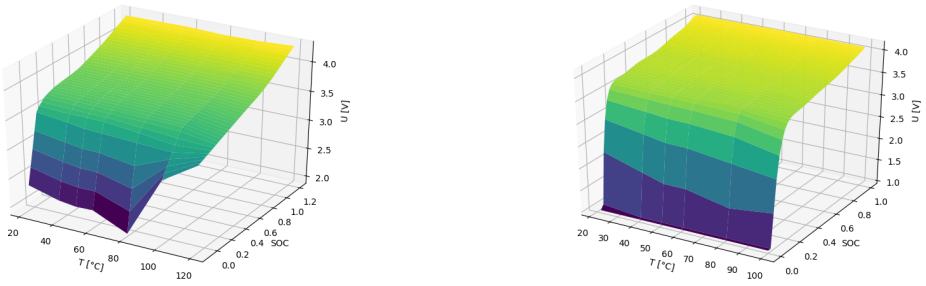

(a) Linear fit (b) Polynomial fit

Figure 5.1: 2D mappings of OCV

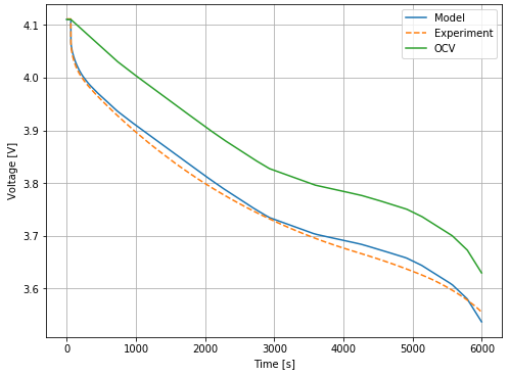

(a) FTSI

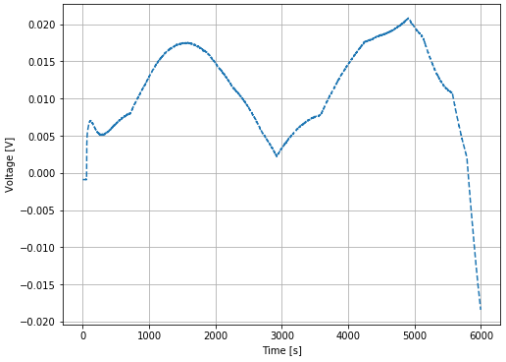

(b) FTSI error

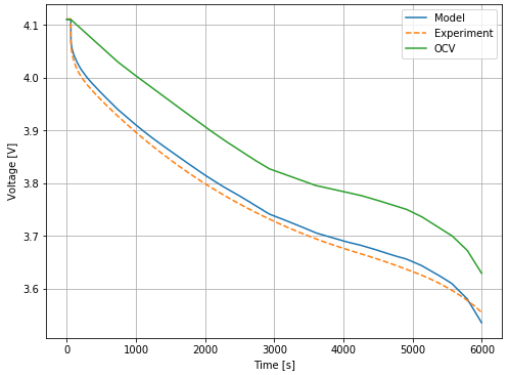

(c) FTSD

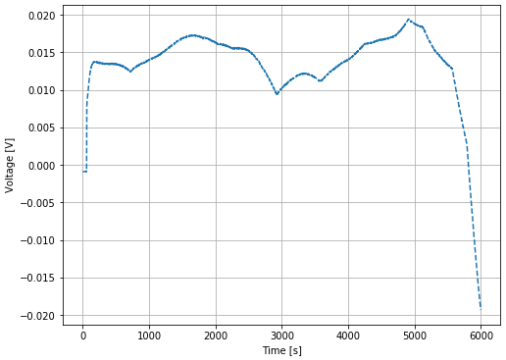

(d) FTSD error

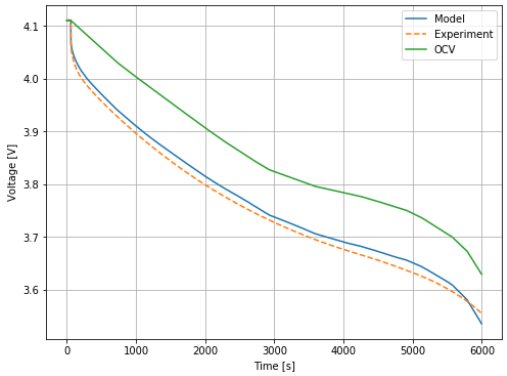

(e) VTSD

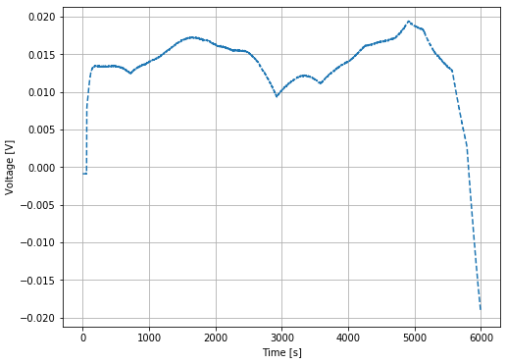

(f) VTSD error

Figure 5.2: Piece-wise linear OCV fit results

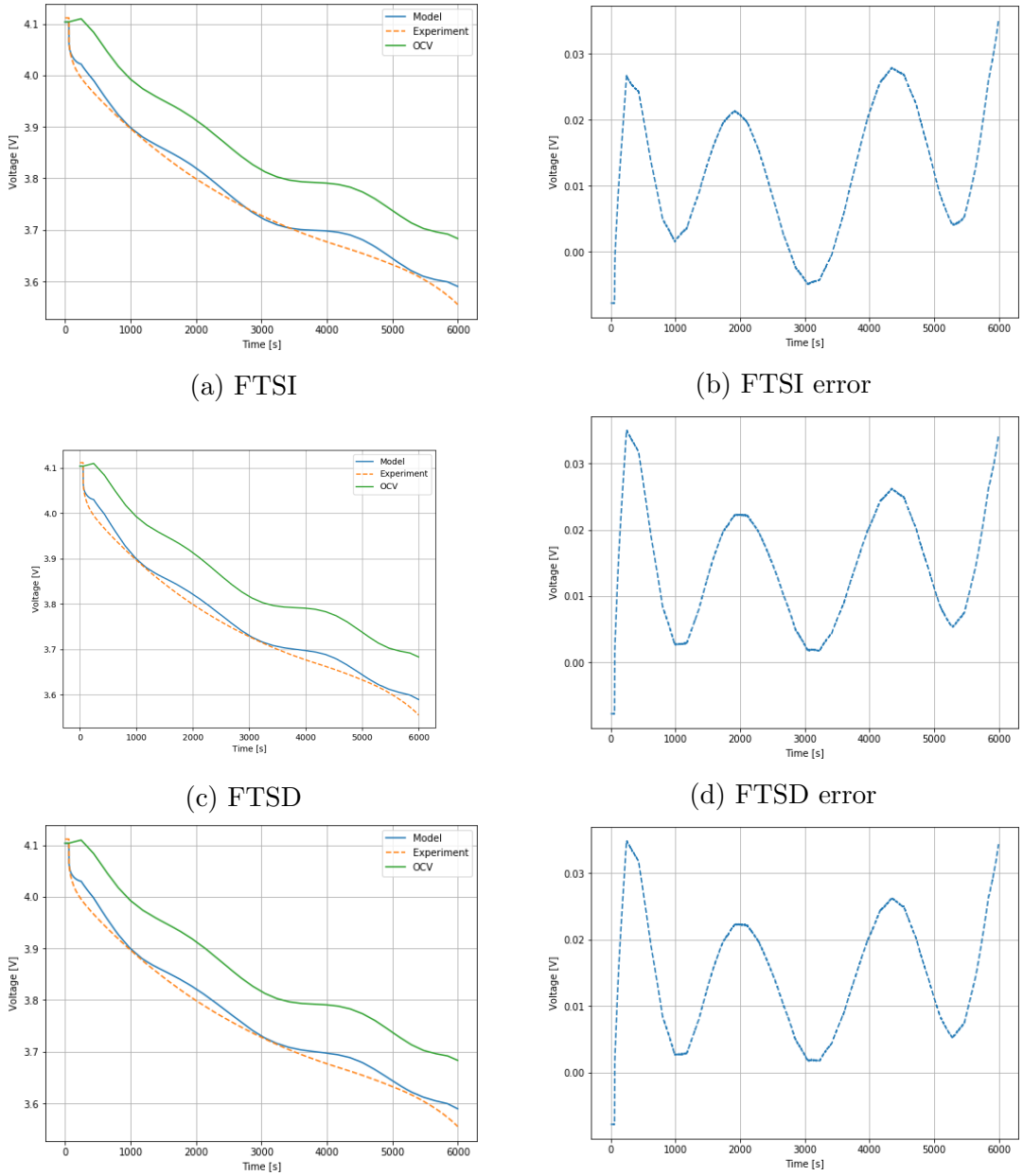

(a) FTSI

(b) FTSI error

(c) FTSD

(d) FTSD error

(e) VTSD

(f) VTSD error

Figure 5.3: Polynomial fit results

5.2.2 Test 2 - Natural Convection

Before high temperature analyses, an ambient temperature and natural convection cooled scenario is first considered. The same HPPC profile is applied to a cell standing vertically in ambient air. The heat transfer coefficient of the setting is calculated using equation 9.27 from *Fundamentals of Heat and Mass Transfer* [25], which comes out to be around 3.5 $Wm^{-2}K^{-1}$.

Observations

Figures 5.4, 5.5 and 5.6 juxtapose experimental data with results obtained from FTSI model, FTSD model, and VTSD model respectively. The maximum variation in temperature and voltage prediction is seen in the FTSI results. FTSD and VTSD give very similar solutions.

The low SOC region is the part with the highest deviation from the experimental data for all the models. The FTSI model gives a peak voltage error of 0.3 V, and the rest give a peak voltage error of 0.2 V. Otherwise, the errors in FTSD and VTSD are less than 0.02 V.

The temperature output of the FTSD and VTSD models seem to agree better with the actual data than the FTSI model for the most part. The temperature plot exhibits a peculiar behavior in the low SOC region where the peak temperature goes down. From the heat generation subplots, one can see the jump in reversible heat source term near the end of the cycle, which acts as an endothermic heat source term.

Analysis

As expected, the temperature spikes are observed in the high C-rate pulse regions. Since, the LIB is placed in ambient condition, the variation in temperature is not high (2-4°C). FTSI model uses SOC-independent R_{int} values which is a particularly erroneous assumption at ambient temperature, thus, the deviation of the FTSI output from actual result is consistent with the expectations.

The error in capacity evaluation or OCV measurement at low SOC penetrates more strongly into FTSD and VTSD models as the ECM parameters are dependent on SOC (which is calculated using capacity), and the reversible heat term $\frac{dU}{dT}$.

The RMS errors are listed in table 5.2. Again, aligning with expectations, the least error is observed in VTSD and FTSI results gives the highest deviation. However, these numbers need to be viewed with caution, as the least count of the data

Model	Temperature RMSE (°C)	Voltage RMSE (V)
FTSI	0.1847	0.0156
FTSD	0.1754	0.0138
VTSD	0.1743	0.0138

Table 5.2: Test 2 - Natural Convection - RMS errors

acquisition devices used are quite moderate: 1 significant digit in temperature measurement and 4 in voltage measurement. Thus, the uncertainty associated with the experimental data needs to be accounted for.

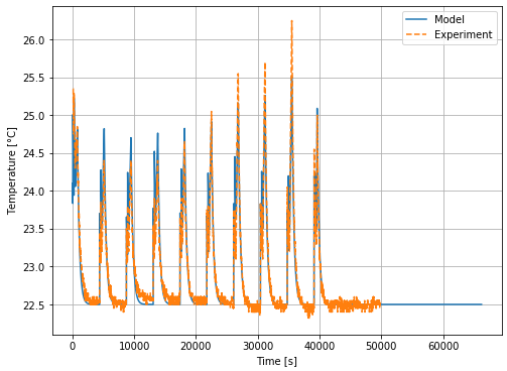

(a) Temperature

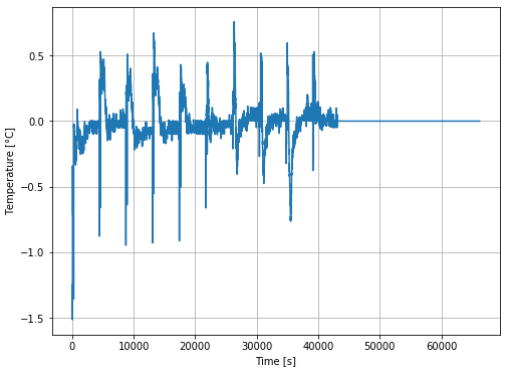

(b) Temperature error

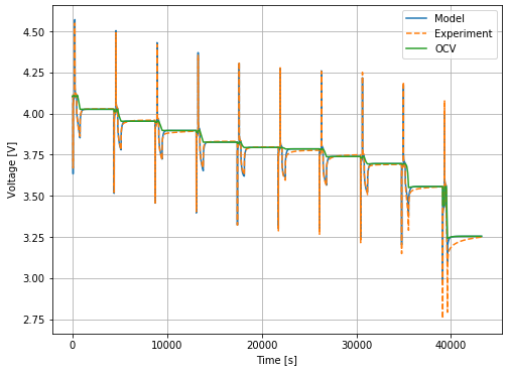

(c) Voltage

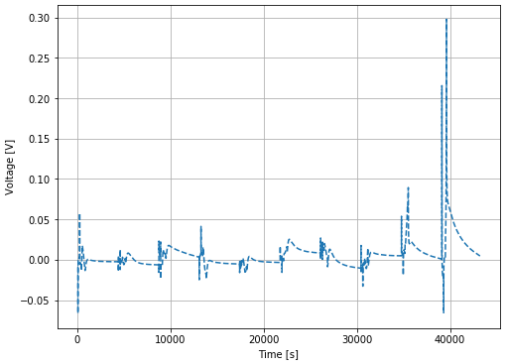

(d) Voltage error

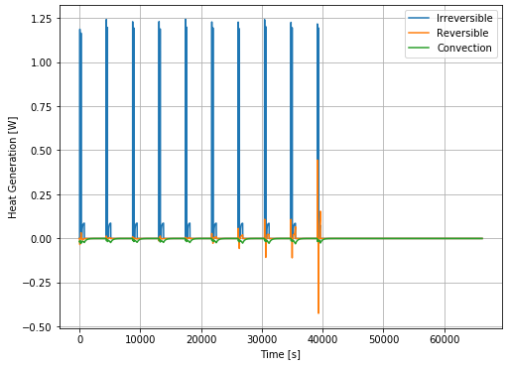

(e) Heat generation

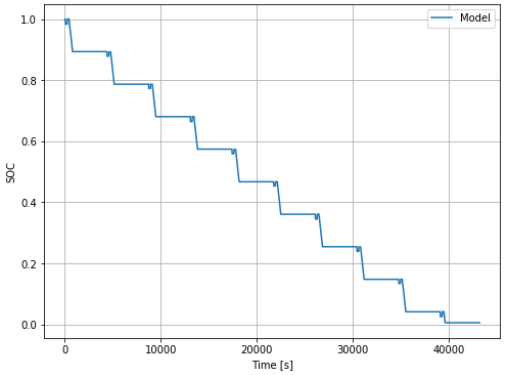

(f) SOC

Figure 5.4: Test 2 - Natural Convection - FTSI results

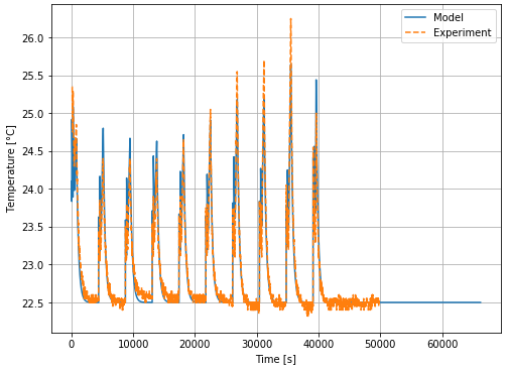

(a) Temperature

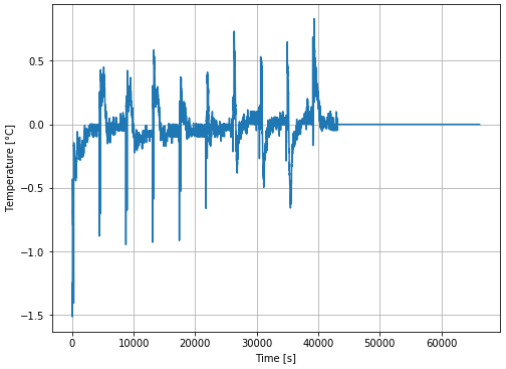

(b) Temperature error

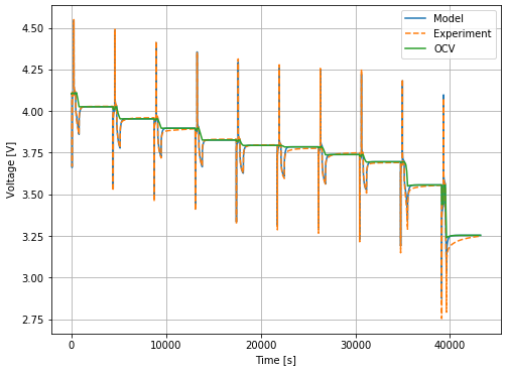

(c) Voltage

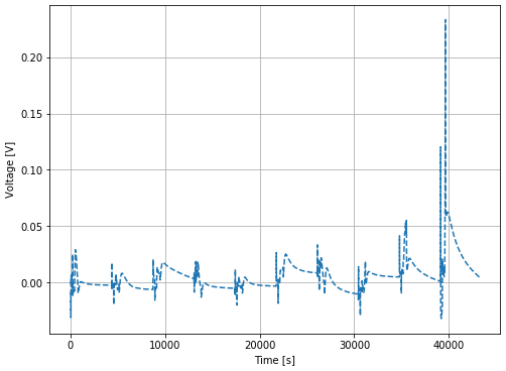

(d) Voltage error

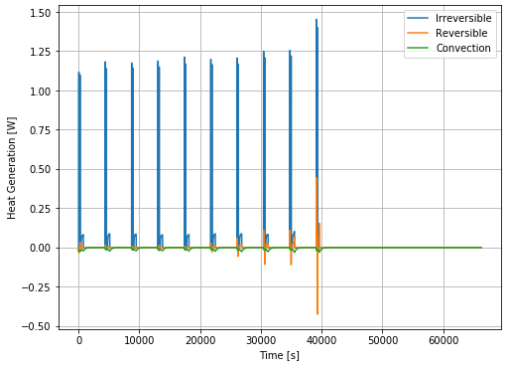

(e) Heat generation

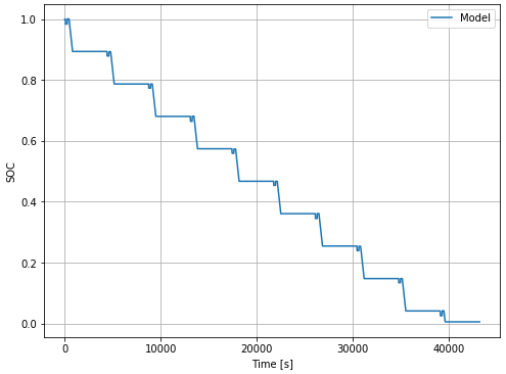

(f) SOC

Figure 5.5: Test 2 - Natural Convection - FTSD results

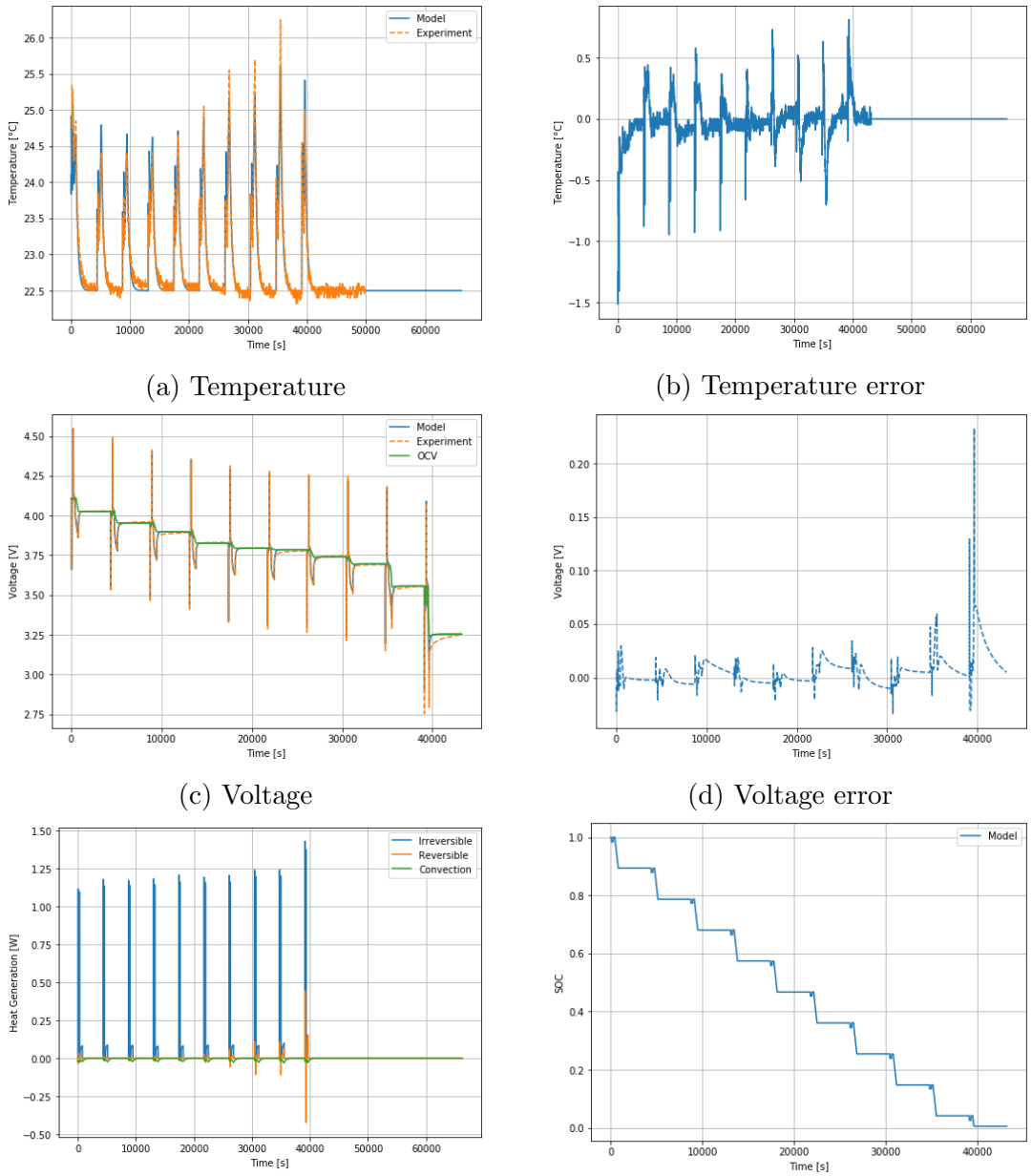

(a) Temperature

(b) Temperature error

(c) Voltage

(d) Voltage error

(e) Heat generation

(f) SOC

Figure 5.6: Test 2 - Natural Convection - VTSD results

5.2.3 Test 3A - 5C pulsing (Voltage Constraint)

From now on, all the tests are conducted in insulated battery conditions. The battery is wrapped in a ceramic fiber blanket which is manufactured from alumina-silica bulk fibers. As mentioned before, the insulator has low thermal conductivity and heat storage properties (low specific heat, thus, proving to be an efficient and inexpensive insulator for LIB test requirements. For this case, the cell is wrapped

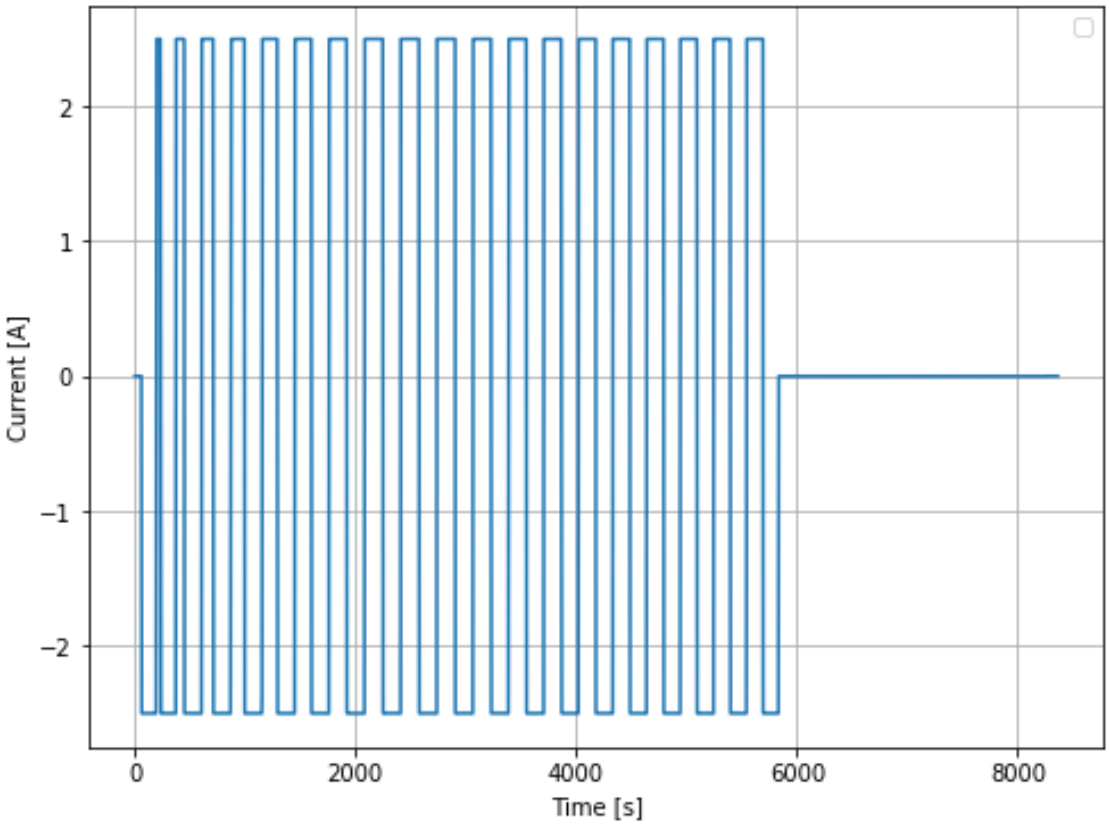

Figure 5.7: Test 3 - 5C pulsing (Voltage Constraint) - Current profile

in two layers of insulation. A weight is also placed over the wrapped arrangement to ensure better contact with insulation.

The current profile for this case is shown in figure 5.7. It is a cyclic process: 5C discharge current is supplied till voltage reaches 2.75V and then it switches to a charge current of 5C till voltage reaches 4.2V.

Observations

The current profile shows that the LIB goes from 4.2 V to 2.75 V very quickly at the beginning of the cycling process. After 3 cycles, the current profile stays uniform until the end of the process.

Figures 5.9, 5.10, and 5.11 show the battery response to the aforementioned current profile. The most erroneous prediction is of LIB voltage. Such periodic drops in voltage for the given current profile can be observed only when the battery reaches

near 0 SOC. This means that the capacity of the battery is lower than the nominal capacity. For the present test, if the capacity is decreased to 0.315 (30% less than the nominal capacity), then the model is able to match the dips, however, all the other regions diverge from the actual value.

The SOC variation predicted by the model shows that the model LIB does not go below 35% SOC. However, as discussed before, the experimental behavior does not corroborate the model voltage output at the end-of-discharge sections.

The actual temperature profile aligns with general expectations. The peaks occur when the current switches from discharge to charge mode, and the troughs occur when the current changes back to discharge mode. One can discern from the FTSI fit that it fails to model the cyclic peaks. Its temperature prediction is uniformly oscillating, in contrast to the alternating peaks observed in the actual data. The FTSD model slightly underestimates the temperature as compared to the VTSD model. It is also interesting how the inaccuracy in low SOC voltage prediction doesn't drastically affect the temperature prediction.

Analysis

The temperature trend shows that the model reaches a steady range more quickly, which is in contrast to the damped growth exhibited by the actual case. This can be attributed to the cyclic degradation of the cell. As the LIB is cycled with increasing temperatures, the SEI growth gets accelerated. A direct consequence of this growth is the increase in path resistance for lithium intercalation in the anode. More details are discussed in the following section where these effects are empirically modeled and integrated into the current DP model.

The heat generation plot shows that the reversible component cannot be ignored. Simulation of two cases, with and without the reversible heat term, is shown in figure 5.8. Its endothermic characteristic, that contributes greatly at the beginning of each discharge part, becomes apparent in the figure. There are sections wherein it exceeds the irreversible heat term. Thus, its contribution is of importance when

Model	Temperature RMSE (°C)	Voltage RMSE (V)
FTSI	3.296	0.1107
FTSD	2.625	0.104
VTSD	2.524	0.1031

Table 5.3: Test 3 - Test 3A - 5C pulsing (Voltage Constraint) - RMS errors

dealing with current pulsing.

Again, the RMS error suggests that the VTSD results are closest to the experimental data. Interestingly, FTSI gives a lower error than FTSD. However, as observed from the plots, FTSI fails to capture the trend in temperature variation. Thus, the VTSD model is used to model all test cases that follow.

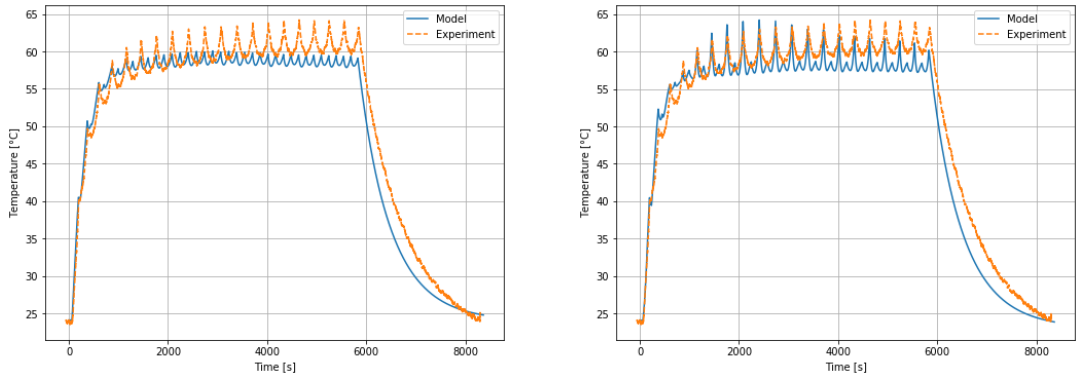

(a) No irreversible heat term

(b) With irreversible heat term

Figure 5.8: Effect of irreversible heat - 5C pulsing (Voltage Constraint)

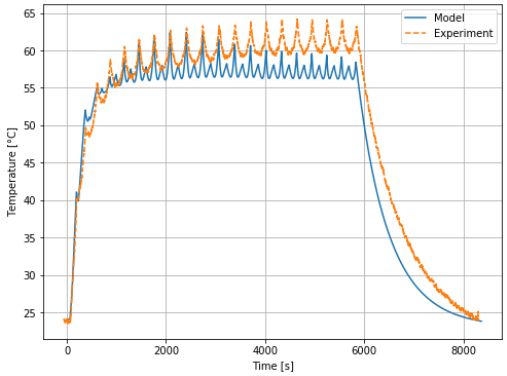

(a) Temperature

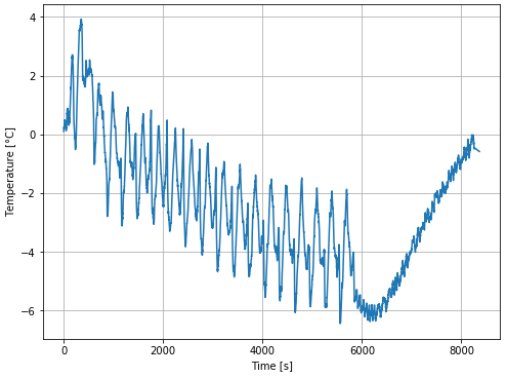

(b) Temperature error

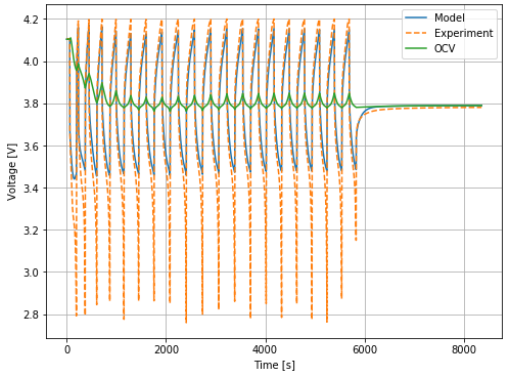

(c) Voltage

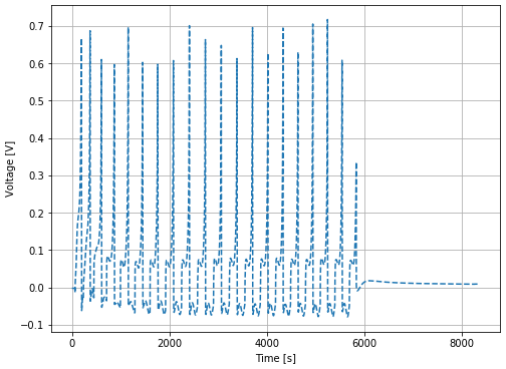

(d) Voltage error

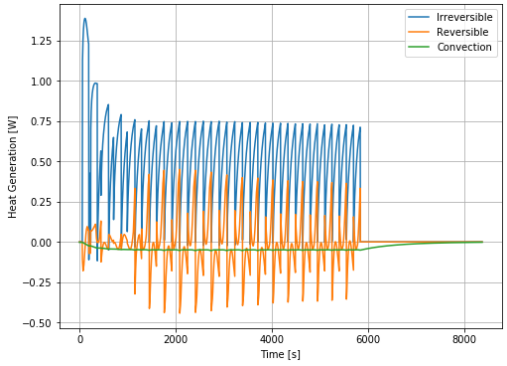

(e) Heat generation

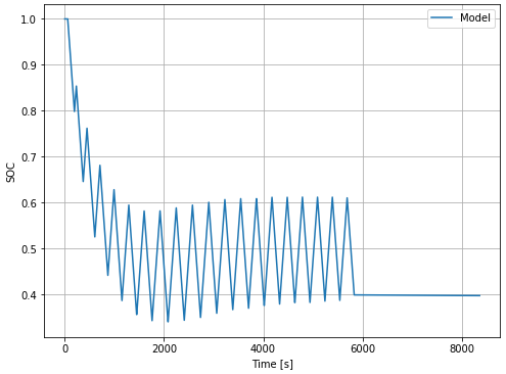

(f) SOC

Figure 5.9: Test 3 - 5C pulsing (Voltage Constraint) - FTSI results

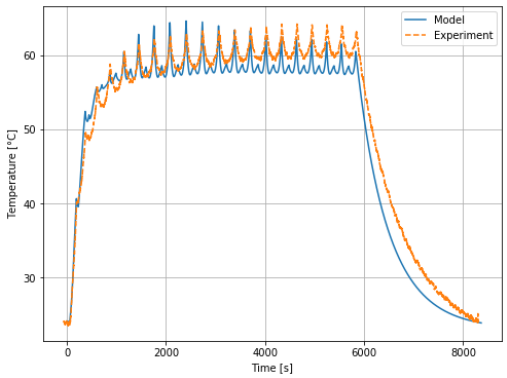

(a) Temperature

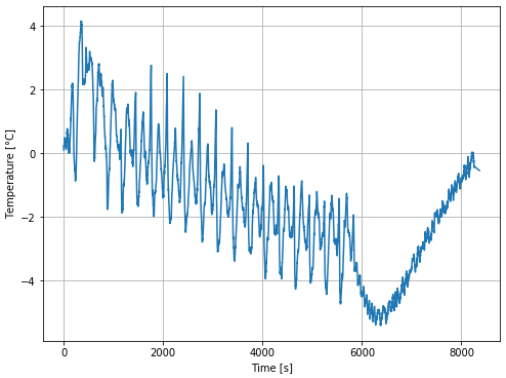

(b) Temperature error

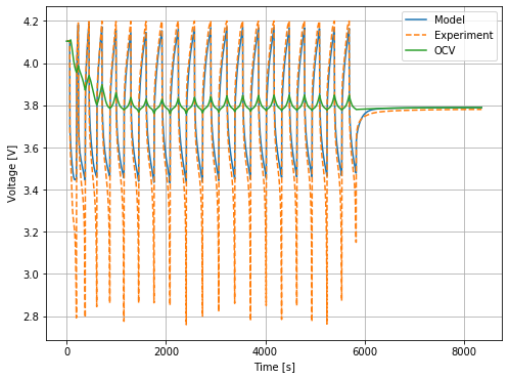

(c) Voltage

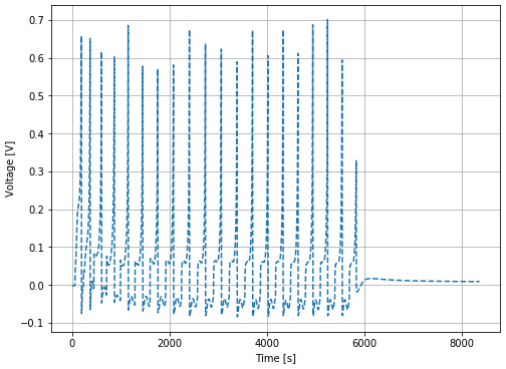

(d) Voltage error

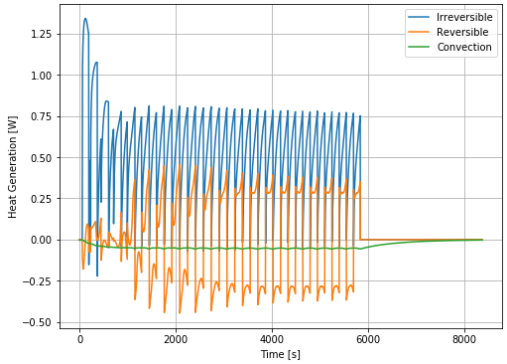

(e) Heat generation

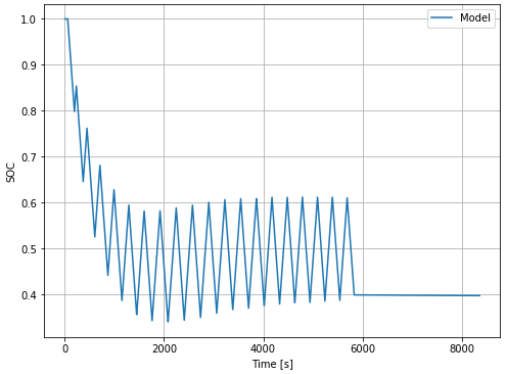

(f) SOC

Figure 5.10: Test 3 - 5C pulsing (Voltage Constraint) - FTSD results

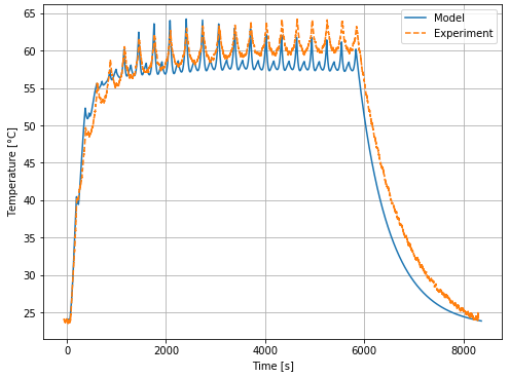

(a) Temperature

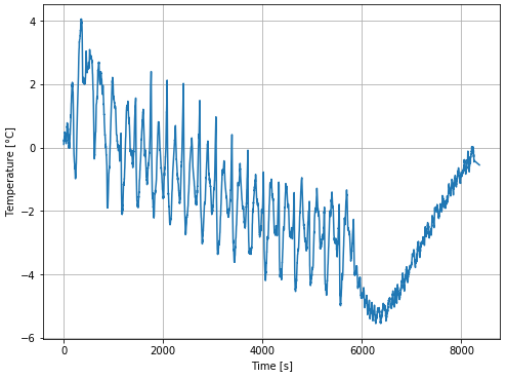

(b) Temperature error

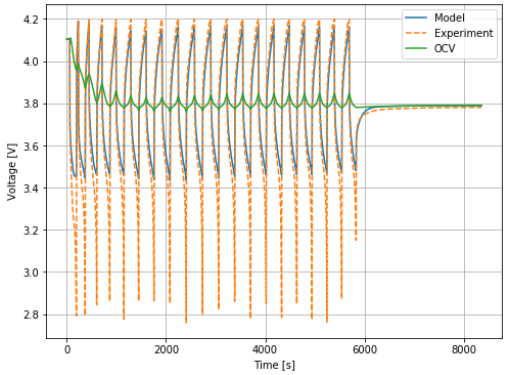

(c) Voltage

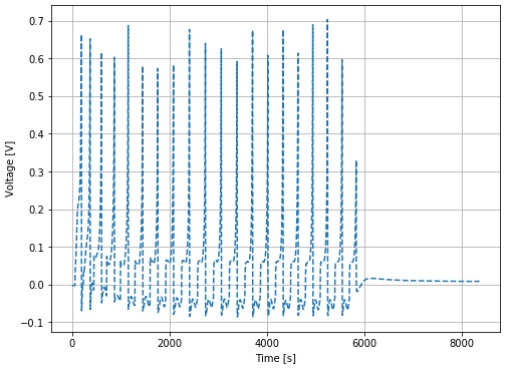

(d) Voltage error

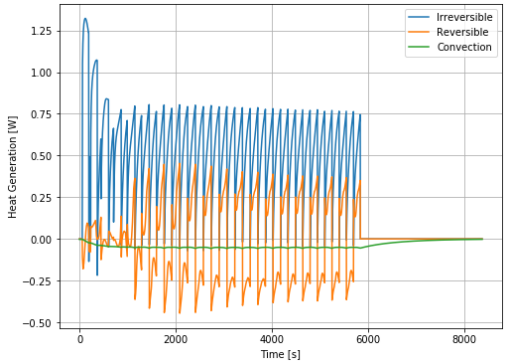

(e) Heat generation

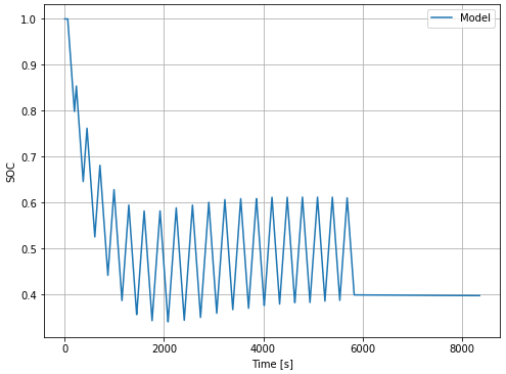

(f) SOC

Figure 5.11: Test 3 - 5C pulsing (Voltage Constraint) - VTSD results

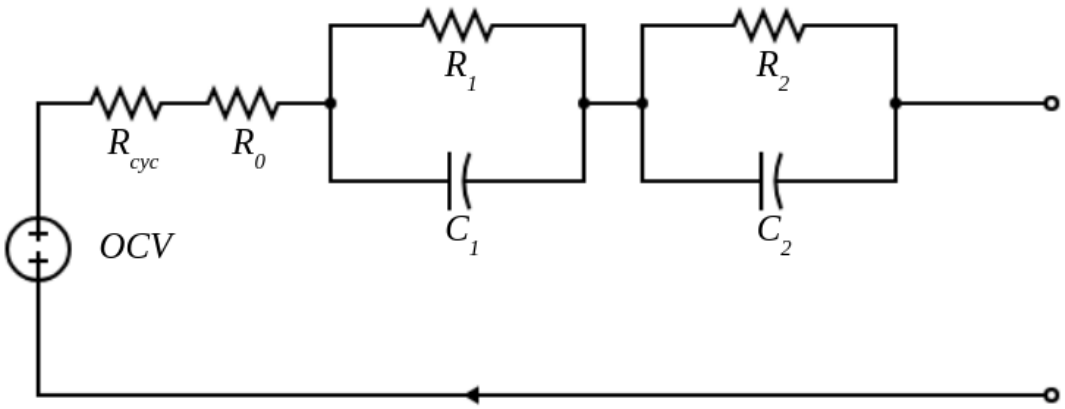

Figure 5.12: Modified DP model

5.3 Simple Model Modifications and Preliminary Results

To model the transition to abuse conditions, it is mandatory to have some way of addressing each phase that occurs during this transition. Processes like capacity fade, increase in internal resistance and parasitic side reactions have to be included.

As the aim of this thesis is to model battery operation using a simple and fast method, the DP model is slightly modified, as shown in figure 5.12.

The modifications include the addition of a cycling resistance and a variable capacity. Taking inspiration from the SEI layer growth theory [27], the cycling resistance is defined in a very simple fashion. The SEI layer thickness is shown to have a $\sqrt{t}$ dependence under certain assumptions [28]. Extending that result, it is assumed that the increase in the internal resistance of LIB due to SEI growth can be modeled as follows,

$$R_{cyc} = a_{cyc} N^{1/2} \tag{5.1}$$

where a_{cyc} is the cyclic coefficient, and N is the number of cycles. It should be noted that a_{cyc} is a function of SOC, temperature, current, and its direction. However, for demonstration purposes, a constant value is fitted for each test.

The rate of change of capacity (C_c) can be broken down into two terms, simplifying

equation 27 from Schimpe [64],

$$\Delta C_c = \int_0^t \frac{dC_{c,calendar}}{d\tau} d\tau + \int_0^{C_c} \frac{dC_{c,cyc}}{dq} dq \tag{5.2}$$

where the 2 terms represent capacity loss due to calendar ageing and cycle ageing respectively. The calendar ageing rate is integrated with time and the cyclic ageing change is integrated with the amount of charge put into the battery. The upper limit of the integral for the cyclic term is set to be C_c since we are always charging the battery from 0 SOC to 100 SOC in each cycle.

The variable capacity aspect is implemented by adding an Arrhenius temperature dependence on C_c in the SOC circuit, as shown in figure 2.5. Mathematically,

$$\frac{dC_{c,calendar}}{d\tau} = -k_{cal}\tau^{-0.5} e^{-\frac{E_{a,cal}}{R}(\frac{1}{T}-\frac{1}{T_{ref}})} \tag{5.3}$$

$$\frac{dC_{c,cyc}}{dq} = -k_{cyc,1} q^{-0.5} e^{-\frac{E_{a,cyc,1}}{R}(\frac{1}{T}-\frac{1}{T_{ref}})} - sgn(I) k_{cyc,2} q^{-0.5} e^{-\frac{E_{a,cyc,2}}{R}(\frac{1}{T}-\frac{1}{T_{ref}})} \tag{5.4}$$

The parameters for this addition, namely, stress factors k and the activation energies E_a are taken from [64]. If one assumes isothermal conditions, the equations can be be integrated analytically. The $\sqrt{t}$ dependence from the SEI theory is again put to use in modeling calendar ageing. The cyclic loss term is proportional to the $\sqrt{C_c}$, as shown in [64]. An additional term is added to cyclic ageing to account for the lithium plating losses, occurring due to the high charge rate. In this work, the above mentioned equations are discretized in time and numerically integrated at every time step.

5.3.1 Test 3B - 5C pulsing (Voltage Constraint)

The improved capabilities of the modified model are verified by comparing its results with test 3A predictions.

Observations

The results are shown in figures 5.13 and 5.14. Just from a cursory glance, the improvement in temperature accuracy is apparent. According to the modified model, the steady growth in temperature is primarily governed by the increase in internal resistance. The plot of heat generation terms shows a uniform increase in the irreversible heat term, which is directly proportional to the internal resistance of the LIB.

The SOC plots show how the addition of the capacity fade model impacts the voltage response. The error in voltage prediction slightly decreases, thus, validating the idea of cyclic capacity degradation.

A discrepancy can be observed in the modeling of heat loss in the post-cycling phase. A more sophisticated method of insulation is required to isolate the heat generation terms that arise from the battery, thus, eliminating the need to analyze heat loss.

Analysis

The error in voltage decreases slightly because of the addition of the capacity fade model. The gradual change in the range of SOC covered by each cycle goes to show how the decrease in the state of health impacts the SOC variation. However, due to the lack of precision in OCV-SOC fit, and inaccuracy in the initial capacity value, the model is not able to fully correct the voltage prediction.

The trend of the wavy temperature profile is nicely captured by the presented model. As explained in the previous case, cell degradation due to high C-rate cycling is expected to be the main cause of the slow growth in the average temperature of the cell. The old model attains a steady balance between the heat generation terms, causing it to predict a steady profile. With the addition of the internal resistance and capacity fade model, the model is able to capture the effect of the underlying physical processes more accurately.

Table 5.4 quantifies the difference between the accuracy of each model. As expected, the modifications improve the temperature and voltage prediction capabilities of the existing DP model.

Since the battery is doubly wrapped in a ceramic blanket with weight placed on it, a more simple and tractable arrangement is needed. The passage for wires coming out of the apparatus also provides a path for air circulation. Additionally, as shown by Headley [65], the thermal conductivity of the ceramic blanket increases with increase in temperature, which has not been incorporated in the analysis.

Model	**Temperature RMSE (°C)**	**Voltage RMSE (V)**
3A	2.524	0.1031
3B	1.796	0.0987

Table 5.4: Test 3 - 5C pulsing (Voltage Constraint) - RMSE errors

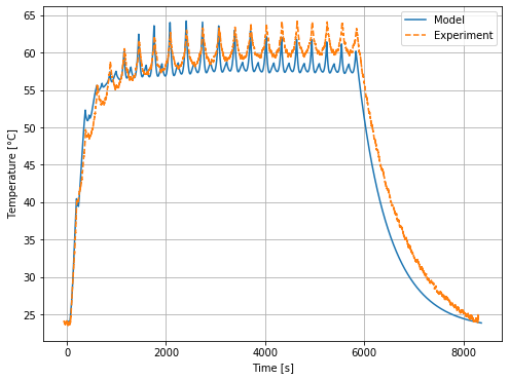

(a) Temperature - Old

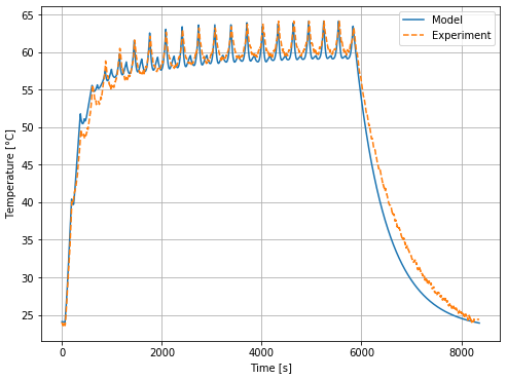

(b) Temperature - Modified

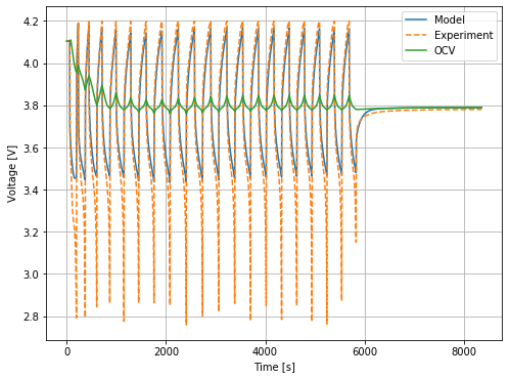

(c) Voltage - Old

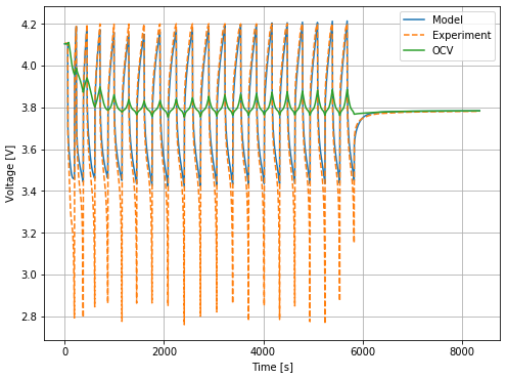

(d) Voltage - Modified

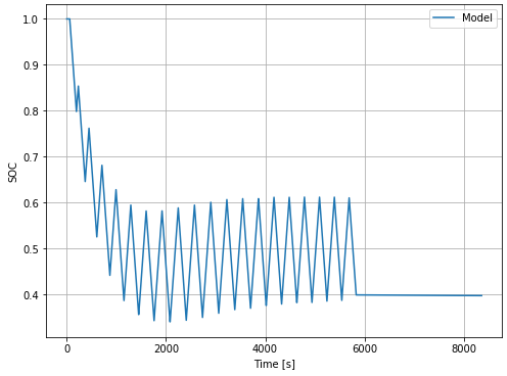

(e) SOC - Old

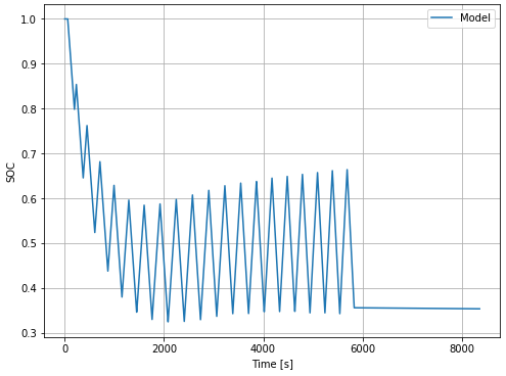

(f) SOC - Modified

Figure 5.13: Test 3 - 5C pulsing (Voltage Constraint) - Model comparison I

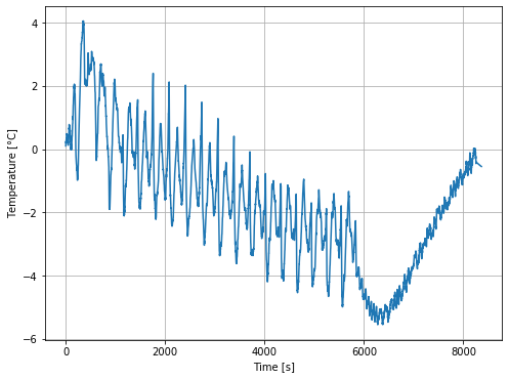

(a) Temperature error - Old

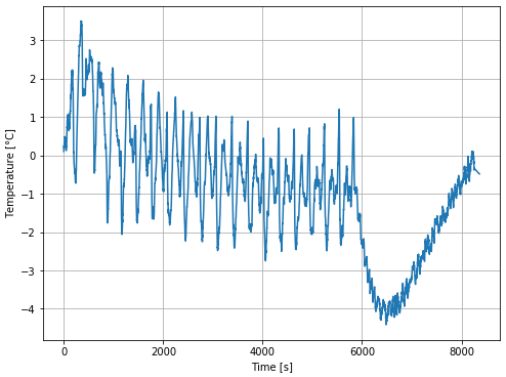

(b) Temperature error - Modified

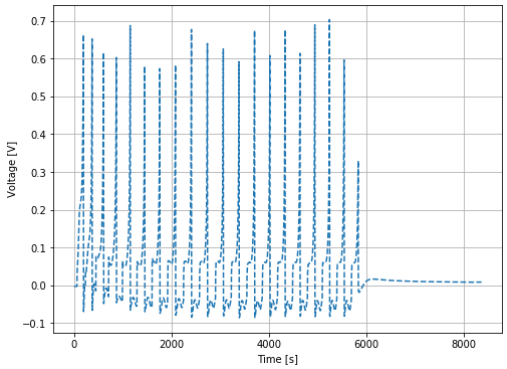

(c) Voltage error - Old

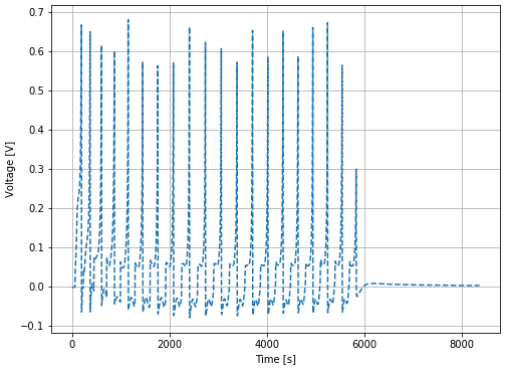

(d) Voltage error - Modified

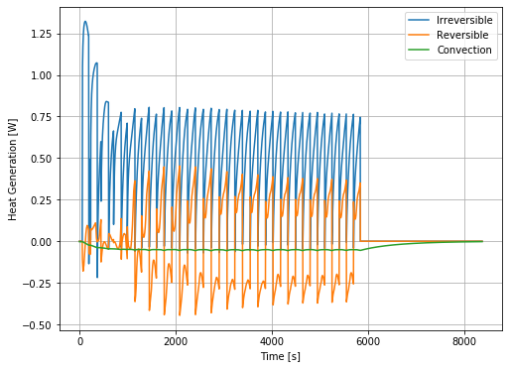

(e) Heat generation - Old

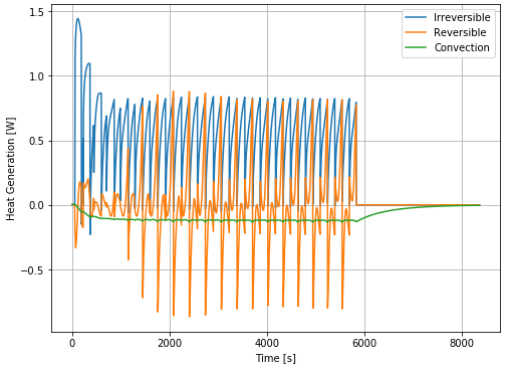

(f) Heat generation - Modified

Figure 5.14: Test 3 - 5C pulsing (Voltage Constraint) - Model comparison II

5.3.2 Test 4 - 3C pulsing (Time Constraint)

The current profile is changed to a time-based input: 3C discharge for 5 minutes followed by 3C charge for 5 minutes, as shown in figure 5.16. The current profile of the previous case was not consistent, leading to a non-periodic charge movement into/out of the LIB. To avoid sudden shock effects, as observed at the beginning of test 5, the battery is discharged at 1C rate for 40 minutes, taking it to 20% SOC.

Given the uncertainty in the heat transfer characteristics observed in the previous case, a single layer insulation of ceramic blanket (without any external weight) is used to wrap the cell.

This is a way to roughly estimate the effective heat transfer coefficient by using a steady state analysis. For the figure shown in 5.15, the equivalent heat transfer coefficient can be calculated using the following equation,

$$\frac{1}{h_{eff}} = \frac{l_{ins}}{\lambda_{ins}} + \frac{1}{h} \tag{5.5}$$

Taking $h = 7\ Wm^{-2}$ for ambient air natural convection [25], the h_{eff} value comes out to be $1.82Wm^{-2}$. Using this value, the temperature difference between the battery surface and the ambient air comes out to be 39.8°C. A more accurate answer can be obtained by treating the insulation as a semi-infinite wall. The Fourier number pertaining to this problem comes out to be $8.83 \times 10^{-4}\ t$. For times less than approximately 1140 seconds (Fourier number less than 1), the transient response of the insulation cannot be ignored. This means that the assumption of steady state conduction is erroneous. A part of the heat dissipated by the battery is being stored in the insulation at short times. For early times, one might consider an approximation like:

$$\frac{1}{h_{eff}} = \frac{\sqrt{\alpha t}}{\lambda_{ins}} \tag{5.6}$$

where α is the thermal diffusivity of the insulation.

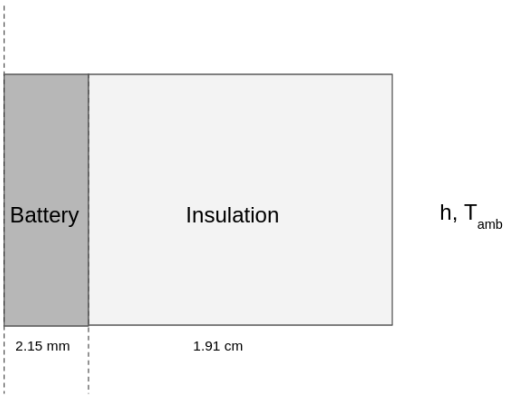

Figure 5.15: Representation of the cell-insulation arrangement

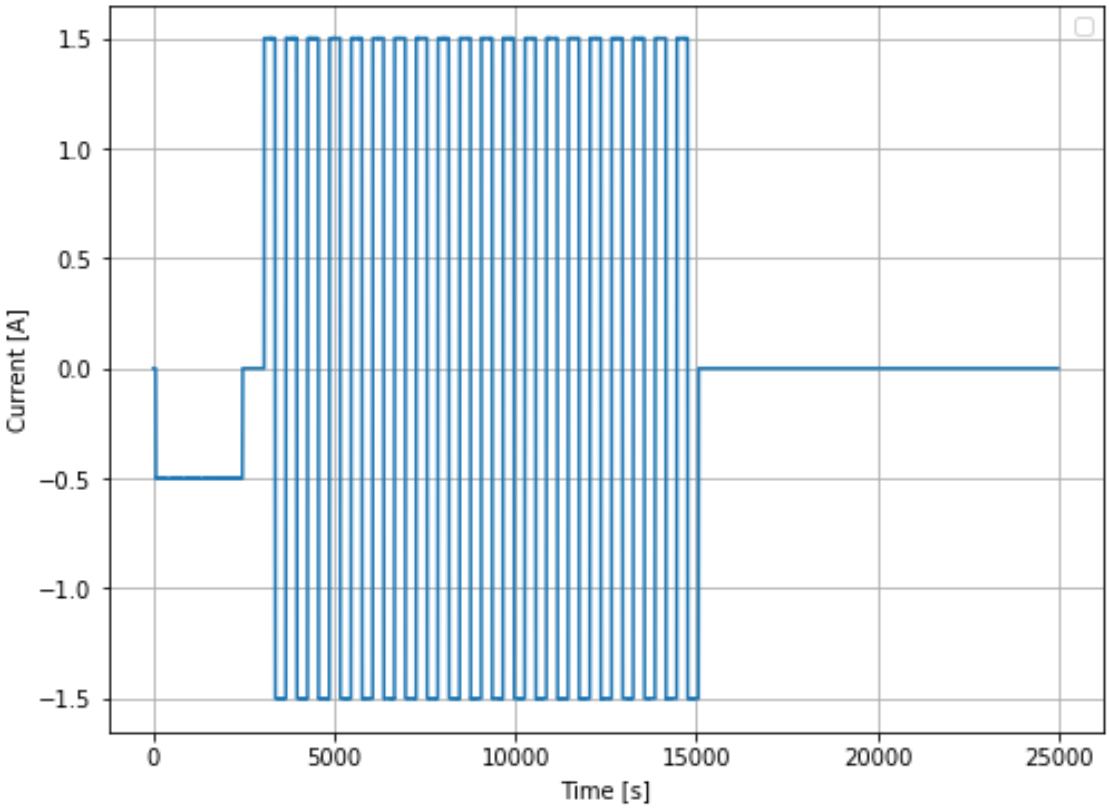

Figure 5.16: Test 4 - 3C pulsing (Time Constraint) - Current profile

Observations

Interestingly, the battery seems to be losing capacity after each cycle, as seen in figure 5.17. The voltage at the end of each discharge pulse drops initially and then becomes constant. One can see from the voltage plot that the voltage range covered by the end of the first cycle is 4.1 V to 3.15 V. As the number of cycles and temperature increase, the end-of-discharge voltage decreases, falling to 1.47 V by the end of the last cycle.

The error in voltage has decreased very slightly after the addition of the capacity fade model. The SOC plots also show how battery degradation affects the SOC range for the same current cycle at different times. The parameters of the model and the actual initial capacity need to calibrated precisely to achieve overall accuracy.

The experimental data shows that the LIB temperature rises steadily after it reaches 40°C, which is nicely captured by the modified model. As seen before, the old model reaches a steady temperature value, 45°C in this case.

The effective heat loss properties also match the experimental for this case. However, the inaccuracy of the same heat loss properties in the last test case proves the inconsistency in the setup of the adiabatic environment around the LIB.

Analysis

Based on the voltage output of the first cycle, it is safe to conclude that the battery was not being over-discharged from the beginning of the cycle. But, the continuous cycling and raised temperature led to capacity fade. Because of this degradation, the current pulse, which initially maintained the battery in normal operation range, was now over-discharging it. Another way to look at it would be to refer to the OCV-SOC relationship. As the capacity fades, the pulse profile that took the battery to, say, 5% SOC would now discharge it to -1% SOC (calculated using degraded capacity). Assuming that the OCV-SOC relationship stays the same and given its steep descent in the 0 SOC region, it can be noticed that the OCV of the degraded LIB (calculated at -1% SOC) would be much less than that of the OCV of a relatively fresh battery (calculated at 5% SOC).

As explained above, a part of these drops is a direct consequence of capacity fade. To understand another contributor to this voltage drop, one needs to consider two factors that lead to capacity fade: SEI layer formation and lithium plating at elevated charge currents. A consequence of SEI growth is decreasing anode porosity, which then leads to an increase in the internal resistance of the cell. As seen in figure 4.19, the internal resistance shoots up quite rapidly as the SOC decreases in the near 0 SOC region, which is not captured well by the model. Thus, another factor that may lead to high voltage drop during discharge is increased internal resistance loss (IR_{int}).

The thermal performance is effectively modeled by the cyclic resistance. In a way, the cyclic resistance term lumps up the effects of cell degradation, which is mainly governed by SEI growth and lithium plating. Additionally, the errors in voltage predictions do not translate to errors in temperature predictions. This interesting aspect of the model can be justified by the argument that near 0 SOC region, the

heat generation terms are relatively less sensitive to the steep gradient in OCV.

The effective heat transfer coefficient calculated overestimates the temperature difference. This can be attributed to the deviations from the ideal situation presented in the figure 5.15, like treatment of the insulation as a semi-infinite wall, contact resistance and heat loss to the surroundings form the top and the bottom of the battery. The radiation losses should also be calibrated properly.

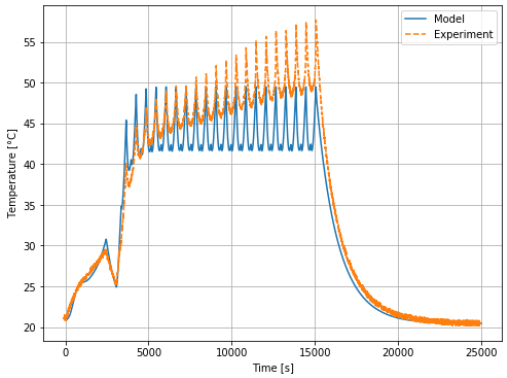

(a) Temperature - Old

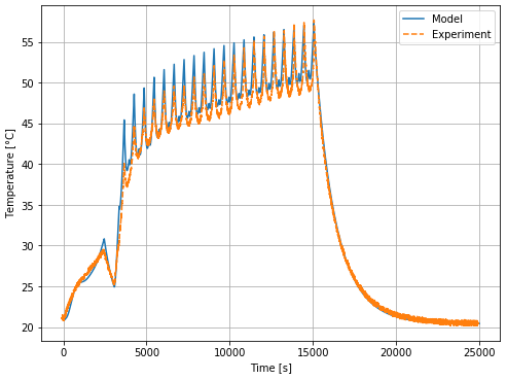

(b) Temperature - Modified

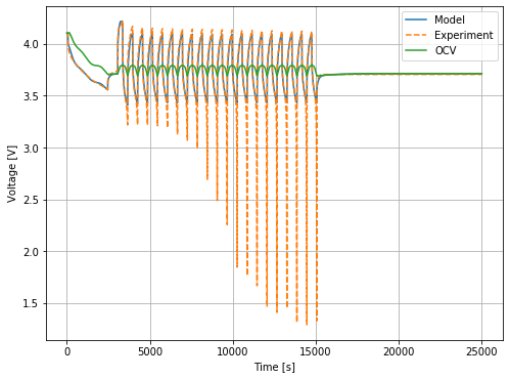

(c) Voltage - Old

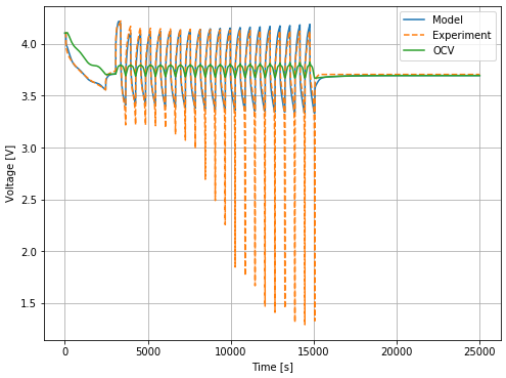

(d) Voltage - Modified

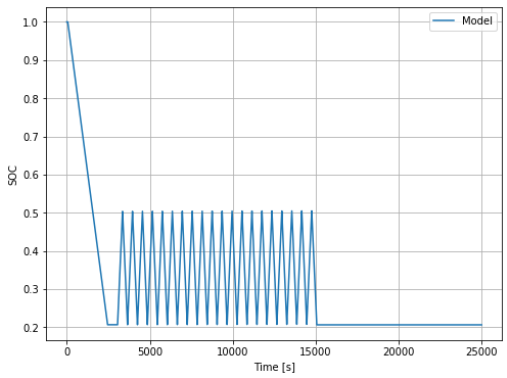

(e) SOC - Old

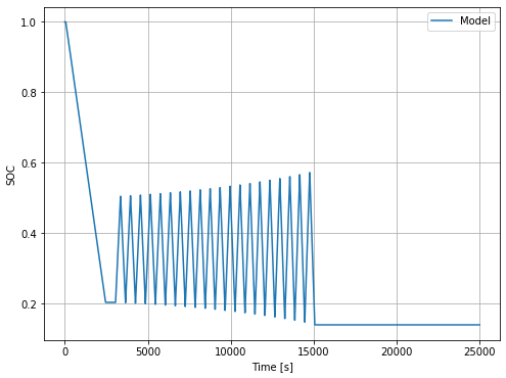

(f) SOC - Modified

Figure 5.17: Test 4 - 3C pulsing (Time Constraint) - Model comparison I

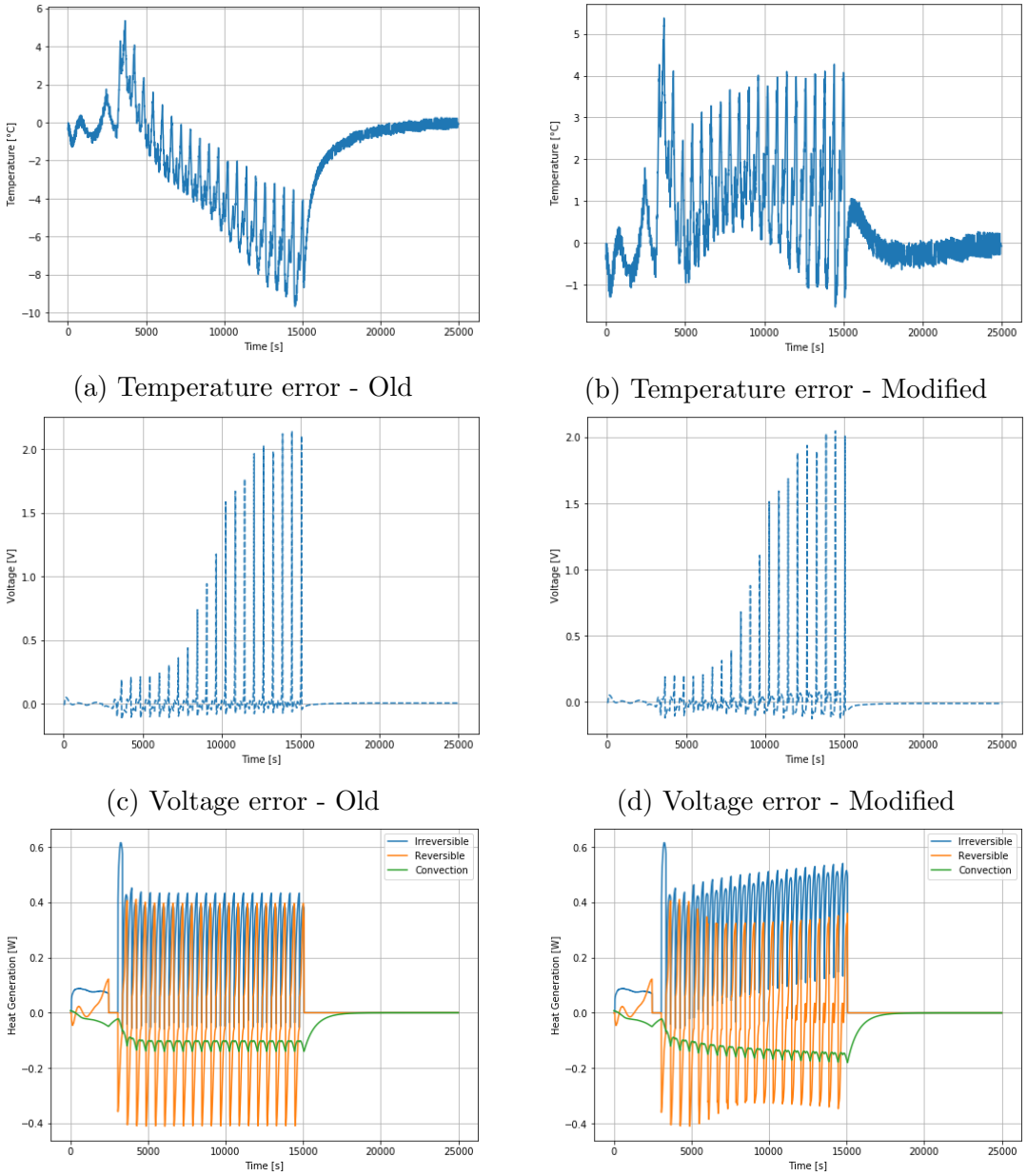

(a) Temperature error - Old

(b) Temperature error - Modified

(c) Voltage error - Old

(d) Voltage error - Modified

(e) Heat generation - Old

(f) Heat generation - Modified

Figure 5.18: Test 4 - 3C pulsing (Time Constraint) - Model comparison II

5.3.3 Test 5 - Thermal Runaway

In an attempt to prevent battery operation near 0 SOC region, a different current profile is employed, as shown in figure 5.19. The current profiles of test 3 and test 5 are identical, except that the first test has voltage constraints, and the second test has time constraints. Each cycle comprises of a 5-minute discharge at 5C followed by a 5-minute charge at the same C-rate. The failed battery is shown in figure 5.20.

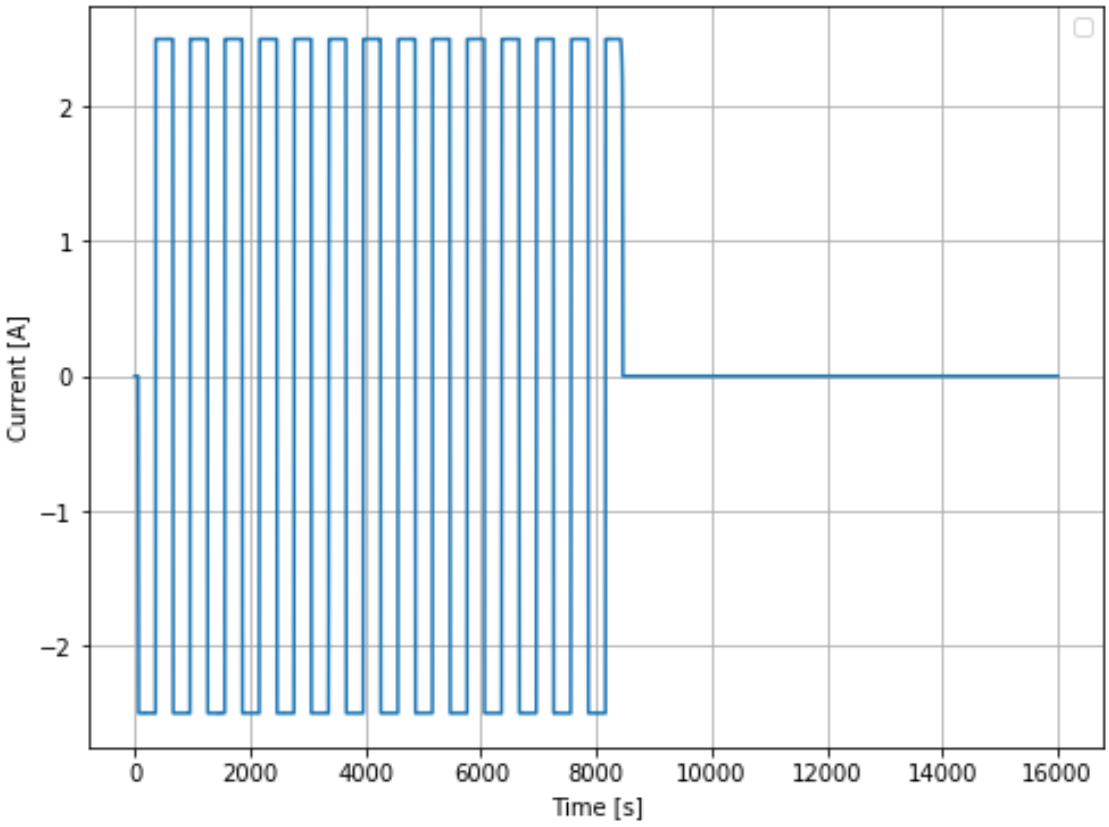

Figure 5.19: Test 5 - Thermal Runaway - Current profile

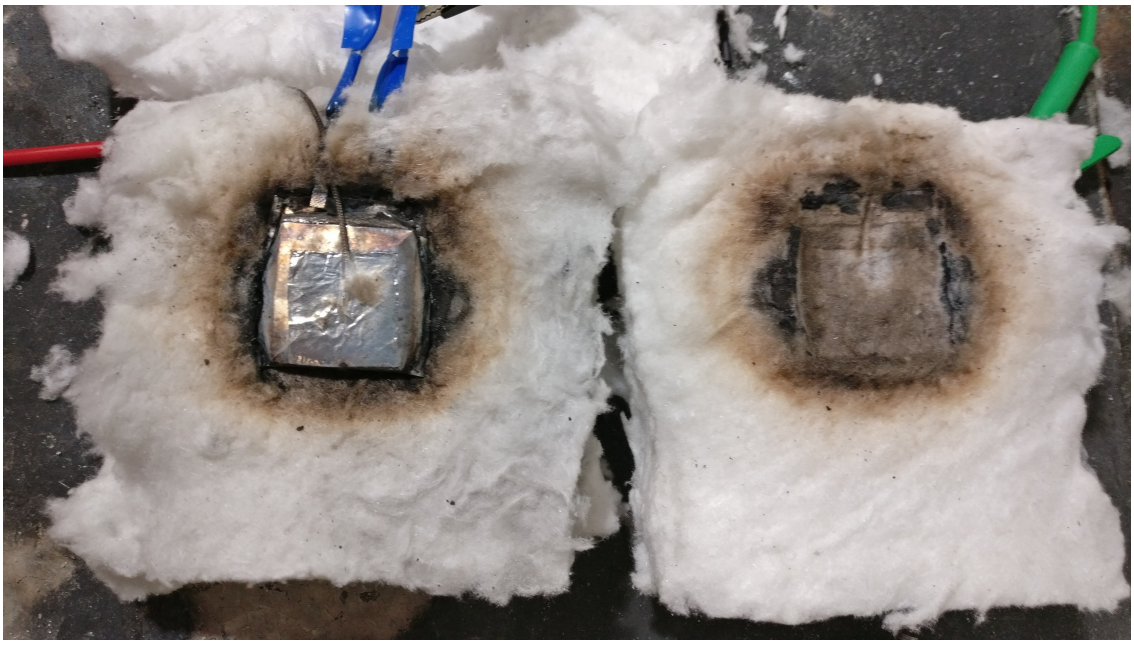

Figure 5.20: Test 5 - Thermal Runaway - Failed battery

Observation

What sets test 5 apart from the existing literature is the path of high C-rate cycling failure. Most of the research revolves around slow overcharging where LIB is charged to high voltages at low C-rates. The main difference can be observed in the way in which charges flow in and out. The current profile pushes the LIB to a peak of 4.39 V and follows it with a discharge to 3.45 V, for a major part of the operation. Interesting voltage behavior is spotted near the end of the operation. The peak value of the voltage decreases from 4.39 V to 4.37 V over the last 3 cycles, after which the voltage value blows up, leading to thermal runaway. The voltage goes from 4.5V to 6.34 V in 53 seconds. The decrease in the trough values of the voltage can be seen in figure 5.21.

The temperature values stay between 60°C and 80°C for the major portion of the operation. Due to the initial voltage response, a temperature jump is observed in the incipient stages of the cycle. At 8100 seconds, thermal runaway gets triggered. In the next 180 seconds, the temperature of the LIB shoots from 91°C to 601°C. The battery then cools through convection and radiation.

Analysis

At the beginning of the cycling itself, strange behavior is exhibited by the LIB voltage. Such a huge voltage drop is generally seen when the internal resistance of the battery is high or when the battery is in the low SOC region, however, none of the reasons explain this initial drop. The model accuracy in the subsequent cycles asserts the validity of model initialization, which in turn proves that the battery resistance and the capacity of the LIB are not causing this unexpected voltage drop.

The voltage and temperature data of the next 11 cycles agree well with the model predictions, refer figure 5.23. This level of similarity validates the fidelity of the OCV-SOC relationship and the ECM parameters at high SOCs and establishes the importance of adding accelerated ageing calculations to the model.

After 12 cycles and before thermal runaway, an increase in average temperature is observed. Based on the voltage and temperature plot, a possible pathway to failure can be hypothesized. Firstly, there is a steep drop in voltage which suggests an acceleration in capacity fade, and secondly, there is a temperature rise that indicates either the onset of side reactions like SEI decomposition or an increase in internal resistance or both. The high C-rate charging in the high SOC region leads one to believe that the internal short circuit in the battery is caused by lithium plating. The accelerated growth of dendrites at the graphite anode leads to the consumption of usable lithium in the battery, which explains the expedited capacity fade. The deposition of lithium film on the anode surface also poses as a barrier to the diffusion of electrolyte to the active reaction surface.

After 14 cycles, the kinetics of thermal runaway dominate the thermal response of the LIB, as seen in figure 5.22. As explained before in 1.4, the thermal runaway of the battery occurs in stages. SEI decomposition is observed first at around 90°C along with initial anode-electrolyte reaction. The second stage generally consists melting of separator (assuming its made of PE/PP material) which begins at around 120°C. The third stage comprises multiple processes, namely, cathode breakdown, electrolyte decomposition, and high-temperature anode-electrolyte reactions. This stage is spread over a temperature range of 200-300°C. The combined effect of all these processes gives rise to the venting of gases, swelling of LIB, and rapid increase in temperature which ultimately leads to failure of the battery.

Even after the addition of thermal runaway kinetics into the model, it is unable to mimic the experiment results. This model's inability can be attributed to the onset temperature of various runaway reactions and their kinetic parameters. The parameters given in [66] are employed and the onset temperatures of major heat-generating reactions are specified to be around 120°C. The model is unable to reach those temperatures in the first place, hence, those reactions do not get triggered. The modeling of the transition period, the last 2 cycles in the present case, needs to be understood and analyzed more thoroughly using a physics-based approach.

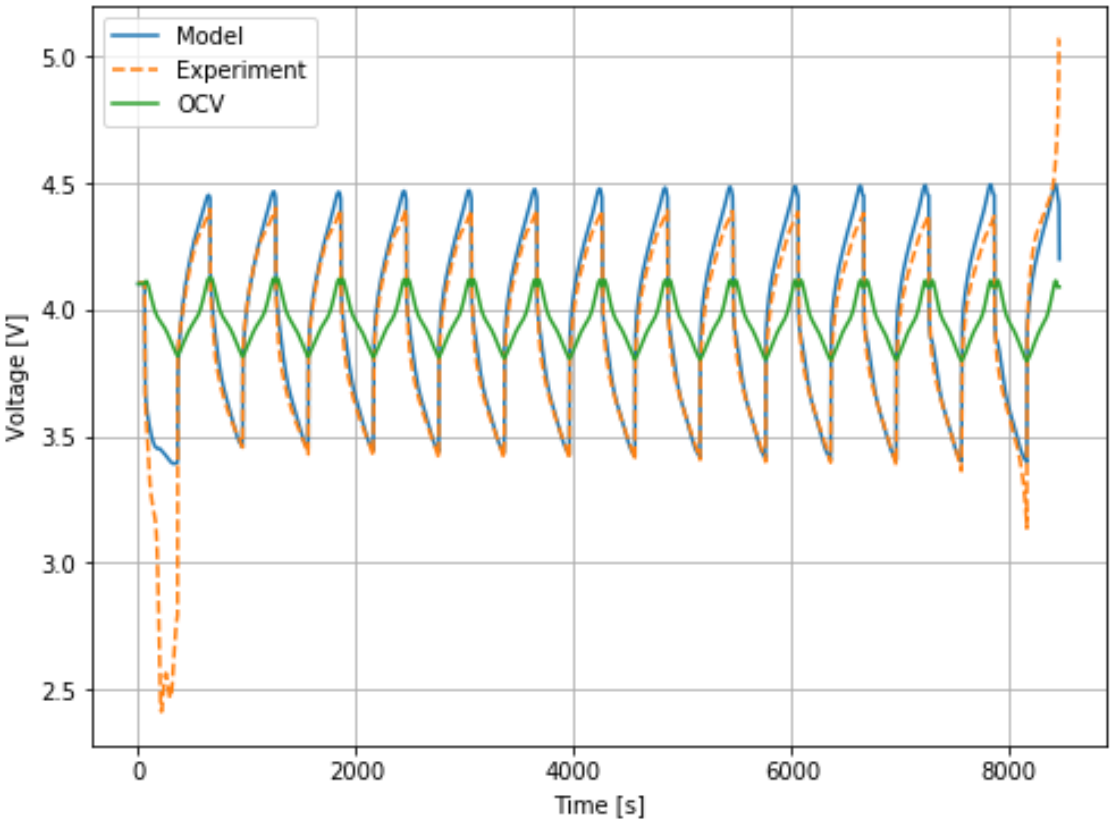

Figure 5.21: Test 5 - Thermal Runaway -Voltage

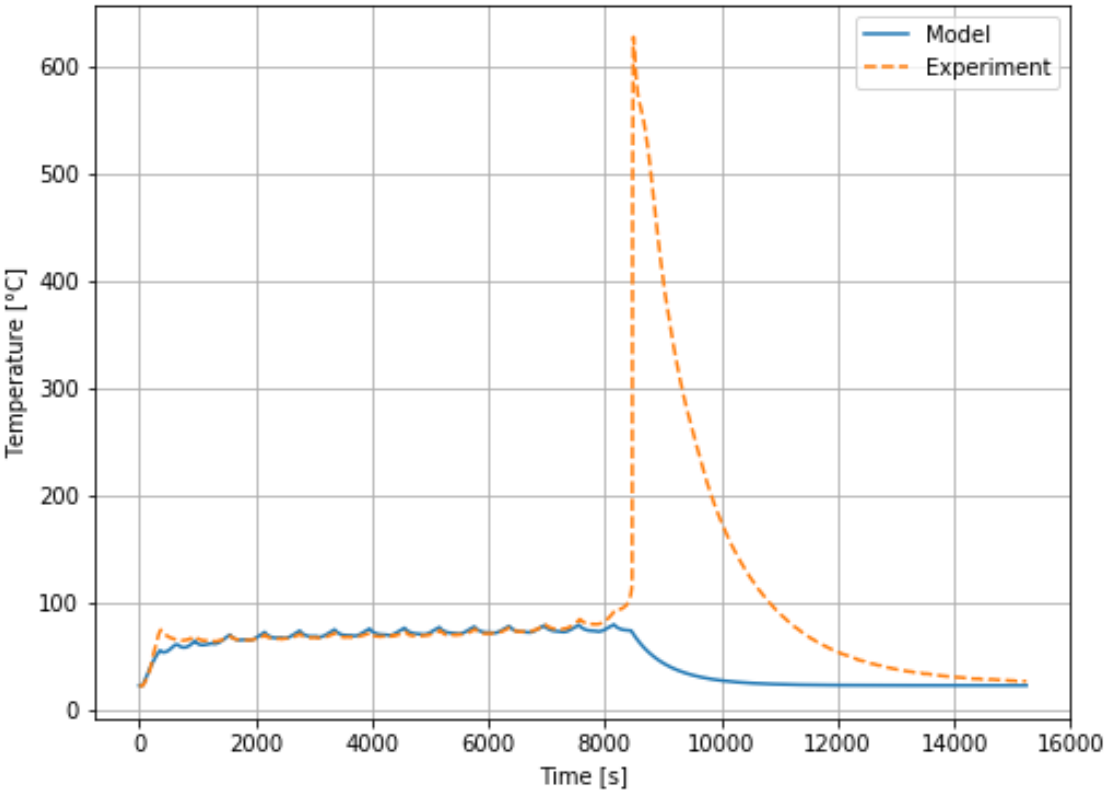

Figure 5.22: Test 5 - Thermal Runaway - Full temperature profile

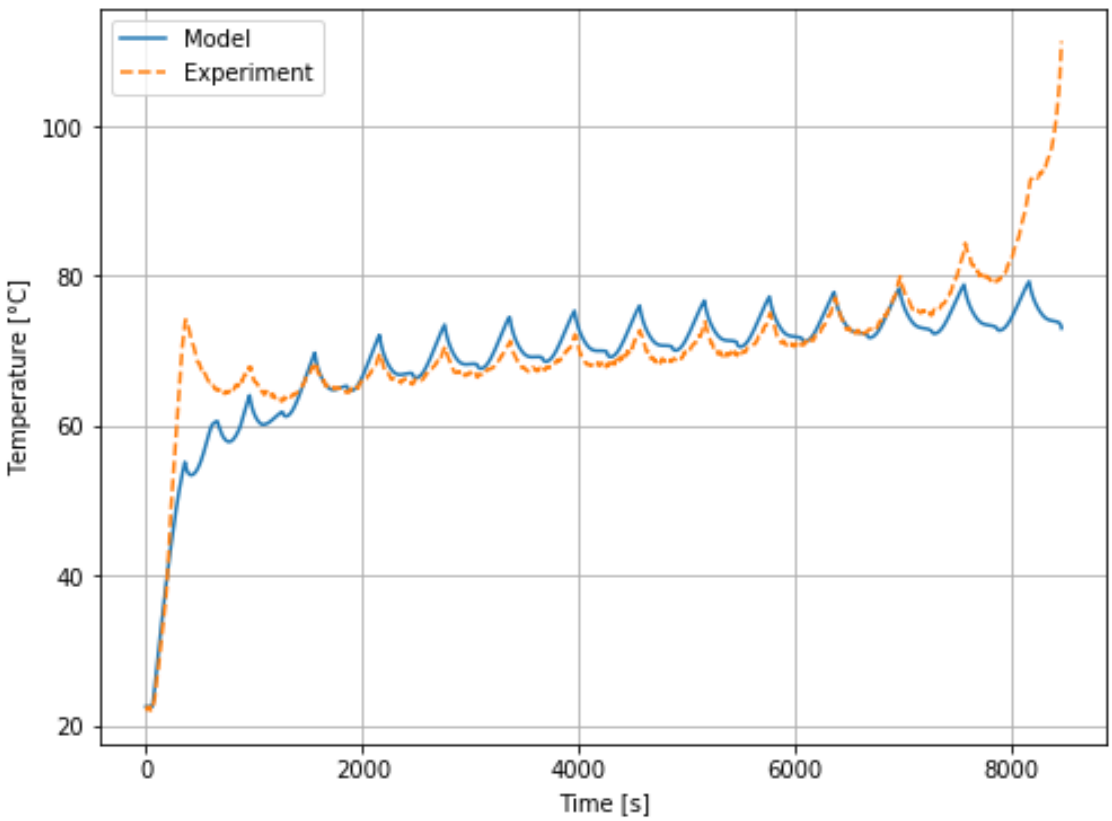

Figure 5.23: Test 5 - Thermal Runaway - Temperature profile before thermal runaway

6 Conclusions

The usefulness of lithium-ion batteries as energy storage devices is well established. The energy storage density provided by LIBs is leaps and bounds ahead of the previously used battery chemistries. However, with the advent of battery modeling techniques, researchers have realized the sheer number of parameters that affect its performance, capacity, and safety. A lot of effort has been put into understanding different charging/discharging methods, and, as a result, optimization of battery performance and usage has been accomplished to a high degree. Yet, the safety aspect of battery operation has not been properly understood. Most of the research surrounding LIB abuse is based on either experiments or empirical models that are fitted to experimental data. The gray area between LIB normal operation and abuse has not been discerned.

In the third chapter, an attempt is made to push the P2D model, which is the most fundamentally accurate model, to abuse conditions. The results show that the model is valid within a set temperature range, outside of which, the model parameters are extrapolated. The limitations of its applicability are quickly realized. To model the LIB transition to abuse conditions, the physics related to capacity fade due to different mechanisms, and the kinetics of various runaway reactions have to be included in the model. After the addition of said physics, the model complexity and a large number of input parameters decrease its usability from an application point of view. A lot of research has already been conducted for model reformulation to increase its applicability. But, the prediction of transition to LIB failure is yet to be addressed from a physics-based modeling perspective.

Since the area between normal operation and thermal abuse hasn't been explored much, a rudimentary circuit model is constructed and used in chapters four and five to predict LIB voltage and temperature response to varying current profiles under different thermal constraints. Firstly, the dependence of the model parameters on

the SOC and the temperature of the LIB is analyzed. The open-circuit voltage of the LIBs is also extracted. After that, the model is run against experimental data. The results show that the parameterized circuit model can correctly predict the temperature response of the LIB. There are errors in voltage prediction in the low SOC region. However, accurate OCV estimation and capacity measurement can potentially reduce voltage errors. A capacity fade model is also added to analyze battery response to the cyclic current input. Clear improvements are observed due to the modification of the circuit model. Yet, the model is not ready to predict the initiation of thermal runaway, owing to the inaccuracy of the model input parameters and physics implementation.

In conclusion, to model the transition to LIB abuse, all the physics relevant to normal operation and abuse conditions have to be modeled in tandem. The model is also sensitive to the ambient conditions of the battery, thus, for model validation, one has to maintain a controlled thermal environment around the battery to obtain accurate predictions. The model can be either a P2D-based model or a circuit model, as long as the parameters involved are quantified to a high degree of accuracy.

7 Future Work

For physics-based models, the number of parameters required for modeling different phenomena has to be determined accurately. Since the processes in LIB operation are coupled, it is necessary to develop a standard routine to isolate the effect of each parameter to enable its determination using a fewer number of experiments. From a big picture perspective, this will increase the model's applicability and advance easy recalibration, if needed. Also, the performance capabilities of the P2D model and the reformulated models have to be tested by simulating LIBs in harsh conditions, like high C-rate cycling and high/low temperatures, and validating the results against experimental data.

As observed from the voltage errors in ECM prediction, a more accurate determination of the open-circuit voltage of the LIB is required. Based on the capacity fade demonstrated by experimental data, the importance of using the correct initial capacity value as the input for the model is extremely important. This is justified by the model results shown in chapter four. Even a slight change in the initial capacity can lead to highly inaccurate voltage predictions in the low SOC region, owing to the sharp voltage drop in the open circuit potential. The model can also be extended to predict battery stack operation.

Overall, the path to transition portrayed in this thesis can help increase the understanding of LIB functioning in abuse conditions. As more data is collected and analyzed, improvements can be made to the sub-models that address different physical aspects of LIB operation and safety.

Appendices

A Stack Cell Test

In this chapter, the results from the stack tests are presented. The first test consists of two stacked cells that are insulated using a ceramic blanket. Similarly, the second test has the same configuration, but with three cells.

A.1 Stack of 2 cells

Experiment Setup

The setup of this experiment is the same as the one described in chapter 5.1. Two cells are placed such that one cell is on top of the other, forming a stacked sandwich. The thermocouples are placed at the outer surfaces of the sandwich. No thermocouple is placed at the interface so as to decrease the thermal resistance between the cells and maximize contact.

Due to the limitation of the Arbin instrument, the cells are not connected in series. Arbin has a maximum voltage limit of 5 V across each channel. If one were to connect the cells in series, the nominal potential difference across the cell stack would turn out to be 8 V, which is not feasible. To circumvent this restriction, two separate channels are used to cycle both the cells. Without changing the stack structure of the cell arrangement, a "series" connection is now obtained.

Both the cells are charged to 100% SOC using the same CC-CV protocol as described in section 4.1.1. The current profile used to cycle each cell is constrained in

the same way as the one shown in section 5.2.3. A total of 30 cycles are programmed into the Arbin.

Analysis

It was observed in section 5.2.3 that the voltage-constrained case gives rise to a non-uniform current profile. This case amplifies that effect. Figure A.1 juxtaposes the current and voltage profiles of both the cells. Very interesting behavior is exhibited by both the cells. Starting with the current profiles, it can be seen that cell 1 and cell 2 currents go out of phase, despite the same starting conditions of the cell. This peculiar behavior can be attributed to a possible difference in the initial capacity and/or dissimilar degradation rates of the cells. The current profiles of both the cells match when time is less than 500 seconds, however, as the cells are cycled, a phase change can be observed. At time equal to 2000 seconds, cell 1 is getting discharged whereas cell 2 is getting charged. The first cell takes up and gives out charge more quickly than the second cell for times less than 2600 seconds. This implies that the capacity of the second cell is higher than that of the first cell. After the 2500-second mark, the cells' cycling frequency shoots up. However, it should be noted that the increase in the cycling frequency of cell 2 is sharper. For cell 1, a relatively gradual increase in the cycling frequency is observed.

At this same point in time, both the cells reach a temperature of 94°C. As the cells undergo rapid cycling, the temperature steadily increases to 106.3°C, and then decreases as the cycling phase ends. The voltage profiles follow the same trend as the current profiles, cycling between 4.2 V and 2.75 V.

It is fair to conclude that, at 2600 seconds, the cells undergo an accelerated degradation process. Going by the onset temperature values provided by Feng [66], by the time the cells reach 100°C, the SEI decomposition-regeneration process and anode-electrolyte reaction should have already started degrading the cell. It is possible that the level of cell degradation reached by 2600 seconds gets to a point where the capacity of the battery suddenly plummets. Given such harsh operating conditions, it is not illogical to expect thermal runaway, however, the degradation does

not seem to be high enough to cause an internal short circuit in the cells. More tests are needed to isolate the source of this behavior.

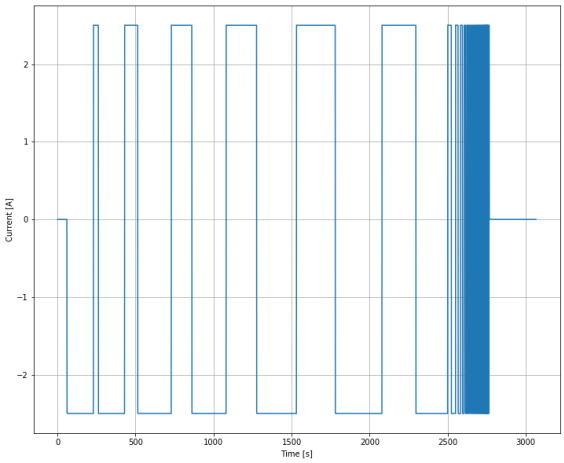

(a) Cell 1 - Current profile

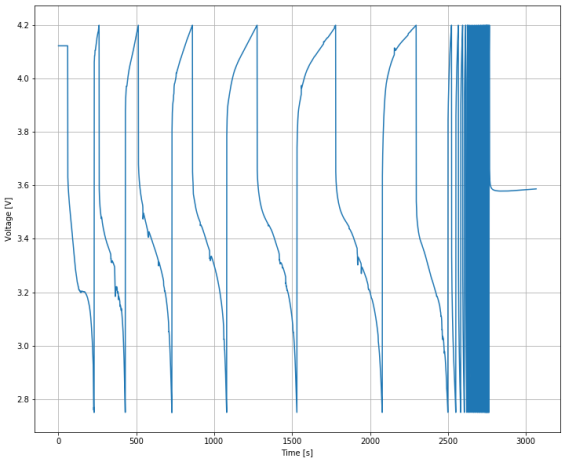

(b) Cell 1 - Voltage profile

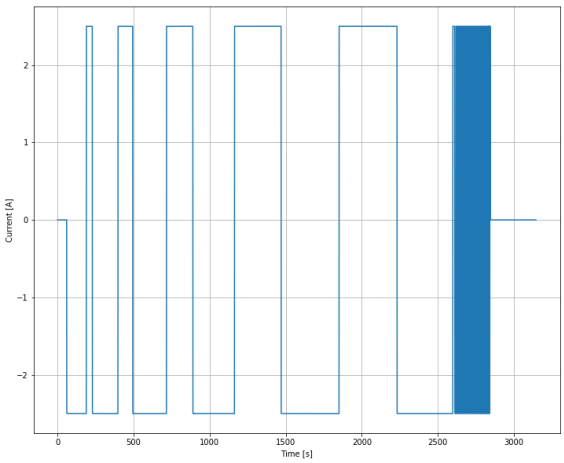

(c) Cell 2 - Current profile

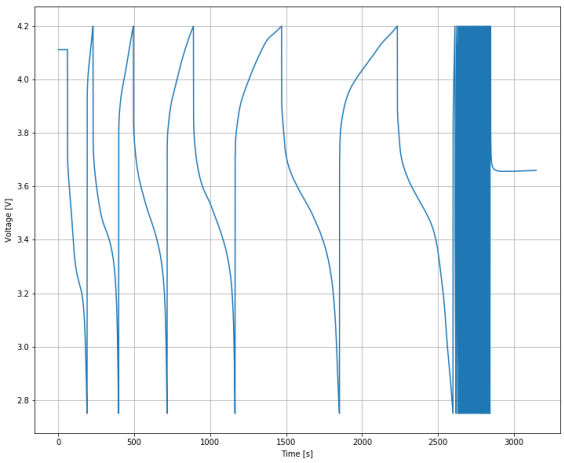

(d) Cell 2 - Voltage profile

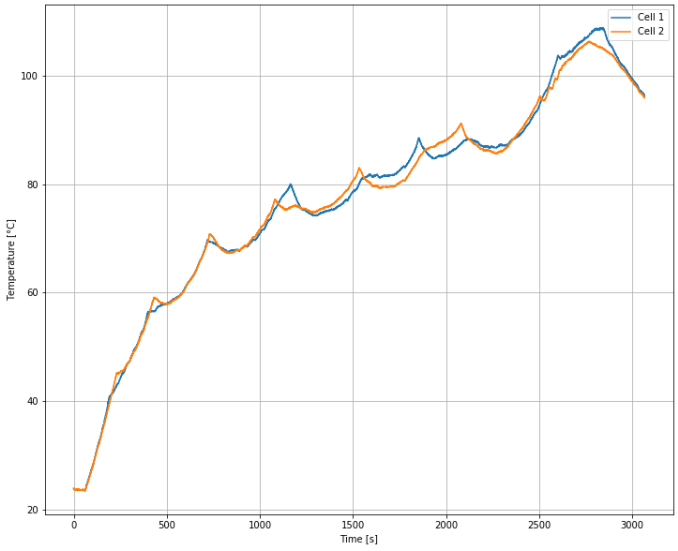

(e) Cell stack surfaces - Temperature profiles

Figure A.1: Stack of 2 cells

A.2 Stack of 3 cells

Experiment Setup

The setup used in this test is the same as the one used in the previous test. The only change here is the addition of the third cell. The thermocouples are now attached to the exposed surface of the first cell and the third cell. The second cell is sandwiched between the edge cells. Each cell is cycled 30 times using different Arbin channels.

Analysis

Figure A.2 shows the current and voltage profiles of all the cells. Cell 2 is the one that is sandwiched between cell 1 and cell 2. The general trend of the current and voltage profile is the same as that shown in the previous case. The cell in the middle takes the longest time to complete 30 cycles, and the rest of the cells complete their cycling processes at the same time. Based on what was seen in the last case, the variation of the cycling frequency in all cells is expected. The most interesting observation of this test is the response of cell 2. The fact that it ended after cell 1 and cell 3 shows that the degradation rate of cell 2 is relatively lower. Again, the difference in the initial capacity plays a crucial role in its long term behavior.

The asynchronous peaks observed in the temperature profiles, shown in figure A.3, can be attributed to the out of phase current profiles of cells 1 and 3. This time, the peak temperature value comes out to be 110.5 °C, which is near the last case's peak value. Information about the temperature of cell 2 is needed to determine the flow of heat across the cells. It is possible that the decelerated response of cell 2 is caused by its thermal behavior. However, this is just a speculation, and more tests with efficient thermocouple placements are needed to study the stack effect properly.

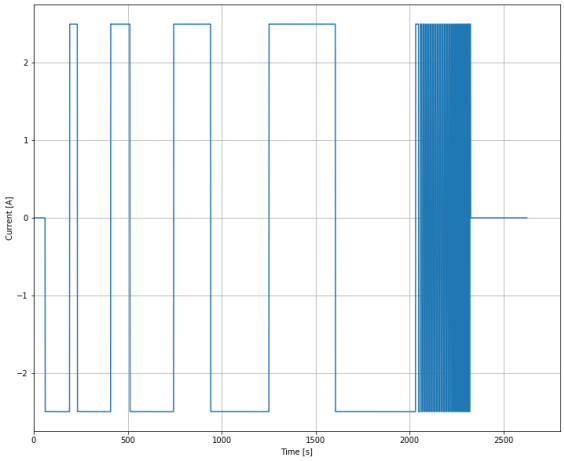

(a) Cell 1 - Current profile

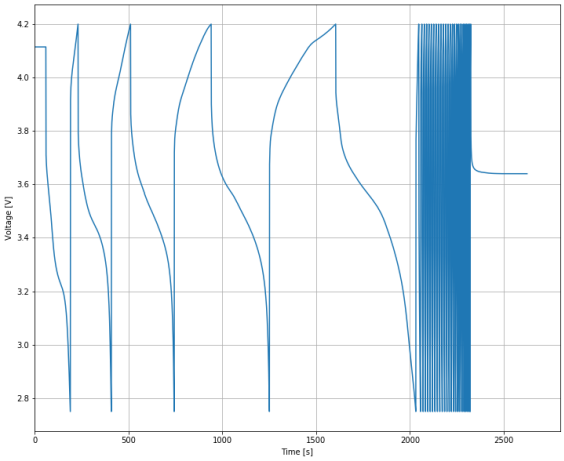

(b) Cell 1 - Voltage profile

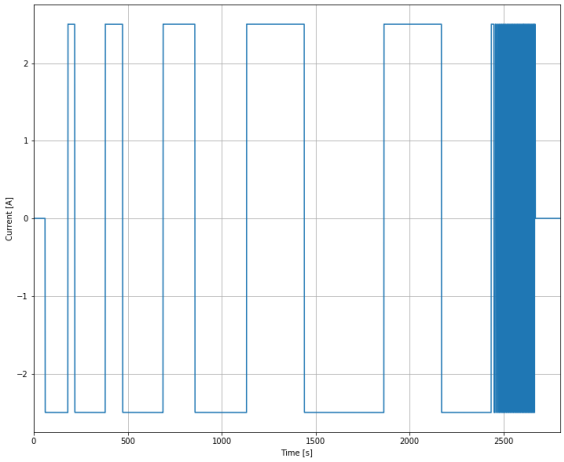

(c) Cell 2 - Current profile

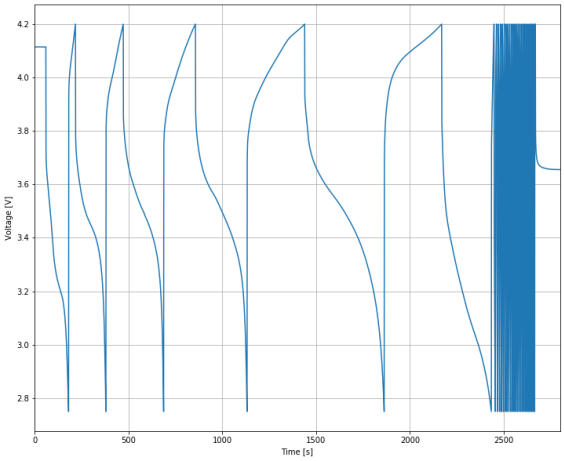

(d) Cell 2 - Voltage profile

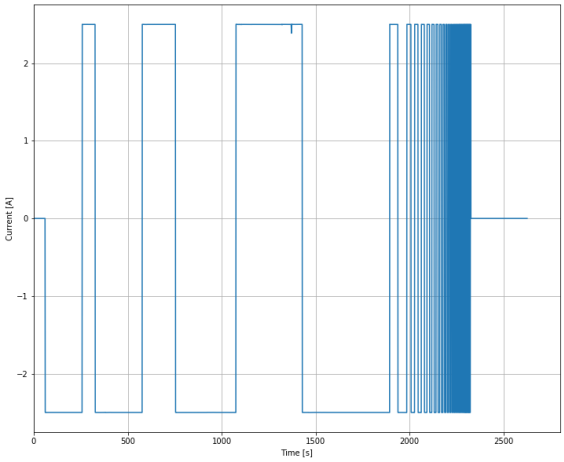

(e) Cell 3 - Current profile

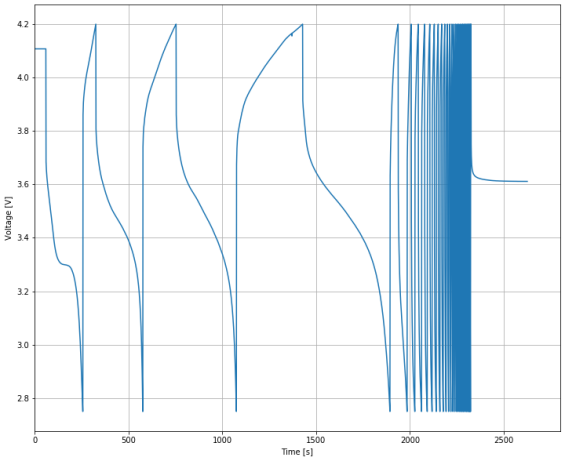

(f) Cell 3 - Voltage profile

Figure A.2: Stack of 3 cells - Current and voltage

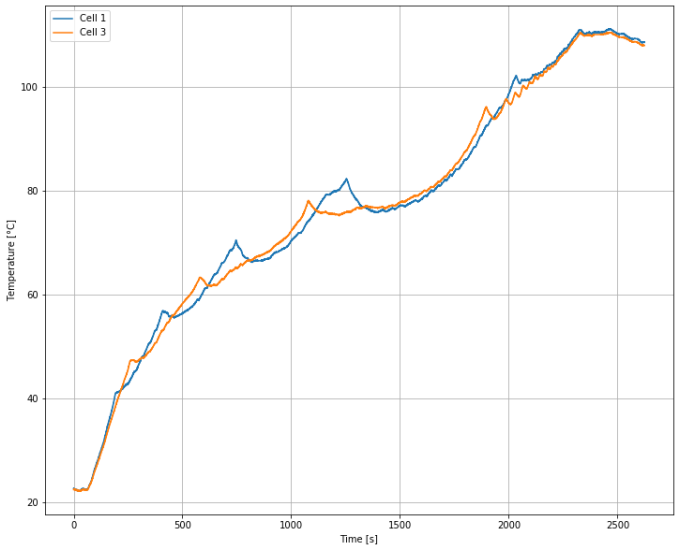

(a) Cell stack surfaces - Temperature Profiles

Figure A.3: Stack of 3 cells - Temperature

B P2D simplifications

For faster simulation, the P2D model is generally reformulated. Two very popular models are the single particle model (SPM) and the parabolic profile model (PP).

B.1 Single Particle Model

In this model, the spatial dependence of the variables of interest is eliminated and each electrode is treated as a model sphere. Some salient features of the model are:

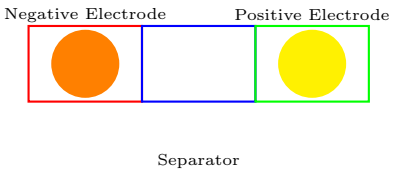

Figure B.1: SPM Model

- Solve ODEs of: C_s, T (**No** C_e, ϕ_s and ϕ_e)
- Simple with minimum computational effort
- Useful for normal operation and life modeling
- Drawbacks:
    - Needs to be finely-tuned according to electrolyte properties and cell thickness
    - Inaccurate for high discharge rates

B.2 Parabolic Profile Model

The way PP model modifies the P2D model is through the volume-averaging of solid concentration. Instead of using finite difference to model solid diffusion at each node in x-grid, the PP model uses an analytical approximation of the solid concentration profile in each sphere. Some characteristics of the PP model are:

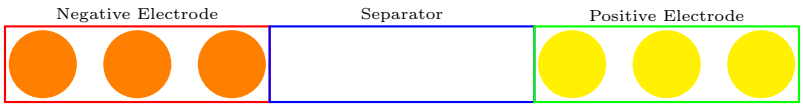

Figure B.2: PP Model

- Solve ODEs of: C_s, C_e, ϕ_s, ϕ_e, T
- Parabolic approximation used to solve C_s diffusion equation

$$C_s(r,t) = a(t) + b(t) * (r/R)^2 \tag{B.1}$$

- $a(t)$ and $b(t)$ can be obtained by substituting (B.1) in C_s diffusion equation
- Drawbacks:
    - Inaccurate for pulse loads
    - Higher order approximations needed for high discharge rate

References

[1] Noshin Omar et al. “Lithium iron phosphate based battery – Assessment of the aging parameters and development of cycle life model”. In: *Applied Energy* 113.C (2014), pp. 1575–1585. DOI: 10.1016/j.apenergy.2013.0. URL: https://ideas.repec.org/a/eee/appene/v113y2014icp1575-1585.html.

[2] Xingtao Liu et al. “A novel temperature-compensated model for power Li-ion batteries with dual-particle-filter state of charge estimation”. In: *Applied Energy* 123 (2014), pp. 263 –272. ISSN: 0306-2619. DOI: https://doi.org/10.1016/j.apenergy.2014.02.072. URL: http://www.sciencedirect.com/science/article/pii/S0306261914002177.

[3] Humberto Joachin et al. “Electrochemical and Thermal Studies of LiFePO4 Cathode in Lithium-Ion Cells”. In: *ECS Transactions*. ECS, 2008. DOI: 10.1149/1.2943220. URL: https://doi.org/10.1149%2F1.2943220.

[4] Xuesong Li, Fan He, and Lin Ma. “Thermal management of cylindrical batteries investigated using wind tunnel testing and computational fluid dynamics simulation”. In: *Journal of Power Sources* 238 (2013), pp. 395 –402. ISSN: 0378-7753. DOI: https://doi.org/10.1016/j.jpowsour.2013.04.073. URL: http://www.sciencedirect.com/science/article/pii/S037877531300671X.

[5] Wladislaw Waag, Stefan Käbitz, and Dirk Uwe Sauer. “Experimental investigation of the lithium-ion battery impedance characteristic at various conditions and aging states and its influence on the application”. In: *Applied Energy* 102 (2013). Special Issue on Advances in sustainable biofuel production and use - XIX International Symposium on Alcohol Fuels - ISAF, pp. 885 –897. ISSN: 0306-2619. DOI: https://doi.org/10.1016/j.apenergy.2012.09.030. URL: http://www.sciencedirect.com/science/article/pii/S030626191200671X.

[6] Zhonghao Rao and Shuangfeng Wang. “A review of power battery thermal energy management”. In: *Renewable and Sustainable Energy Reviews* 15.9 (2011), pp. 4554 –4571. ISSN: 1364-0321. DOI: https://doi.org/10.1016/j.rser.2011.07.096. URL: http://www.sciencedirect.com/science/article/pii/S1364032111003418.

[7] Can-Yong Jhu et al. “Thermal runaway potential of LiCoO2 and Li(Ni1/3Co1/3Mn1/3)O2 batteries determined with adiabatic calorimetry methodology”. In: *Applied Energy* 100 (2012). Clean Energy for Future Generations, pp. 127 –131. ISSN: 0306-2619. DOI: https://doi.org/10.1016/j.apenergy.2012.05.064. URL: http://www.sciencedirect.com/science/article/pii/S0306261912004655.

[8] Venkat Subramanian, Vinten Diwakar, and Deepak Tapriyal. “Efficient Macro-Micro Scale Coupled Modeling of Batteries”. In: *Journal of The Electrochemical Society - J ELECTROCHEM SOC* 152 (Jan. 2005). DOI: 10.1149/1.2032427.

[9] Bruno Scrosati and Jürgen Garche. “Lithium batteries: Status, prospects and future”. In: *Journal of Power Sources* 195.9 (2010), pp. 2419 –2430. ISSN: 0378-7753. DOI: https://doi.org/10.1016/j.jpowsour.2009.11.048. URL: http://www.sciencedirect.com/science/article/pii/S0378775309020564.

[10] Jiantie Xu et al. “Recent Progress in Graphite Intercalation Compounds for Rechargeable Metal (Li, Na, K, Al)-Ion Batteries”. In: *Advanced Science* 4.10 (2017), p. 1700146. DOI: 10.1002/advs.201700146.

[11] Reza Younesi et al. “Lithium Salts for Advanced Lithium Batteries: Li-metal, Li-O2, and Li-S”. In: *Energy Environ. Sci.* 8 (June 2015), pp. 1905–1922. DOI: 10.1039/C5EE01215E.

[12] PeterG. Bruce, Bruno Scrosati, and Jean-Marie Tarascon. “Nanomaterials for Rechargeable Lithium Batteries”. In: *Angewandte Chemie International Edition* 47.16 (2008), pp. 2930–2946. DOI: 10.1002/anie.200702505. eprint: https://onlinelibrary.wiley.com/doi/pdf/10.1002/anie.200702505.

URL: https://onlinelibrary.wiley.com/doi/abs/10.1002/anie.200702505.

[13] Heide Budde-Meiwes et al. "A review of current automotive battery technology and future prospects". In: *Proceedings of the Institution of Mechanical Engineers, Part D: Journal of Automobile Engineering* 227 (May 2013), pp. 761–776. DOI: 10.1177/0954407013485567.

[14] *Designing Applications with Lithium-Ion Batteries*. https://www.richtek.com/Design\%20Support/Technical\%20Document/AN025. Accessed: 2020-04-20.

[15] *Pouch Cell - Small but not Trouble Free*. https://batteryuniversity.com/learn/archive/pouch_cell_small_but_not_trouble_free. Accessed: 2020-04-20.

[16] Marc Doyle, Thomas F Fuller, and John Newman. "Modeling of galvanostatic charge and discharge of the lithium/polymer/insertion cell". In: *Journal of the Electrochemical society* 140.6 (1993), p. 1526.

[17] Thomas F. Fuller. "Simulation and Optimization of the Dual Lithium Ion Insertion Cell". In: *Journal of The Electrochemical Society* 141.1 (1994), p. 1. DOI: 10.1149/1.2054684. URL: https://doi.org/10.1149%2F1.2054684.

[18] Ali Jokar et al. "Review of simplified Pseudo-two-Dimensional models of lithium-ion batteries". In: *Journal of Power Sources* 327 (Sept. 2016), pp. 44–55. DOI: 10.1016/j.jpowsour.2016.07.036.

[19] John Newman. "Thermoelectric effects in electrochemical systems". In: *Industrial & Engineering Chemistry Research* 34.10 (1995), pp. 3208–3216. DOI: 10.1021/ie00037a005. eprint: https://doi.org/10.1021/ie00037a005. URL: https://doi.org/10.1021/ie00037a005.

[20] Marcello Torchio et al. "LIONSIMBA: A Matlab Framework Based on a Finite Volume Model Suitable for Li-Ion Battery Design, Simulation, and Control". In: *Journal of The Electrochemical Society* 163 (Apr. 2016), A1192–A1205. DOI: 10.1149/2.0291607jes.

[21] Zhoujian An et al. “Investigation on lithium-ion battery electrochemical and thermal characteristic based on electrochemical-thermal coupled model”. In: *Applied Thermal Engineering* 137 (2018), pp. 792 –807. ISSN: 1359-4311. DOI: https://doi.org/10.1016/j.applthermaleng.2018.04.014. URL: http://www.sciencedirect.com/science/article/pii/S1359431118309840.

[22] Sandip Mazumder and Jiheng Lu. “Faster-Than-Real-Time Simulation of Lithium Ion Batteries with Full Spatial and Temporal Resolution”. In: *International Journal of Electrochemistry* 2013 (Dec. 2013), pp. 1–10. DOI: 10.1155/2013/268747.

[23] Yanqing Lai et al. “Insight into heat generation of lithium ion batteries based on the electrochemical-thermal model at high discharge rates”. In: *International Journal of Hydrogen Energy* 40.38 (2015), pp. 13039 –13049. ISSN: 0360-3199. DOI: https://doi.org/10.1016/j.ijhydene.2015.07.079. URL: http://www.sciencedirect.com/science/article/pii/S0360319915018522.

[24] P. Razelos and E. Georgiou. “Two-Dimensional Effects and Design Criteria for Convective Extended Surfaces”. In: *Heat Transfer Engineering* 13.3 (1992), pp. 38–48. DOI: 10.1080/01457639208939780. eprint: https://doi.org/10.1080/01457639208939780. URL: https://doi.org/10.1080/01457639208939780.

[25] T.L. Bergman et al. *Fundamentals of Heat and Mass Transfer*. Wiley, 2011. ISBN: 9780470501979. URL: https://books.google.com/books?id=vvyIoXEywMoC.

[26] P Ramadass et al. “Development of First Principles Capacity Fade Model for Li-Ion Cells”. In: *Journal of The Electrochemical Society* 151 (Feb. 2004). DOI: 10.1149/1.1634273.

[27] Harry Ploehn, Premanand Ramadass, and Ralph White. “Solvent Diffusion Model for Aging of Lithium-Ion Battery Cells”. In: *Journal of The Electrochemical Society* 151 (Mar. 2004), A456–A462. DOI: 10.1149/1.1644601.

[28] Matthew B. Pinson and Martin Z. Bazant. “Theory of SEI Formation in Rechargeable Batteries: Capacity Fade, Accelerated Aging and Lifetime Prediction”. In: 2012.

[29] Xiao-Guang Yang et al. “Modeling of lithium plating induced aging of lithium-ion batteries: Transition from linear to nonlinear aging”. In: *Journal of Power Sources* 360 (2017), pp. 28 –40. ISSN: 0378-7753. DOI: https://doi.org/10.1016/j.jpowsour.2017.05.110. URL: http://www.sciencedirect.com/science/article/pii/S0378775317307619.

[30] Thomas Waldmann, Björn-Ingo Hogg, and Margret Wohlfahrt-Mehrens. “Li plating as unwanted side reaction in commercial Li-ion cells – A review”. In: *Journal of Power Sources* 384 (2018), pp. 107 –124. ISSN: 0378-7753. DOI: https://doi.org/10.1016/j.jpowsour.2018.02.063. URL: http://www.sciencedirect.com/science/article/pii/S0378775318301848.

[31] Hyung-Joo Noh et al. “Comparison of the structural and electrochemical properties of layered Li[NixCoyMnz]O2 (x = 1/3, 0.5, 0.6, 0.7, 0.8 and 0.85) cathode material for lithium-ion batteries”. In: *Journal of Power Sources* 233 (2013), pp. 121 –130. ISSN: 0378-7753. DOI: https://doi.org/10.1016/j.jpowsour.2013.01.063. URL: http://www.sciencedirect.com/science/article/pii/S0378775313001110.

[32] “A Review on Lithium-Ion Batteries Safety Issues: Existing Problems and Possible Solutions”. In: *Materials Express* 2.3 (2012).

[33] Qingsong Wang et al. “A review of lithium ion battery failure mechanisms and fire prevention strategies”. In: *Progress in Energy and Combustion Science* 73 (2019), pp. 95 –131. ISSN: 0360-1285. DOI: https://doi.org/10.1016/j.pecs.2019.03.002. URL: http://www.sciencedirect.com/science/article/pii/S0360128518301801.

[34] Hossein Maleki and Jason N. Howard. “Internal short circuit in Li-ion cells”. In: *Journal of Power Sources* 191.2 (2009), pp. 568 –574. ISSN: 0378-7753. DOI: https://doi.org/10.1016/j.jpowsour.2009.02.070. URL: http://www.sciencedirect.com/science/article/pii/S0378775309004224.

[35] Elham Sahraei, John Campbell, and Tomasz Wierzbicki. “Modeling and short circuit detection of 18650 Li-ion cells under mechanical abuse conditions”. In: *Journal of Power Sources* 220 (2012), pp. 360 –372. ISSN: 0378-7753. DOI:

https://doi.org/10.1016/j.jpowsour.2012.07.057. URL: http://www.sciencedirect.com/science/article/pii/S0378775312011822.

[36] K.H. Shim et al. "Investigation on blanking of thin sheet metal using the ductile fracture criterion and its experimental verification". In: *Journal of Materials Processing Technology* 155-156 (2004). Proceedings of the International Conference on Advances in Materials and Processing Technologies: Part 2, pp. 1935 –1942. ISSN: 0924-0136. DOI: https://doi.org/10.1016/j.jmatprotec.2004.04.284. URL: http://www.sciencedirect.com/science/article/pii/S0924013604006983.

[37] R. Spotnitz and J. Franklin. "Abuse behavior of high-power, lithium-ion cells". In: *Journal of Power Sources* 113.1 (2003), pp. 81 –100. ISSN: 0378-7753. DOI: https://doi.org/10.1016/S0378-7753(02)00488-3. URL: http://www.sciencedirect.com/science/article/pii/S0378775302004883.

[38] Xuning Feng et al. "Thermal runaway mechanism of lithium ion battery for electric vehicles: A review". In: *Energy Storage Materials* 10 (2018), pp. 246 –267. ISSN: 2405-8297. DOI: https://doi.org/10.1016/j.ensm.2017.05.013. URL: http://www.sciencedirect.com/science/article/pii/S2405829716303464.

[39] Yaoming Deng et al. "From the charge conditions and internal short-circuit strategy to analyze and improve the overcharge safety of LiCoO2/graphite batteries". In: *Electrochimica Acta* 282 (2018), pp. 295 –303. ISSN: 0013-4686. DOI: https://doi.org/10.1016/j.electacta.2018.06.081. URL: http://www.sciencedirect.com/science/article/pii/S0013468618313690.

[40] Salim Erol, Mark E. Orazem, and Richard P. Muller. "Influence of overcharge and over-discharge on the impedance response of LiCoO2—C batteries". In: *Journal of Power Sources* 270 (2014), pp. 92 –100. ISSN: 0378-7753. DOI: https://doi.org/10.1016/j.jpowsour.2014.07.038. URL: http://www.sciencedirect.com/science/article/pii/S0378775314010829.

[41] Perrine Ribière et al. "Investigation on the fire-induced hazards of Li-ion battery cells by fire calorimetry". In: *Energy Environ. Sci.* 5 (Jan. 2012), pp. 5271–5280. DOI: 10.1039/C1EE02218K.

[42] Daniel H Doughty. *Vehicle battery safety roadmap guidance*. Tech. rep. National Renewable Energy Lab.(NREL), Golden, CO (United States), 2012.

[43] Tetsuya Kawamura et al. "Thermal stability of alkyl carbonate mixed-solvent electrolytes for lithium ion cells". In: *Journal of Power Sources* 104.2 (2002), pp. 260 –264. ISSN: 0378-7753. DOI: https://doi.org/10.1016/S0378-7753(01)00960-0. URL: http://www.sciencedirect.com/science/article/pii/S0378775301009600.

[44] Dong Zhang, Branko N. Popov, and Ralph E. White. "Modeling Lithium Intercalation of a Single Spinel Particle under Potentiodynamic Control". In: *Journal of The Electrochemical Society* 147.3 (2000), p. 831. DOI: 10.1149/1.1393279. URL: https://doi.org/10.1149%2F1.1393279.

[45] Venkatasailanathan Ramadesigan et al. "Modeling and Simulation of Lithium-Ion Batteries from a Systems Engineering Perspective". In: *Journal of The Electrochemical Society* 159 (Jan. 2012), R31–R45. DOI: 10.1149/2.018203jes.

[46] David M. Young. "Chapter 18 - SELECTION OF ITERATIVE METHOD". In: *Iterative Solution of Large Linear Systems*. Ed. by David M. Young. Academic Press, 1971, pp. 553 –555. ISBN: 978-0-12-773050-9. DOI: https://doi.org/10.1016/B978-0-12-773050-9.50026-7. URL: http://www.sciencedirect.com/science/article/pii/B9780127730509500267.

[47] J. Crank and P. Nicolson. "A practical method for numerical evaluation of solutions of partial differential equations of the heat-conduction type". In: *Mathematical Proceedings of the Cambridge Philosophical Society* 43.1 (1947), 50–67. DOI: 10.1017/S0305004100023197.

[48] C. T. Kelley. *Iterative Methods for Linear and Nonlinear Equations*. Society for Industrial and Applied Mathematics, 1995. DOI: 10.1137/1.9781611970944. eprint: https://epubs.siam.org/doi/pdf/10.1137/1.9781611970944. URL: https://epubs.siam.org/doi/abs/10.1137/1.9781611970944.

[49] Alexander Farmann and Dirk Uwe Sauer. "A comprehensive review of on-board State-of-Available-Power prediction techniques for lithium-ion batteries in electric vehicles". In: *Journal of Power Sources* 329 (2016), pp. 123 –137. ISSN: 0378-7753. DOI: https://doi.org/10.1016/j.jpowsour.2016.

08.031. URL: http://www.sciencedirect.com/science/article/pii/S0378775316310308.

[50] Alexander Farmann and Dirk Uwe Sauer. "Comparative study of reduced order equivalent circuit models for on-board state-of-available-power prediction of lithium-ion batteries in electric vehicles". In: *Applied Energy* 225 (2018), pp. 1102 –1122. ISSN: 0306-2619. DOI: https://doi.org/10.1016/j.apenergy.2018.05.066. URL: http://www.sciencedirect.com/science/article/pii/S0306261918307761.

[51] Shahab Nejad. "A systematic review of lumped-parameter equivalent circuit models for real-time estimation of lithium-ion battery states". In: *Journal of Power Sources* 316 (June 2016), pp. 183–196. DOI: 10.1016/j.jpowsour.2016.03.042.

[52] J. E. B. Randles. "Kinetics of rapid electrode reactions". In: *Discuss. Faraday Soc.* 1 (0 1947), pp. 11–19. DOI: 10.1039/DF9470100011. URL: http://dx.doi.org/10.1039/DF9470100011.

[53] Rudy Tjandra et al. "Improved Lithium-Ion Battery Model with Hysteresis Effect". In: June 2014. DOI: 10.1109/ITEC.2014.6861809.

[54] Hongwen He, Rui Xiong, and Jinxin Fan. "Evaluation of Lithium-Ion Battery Equivalent Circuit Models for State of Charge Estimation by an Experimental Approach". In: *Energies* 4.4 (2011), 582–598. ISSN: 1996-1073. DOI: 10.3390/en4040582. URL: http://dx.doi.org/10.3390/en4040582.

[55] Kandler A. Smith, Christopher D. Rahn, and Chao-Yang Wang. "Control oriented 1D electrochemical model of lithium ion battery". In: *Energy Conversion and Management* 48.9 (2007), pp. 2565 –2578. ISSN: 0196-8904. DOI: https://doi.org/10.1016/j.enconman.2007.03.015. URL: http://www.sciencedirect.com/science/article/pii/S0196890407000908.

[56] Martin S. Alnæs et al. "The FEniCS Project Version 1.5". In: *Archive of Numerical Software* 3.100 (2015). DOI: 10.11588/ans.2015.100.20553.

[57] Conrad Sanderson and Ryan Curtin. "Armadillo: a template-based C++ library for linear algebra". In: *Journal of Open Source Software* 1 (2016). DOI: 10.11588/ans.2015.100.20553.

[58] Jeffrey Belt. “Battery Test Manual For Plug-In Hybrid Electric Vehicles”. In: (Jan. 2010). DOI: 10.2172/1010675.

[59] Xin Lai et al. “A comparative study of global optimization methods for parameter identification of different equivalent circuit models for Li-ion batteries”. In: *Electrochimica Acta* 295 (2019), pp. 1057 –1066. ISSN: 0013-4686. DOI: https://doi.org/10.1016/j.electacta.2018.11.134. URL: http://www.sciencedirect.com/science/article/pii/S0013468618326173.

[60] Ari Hentunen, Teemu Lehmuspelto, and Jussi Suomela. “Time-Domain Parameter Extraction Method for Thévenin-Equivalent Circuit Battery Models”. In: *Energy Conversion, IEEE Transactions on* 29 (Sept. 2014), pp. 558–566. DOI: 10.1109/TEC.2014.2318205.

[61] Seyed Madani, Erik Schaltz, and Søren Knudsen Kær. “An Electrical Equivalent Circuit Model of a Lithium Titanate Oxide Battery”. In: *Batteries* 5.1 (2019), p. 31. ISSN: 2313-0105. DOI: 10.3390/batteries5010031. URL: http://dx.doi.org/10.3390/batteries5010031.

[62] Jonathan Nadeau et al. “Ageing Estimation of Lithium-Ion Batteries Applied to a Three-Wheel PHEV Roadster”. In: Oct. 2013, pp. 1–6. DOI: 10.1109/VPPC.2013.6671663.

[63] ASTM E3057-19. “Standard Test Method for Measuring Heat Flux Using Directional Flame Thermometers with Advanced Data Analysis Techniques”. In: *ASTM International* (2019). DOI: 10.1520/E3057-19.

[64] M. Schimpe et al. “Comprehensive Modeling of Temperature-Dependent Degradation Mechanisms in Lithium Iron Phosphate Batteries”. In: *Journal of The Electrochemical Society* 165.2 (2018), A181–A193. DOI: 10.1149/2.1181714jes. URL: https://doi.org/10.1149%2F2.1181714jes.

[65] Alexander J. Headley et al. “Thermal conductivity measurements and modeling of ceramic fiber insulation materials”. In: *International Journal of Heat and Mass Transfer* 129 (2019), pp. 1287 –1294. ISSN: 0017-9310. DOI: https://doi.org/10.1016/j.ijheatmasstransfer.2018.10.060. URL: http://www.sciencedirect.com/science/article/pii/S001793101833151X.

[66] Xuning Feng et al. “A Coupled Electrochemical-Thermal Failure Model for Predicting the Thermal Runaway Behavior of Lithium-Ion Batteries”. In: *Journal of The Electrochemical Society* 165 (Jan. 2018), A3748–A3765. DOI: 10.1149/2.0311816jes.